THE UNIVERSITY OF CHICAGO

PLANET-PLANET INTERACTIONS IN EXOPLANET SYSTEMS

A DISSERTATION SUBMITTED TO
THE FACULTY OF THE DIVISION OF THE PHYSICAL SCIENCES
IN CANDIDACY FOR THE DEGREE OF
DOCTOR OF PHILOSOPHY

DEPARTMENT OF ASTRONOMY AND ASTROPHYSICS

BY

NORA BAILEY

CHICAGO, ILLINOIS

JUNE 2022

Dedicated to Fíli and Pippin, who were here for it all.

"There is a theory which states that if ever anyone discovers exactly what the Universe is for and why it is here, it will instantly disappear and be replaced by something even more bizarre and inexplicable.

There is another theory which states that this has already happened."

Douglas Adams

TABLE OF CONTENTS

LIST OF FIGURES viii

LIST OF TABLES x

ACKNOWLEDGMENTS xi

ABSTRACT xiii

1 INTRODUCTION 1
1.1 A Brief History of Planetary Dynamics 1
1.1.1 Kepler's Laws 2
1.1.2 Newton's Law of Gravity 3
1.1.3 Einstein's Theory of Gravity 3
1.1.4 Gravity and Multiple Planets 4
1.2 The Rise of Exoplanets 6
1.2.1 The Kepler Survey 7
1.3 Numerical Methods 9
1.3.1 Limitations 10
1.3.2 The `REBOUND` N-body Integrator 11

2 NODAL PRECESSION IN CLOSELY SPACED PLANET PAIRS 13
2.1 Introduction 13
2.2 Numerical Investigation 16
2.2.1 Restricted Simulations 16
2.2.2 Unrestricted Three Body Simulations 19
2.3 Analytical Investigation 23
2.3.1 Analytical Results 25
2.3.2 Time Dependence 28
2.3.3 Effect of General Relativity 29
2.4 Limits of Applicability 30
2.5 Application to Kepler Population 35
2.6 Secular Resonance 37
2.7 Conclusions 39
2.8 Appendix 40
2.8.1 Expressions of $f(\alpha)$ 40
2.8.2 Tabulated Results 43

3 PERIOD RATIO SCULPTING NEAR SECOND-ORDER MEAN-MOTION RESONANCES 46
3.1 Introduction 47
3.2 Methods 49
3.2.1 System Generation 49

3.2.2 Analysis . . . 51
3.2.3 Model . . . 52
3.2.4 Fitting . . . 53
3.2.5 Sampling and Fitting Eccentricity Scales . . . 54
3.3 Results . . . 57
3.4 Analytics . . . 61
3.5 Discussion . . . 70
3.5.1 Comparison with Previous Results . . . 70
3.5.2 Tides . . . 72
3.5.3 Eccentricity at Formation . . . 74
3.5.4 Mass Dependence . . . 74
3.5.5 Resonance Probability . . . 76
3.5.6 Investigating the Case of K02261 (Kepler-1164) via Timing Analysis . 77
3.6 Conclusion . . . 83
3.7 Appendix . . . 84
3.7.1 KOIs . . . 84
3.7.2 Population Comparisons . . . 84

4 RELATIVE HABITABILITY OF EXOPLANET SYSTEMS WITH TWO GIANT PLANETS . . . 92
4.1 Introduction . . . 93
4.2 Methods . . . 94
4.2.1 Architecture Selection . . . 94
4.2.2 Process . . . 97
4.2.3 Stability Outcomes . . . 99
4.2.4 Habitability Model . . . 103
4.2.5 Example Relative Habitability Calculation . . . 107
4.3 One-Dimensional Analysis . . . 109
4.3.1 Giants Exterior to HZ . . . 109
4.3.2 Giants Interior to HZ . . . 113
4.4 Multi-Dimensional Analysis . . . 116
4.4.1 Results . . . 116
4.4.2 Discussion . . . 118
4.4.3 Future Work . . . 129
4.5 Conclusion . . . 130
4.6 Appendix . . . 132
4.6.1 Stability Outcome Results . . . 132

5 IN CLOSING . . . 134

REFERENCES . . . 136

SUPPLEMENTARY FILES AVAILABLE ONLINE

Machine Readable Table, Restricted Simulation Data (Full Version of Table 2.4)

Machine Readable Table, Unrestricted Simulation Data (Full Version of Table 2.5)

LIST OF FIGURES

1.1 Overview of Orbital Elements 4
1.2 Cumulative Total of Known Exoplanets Over Time 7

2.1 Deviation of Precession Period from Linear Theory (Test Particle) 20
2.2 Deviation of Precession Period from Linear Theory (Massive Planets) 22
2.3 Deviation of Precession Period from Linear Theory (Test Particle, Multiple Configurations) 25
2.4 Deviation of Precession Period from Linear Theory (Massive Planets, Multiple Configurations) 26
2.5 Laplace Coefficients versus α 28
2.6 Precession Rate Over Time (Example) 29
2.7 Distribution of Simulations by Accuracy 31
2.8 2D Distribution of Simulations by Accuracy 33
2.9 Distributions of Kepler-Like Planets 35
2.10 Deviation of Actual Precession Period from Linear Theory (CDF) 36
2.11 Secular Resonance Location Kepler-117 37

3.1 Period Ratio Distribution (Simulated Systems) 52
3.2 Eccentricity Distribution (Generated Systems) 55
3.3 Various Eccentricity Distribution PDFs 56
3.4 Period Ratio Distribution (CDF) - Data and Model (Generated Systems) 57
3.5 Period Ratio Distribution (CDF) - Data and Model (Kepler) 59
3.6 Peak Area Distributions (Beta Distribution) 60
3.7 Sub-samples and Model at Varying Eccentricities 62
3.8 Peak Area Comparison (Rayleigh Distribution) 63
3.9 Analytical Period Ratio Distribution 65
3.10 Period Ratio Distribution (CDF) - Fiducial Analytical 66
3.11 Period Ratio Distribution (CDF) - Analytical with Varied Parameters 68
3.12 Tidal Circularization Timescales 73
3.13 Mass and Eccentricity Splitting (Generated Systems, 3:1) 75
3.14 Mass and Eccentricity Splitting (Generated Systems, 5:3) 76
3.15 Resonance Probability for Kepler Planets Near 5:3 77
3.16 K02261 Period Ratio Over Time 79
3.17 Exact versus Estimated Period Ratios from Simulations 81
3.18 K02261 Period Ratio Over Time (Simulated) 82
3.19 Mass Ratio Distributions (Generated Systems) 87
3.20 Inner Period Distributions (Generated Systems) 87
3.21 Period Ratio Distributions (Generated Systems) 88
3.22 Mutual Inclination Distributions (Generated Systems) 89
3.23 Longitude of Pericenter Alignment Distributions (Generated Systems) 90
3.24 Argument of Pericenter Alignment Distributions (Generated Systems) 91

4.1 Spectral Fraction Distributions Earth-Jupiter-Jupiter 103

4.2 Unperturbed Habitability Model 104
4.3 2D (a-e) Habitability Model 106
4.4 Relative Habitability Calculation (Example) 108
4.5 Relative Habitability by Parameter (Outer Fiducial) 110
4.6 Relative Habitability by Parameter (Inner Fiducial) 113
4.7 Relative Habitability by Parameter (Multidimensional) 117
4.8 Mean Relative Habitability Comparison by Inclination 118
4.9 Mean Relative Habitability Comparison by Pericenter Alignment 119
4.10 Maximum Habitable Eccentricity Distribution 119
4.11 Maximum Earth Eccentricity (High a_1 Example) 121
4.12 Maximum Earth Eccentricity (α/a_1 Example) 122
4.13 Maximum Earth Eccentricity and Stability Outcome (High Combined Mass Example) 123
4.14 Relative Habitability Range Distributions by Parameter 124
4.15 Distributions of Parameters for Relative Habitability > 1 125
4.16 Distributions of Parameters for Relative Habitability 0.5 Overlapping the HZ . . 127

LIST OF TABLES

2.1 Initial Conditions - Test Particle 18
2.2 Initial Conditions - Massive Planets 21
2.3 Kepler-117 System Parameters 38
2.4 Restricted Simulations Data 44
2.5 Unrestricted Simulations Data 45

3.1 MCMC Fitted Parameters 58
3.2 Analytical Investigation Variable Parameters 66
3.3 Possibly Resonant 5:3 KOIs 78
3.4 KOIs 85

4.1 Varied Parameter Ranges 95
4.2 Multidimensional Relative Habitability Results 116
4.3 Multidimensional Stability Results 133

ACKNOWLEDGMENTS

While it is my name that appears on the title page, there are many people who made this dissertation and my academic journey to PhD possible.

First and foremost, I must thank my advisor, Dan Fabrycky. For many things, including his patience, his mentorship, and perhaps most importantly his love of celestial mechanics. His in-depth knowledge of seemingly every paper ever published in our field was quite the feat! In addition, I want to thank my thesis committee: Dan, Leslie Rogers, Fred Ciesla, and Mike Gladders. Their feedback was of enormous help in completing this gargantuan task.

I also want to thank the other graduate students in the department, especially the exoplanet group, and the faculty and staff for making an environment of learning, exploration, and achievement. I must thank my undergraduate professors, Elise Albert and Jeff Larsen, for giving me such a love of astrophysics and helping me return to the field rather later than most. Thanks as well to Mr. Hayes, my high school AP Physics teacher, who was so shocked I ended up studying physics—sorry for complaining about it so much!

Thanks to my family for their love and support through this newest phase of my life, like they did for all the ones before. Thanks especially to my dad, who always encouraged a love of learning in me—an occupational hazard of being a philosopher—and now has to deal with not being the coolest Dr. Bailey around.

Thank you to my friends, both new ones met during this process and old ones who have known me since I was the awkward kid who read while walking between classes in middle school. Especially thank you to Christina (excuse me, Dr. Knudson), who helped me understand that getting a PhD wasn't as scary as the internet made it sound. Thanks to the Scotch Hour group, which fell apart thanks to time and covid but was a huge part in making Chicago feel like home.

Lastly and in no way leastly, thanks to Anthony, the unexpected acquaintance of an exoplanet conference who is now my dearest partner. He has supported me through thick

and thin, navigated the byzantine immigration system to be by my side, and always believed in me even during the many, many times I did not believe in myself. And of course he provided the excellent motivation of not letting him be the only doctor in the house!

I am very grateful to everyone who has helped me achieve this dream of mine. Thank you all.

ABSTRACT

The gravitational interactions of planets in multiplanetary systems can have effects ranging from tiny orbital alterations to severe instability and everything in between. In this thesis, I discuss three applications of planet-planet interactions.

First, I demonstrate using N-body simulations that a commonly used analytical approximation can have large inaccuracies for planetary systems like those observed by the Kepler mission when used to calculate the rate at which the longitude of the ascending node changes. The dependency between the eccentricity, inclination, and semi-major axis ratio (α) of a pair of planets requires a higher-order expansion of the disturbing function, particularly in α to recreate the simulated behavior to a specified accuracy. Not accounting for these effects could lead to significant errors when calculating the locations of secular resonances, as I demonstrate with the Kepler-117 system.

Secondly, I use N-body simulations and analytics to illustrate how the slight change in period ratio over time for planet pairs both in and out of mean-motion resonance can lead to observable sculpting of the time-averaged period ratio for a population of planets. The strength of this sculpting depends on the eccentricity of the planets involved, and we can use the observed period ratio distribution from the Kepler mission to infer the distribution of eccentricity for those planets. When modeled as an independent Rayleigh distribution for each planet, I find the Rayleigh scale parameter is $\sigma_e < 0.245$ (near the 3:1 resonance) and $\sigma_e < 0.095$ (5:3) with 95% confidence.

Lastly, I endeavor to quantify how the presence of two giant planets affects the potential habitability of an Earth-like planet. Stability predictions, on both long and short timescales, are combined with the maximum eccentricity for Earth-like planets located near the expected habitable zone and a probabilistic habitability model to assess the relative habitability for each giant planet configuration—that is, the integrated habitability probability compared to a system with only an Earth-like planet. By varying the properties of the two giant

planets (mass, semi-major axis, eccentricity, and inclination), I identify correlations between various parameters, identify particularly habitable and uninhabitable configurations, and demonstrate how the interplay of mean-motion resonance, secular resonances, and other dynamical effects must be taken into account when considering habitability.

CHAPTER 1

INTRODUCTION

The planets of our solar system (save Uranus and Neptune) have been known to humankind for as long as our species has been looking up to the night sky. Thanks to their proximity to Earth, these planets are as bright as any star, but unlike the stars, the locations of the planets are not fixed in the sky. This is the origin of the name "planets," from the Greek "πλανήτης (wanderer)."

Attempting to explain the motion of the planets across the sky is the first step of planetary dynamics.

1.1 A Brief History of Planetary Dynamics

As the night sky extends in every direction when we look up from Earth, early models of the solar system naturally centered on the Earth. This viewpoint was reinforced by religious and cultural sentiments about the importance of the Earth. Ancient Greeks like Eudoxus and Aristotle developed models based on combinations of perfect spheres to explain the observations of planetary motion [Easterling, 1961]. These models gave way to the more detailed geocentric model of Ptolemy, published in his 2nd century treatise *Almagest*. The Ptolemaic model of deferents, epicycles, and equants could predict the motions of the planets to within ten arcminutes ($^1/_6{}^\circ$), roughly the observational accuracy of the time [Babb, 1977]. The Ptolemaic model was the prevailing model for over a millennium, until the sixteenth century and the model published by Copernicus in *De revolutionibus orbium coelestium*. The Copernican model represented a revolutionary shift by placing the Sun, rather than the Earth, at the center of the solar system; however, it still included complicated epicycles and did not improve upon the accuracy of the Ptolemaic model.

As observations increased in accuracy and number, astronomers had more data than ever

about the motion of the planets that needed to be explained. The Danish astronomer Tycho Brahe, in particular, created a comprehensive collection of astronomical observations accurate to roughly one arcminute [Verbunt and van Gent, 2010]. This data enabled his assistant, Johannes Kepler, to notice patterns in the movements of the planets that became known as Kepler's laws of planetary motion. These laws of planetary motion, though approximations, are still recognized and used today.

1.1.1 Kepler's Laws

Kepler's three laws are:

1. All planets move about the Sun in elliptical orbits, having the Sun as one of the foci.
2. A line drawn between a planet and the Sun sweeps out equal areas during equal time intervals.
3. The squares of the planets' orbital periods are directly proportional to the cubes of their mean distances from the Sun.

The first two laws were published in Kepler's 1609 text *Astronomia nova* and the third in his 1619 work *Harmonices Mundi*. The first law was another revolutionary shift—not only to heliocentrism (Kepler was a Copernican), but away from the insistence on perfect circles. A simple ellipse was able to explain the movements of the planets without complicated epicycles or equants.

All of these laws can now be described mathematically, but at the time neither calculus nor the law of gravity existed, making these laws all the more remarkable in the keenness of their insight.

1.1.2 Newton's Law of Gravity

Isaac Newton used inductive reasoning to consider how forces on the surface of the Earth might be extended to much larger distances. He posited that this gravitational attraction could be universal, and he was able to quantify that attraction mathematically, which he published in his 1687 book *Philosophiæ Naturalis Principia Mathematica*. Newton recognized that gravity follows an inverse-square law and depends on the masses of the objects, thus the equation that describes the force of gravity:

$$\vec{F} = G\frac{m_1 m_2}{r^2}\hat{r}. \tag{1.1}$$

The proportionality constant G is one of the physical constants of the universe. This equation applies equally to an apple falling from a tree branch as it does to the Moon orbiting the Earth and the planets orbiting the Sun. All of Kepler's laws can be derived from this equation as well. From the work of Newton and Kepler, the entire field of planetary dynamics was born.

1.1.3 Einstein's Theory of Gravity

Both Kepler's insights about planetary motion and Newton's description of gravity were empirical; they are descriptions of what happens based on observations and identify patterns that can predict future behavior. The scientific theory to explain these laws came about with Einstein's general theory of relativity [Einstein and Lawson, 1921]. Newtonian gravity and Keplerian motion are both consistent with general relativity and are applicable as approximations in many circumstances. While general relativity can become important in the context of planetary dynamics (famously with the orbit of Mercury [Einstein, 1916]), this thesis deals almost exclusively with Newtonian gravity.

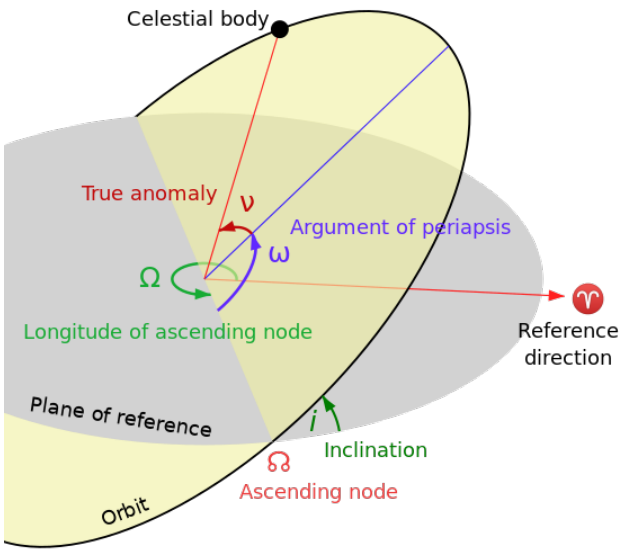

Figure 1.1: Diagram illustrating various terms in relation to orbits of celestial bodies. This illustration was created by the user Lasunncty and is re-used via Wikimedia Commons (CC BY-SA 3.0).

1.1.4 Gravity and Multiple Planets

A single planet orbiting a single star has a well-determined orbit described by six independent parameters. Those parameters can be defined by Keplerian orbital elements; for example, period (P), eccentricity (e), inclination (i), longitude of ascending node (Ω), argument of pericenter (ω), and mean longitude (λ) at epoch, where epoch is the reference time. Alternative orbital elements can be used, such as semi-major axis (a) in place of period, or an entirely different system such as Cartesian position (x, y, z) and velocity (v_x, v_y, v_z), also six independent parameters, at epoch. Figure 1.1 illustrates examples of some of the common orbital elements.

Additional planets in the system, however, cause perturbations of the planetary orbits. The orbital elements are then no longer constant over time. In fact, this type of planet-planet perturbation led directly to the discovery of the planet Neptune, thanks to Neptune's effects on the orbit of Uranus [Le Verrier, 1846, Galle, 1846]. These perturbations can be increased in strength when the planets' orbital periods are integer multiples of one another, a dynamical state called mean-motion resonance.

If the planets are unstable or in mean-motion resonance, their orbital elements might

change quickly over short time periods. But even stable, non-resonant planets give rise to perturbations that cause the planets' orbital elements to change on long, or secular, timescales. This was recognized as far back as Newton himself, who considered that these small changes could build up over time and eventually destabilize the Earth, possibly requiring occasional interventions from a deity over long timescales. Indeed, the effect of other planets on the habitability of the Earth is not negligible, a concept that is explored in Chapter 4.

The question of solving the problem of these planetary perturbations occupied planetary dynamicists for centuries as they sought to create perfect models of the solar system that could predict the motions of the planets over an indefinite period of time. Leonhard Euler, Joseph-Louis Lagrange, and Pierre-Simon Laplace, among others, applied themselves to these questions of celestial mechanics, particularly in regards to the stability of the solar system. In fact, the approximation we now call Laplace-Lagrange theory is still used today to understand multiplanet systems, though this theory does not capture the multi-faceted dependence on eccentricity and inclination, especially for planets close to one another, as will be shown in Chapter 2 for the precession rate of the longitudes of ascending node for a pair of planets.

However, Henri Poincaré eventually proved that, with three or more bodies, a general analytical solution to the problem is no longer possible [Poincare, 1892]. Thus planetary dynamicists developed a plethora of approximate solutions to apply, including the use of a disturbing function that describes the perturbing potential experienced by one planet due to another. The disturbing function can be applied to describe how the orbital elements of a planet change over time, usually in the form of some approximate expansion. See Murray and Dermott [1999] for an excellent reference covering these ideas, including the disturbing function expansion that underlies the work in Chapter 2.

1.2 The Rise of Exoplanets

The study of planetary dynamics concerned itself primarily with the solar system (including planets, moon, asteroids, and even artificial satellites) for good reason—it was the only data point to be had. While planets around other stars, called exoplanets, were considered likely as far back as Giordano Bruno in the 16th century, no signals of these objects had been detected.

That changed in 1992 with the first confirmed exoplanet detection: two planets orbiting the pulsar PSR B1257+12 [Wolszczan and Frail, 1992]. As is often the way with paradigm-shifting discoveries, this was an unusual case, given that the central object in this system was a rapidly rotating neutron star rather than a quiet G-dwarf like our Sun. Exoplanets around Sun-like stars were soon to follow, with the detection of a large planet orbiting the star 51 Pegasi [Mayor and Queloz, 1995]. But this system, too, was an unusual case. The planet is similar in mass to Jupiter, but orbits its star at less than 0.053 AU—more than seven times closer than Mercury does in the solar system.

These unusual and historic discoveries were a prime opportunity for dynamicists. For the first time in history, there were architectures other than the solar system to analyze and explain. For example, hot Jupiters, as those close-in gas giants came to be known, are very unlikely to have formed in their current locations (Lin et al. 1996, though perhaps possible, e.g. Batygin et al. 2016), meaning that some dynamical process is at play. Exoplanets around stellar remnants, like the PSR B1257+12 system, must account for complicated dynamical effects from stellar mass loss and violent stellar winds or from post-main sequence formation or capture (see Veras [2016] for a review).

Unlike the planets of the solar system, which have a maximum eccentricity of 0.206 and inclination of 6.34° (both belonging to the smallest planet, Mercury), exoplanets quickly revealed the potential for very high eccentricities and inclinations. The planet HD 20782 b has an eccentricity of 0.95 ± 0.001 [Jones et al., 2006, Udry et al., 2019], and while inclinations

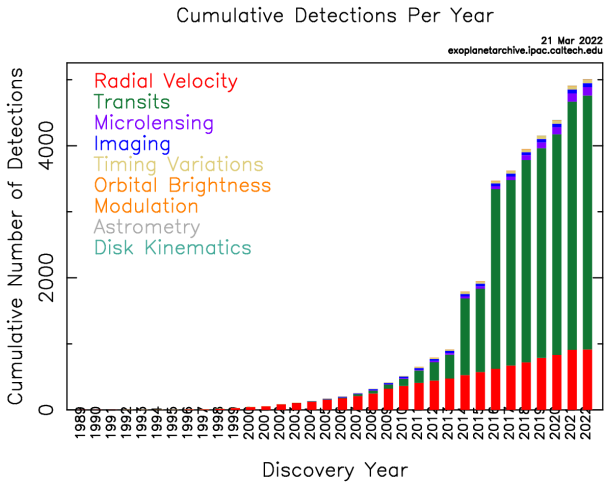

Figure 1.2: The cumulative total of known exoplanets over time, colored by detection method of the discovery. The total surpassed 5,000 exoplanets on March 21, 2022. This figure was created by the NASA Exoplanet Archive.

are harder to measure, π Mensae b and c have a mutual inclination of at least 34.5° [De Rosa et al., 2020].

Not only are these types of orbits indicative of a history of significant dynamical interactions, but they represent a challenge for many of the analytical approximations developed by planetary dynamicists, which often apply only in the regime of low eccentricities and inclinations.

1.2.1 The Kepler Survey

The earliest exoplanet discoveries were primarily accomplished by the radial velocity method (see Wright and Gaudi [2013] for an overview of detection methods). While the radial velocity method continues to be used to discover new planets, the new primary method of detection is the transit method, as illustrated in Figure 1.2. This shift was largely due to NASA's Kepler mission, which launched in 2009 [Borucki et al., 2010].

The Kepler space telescope operated for almost ten years and completed two different missions. The primary mission, from 2009 to 2013, is the "Kepler" mission and the second mission, after reaction wheel failure, is called "K2." In this thesis, reference to "Kepler" is to the mission and not to the telescope.

During the mission, the telescope had a fixed field of view and pointing; that is, it

was constantly observing the same patch of sky (115 square degrees in the constellations Cygnus, Lyra, and Draco). Within this area, there were approximately 180,000 target stars, including over 90,000 G-type stars like the Sun. By looking at the same set of stars for a long period of time, and by being a space telescope free of atmospheric absorption and interference, Kepler was sensitive to smaller planets on wider orbits than previous exoplanet hunts. And the results from the mission did not disappoint, as Kepler began discovering exoplanet candidates almost immediately.

The potential planets found by Kepler are considered only candidates until they can be confirmed by follow-up observations or statistically validated. But it is expected that the vast majority of Kepler candidates are, in fact, real exoplanets [Morton and Johnson, 2011]. The Kepler data is publicly available and still being studied by astrophysicists all over the world to tease as much information and as many detections as possible from the data. As of February 2022, there were 4766 planet candidates and 2709 confirmed planets detected by Kepler.

The Kepler results enabled the field of exoplanets to step from studying individual systems to considering the population of planets in the galaxy. Kepler's detections also included a large number of multiplanetary systems, again allowing planetary dynamicists access to a whole population of planetary systems besides our own solar system.

Fabrycky et al. [2014] covers many of the early insights into multiplanetary systems discovered by Kepler. Analysis of a subset of Kepler targets with better-characterized stellar properties (the California Kepler Survey) also revealed insights such as the "peas in a pod" idea that planets within a system tend to have similar properties [Weiss et al., 2018] and the apparent dearth of close-in planets with middling radii [Fulton et al., 2017]. Study of the architectures of Kepler systems continues, such as the system-level framework of Gilbert and Fabrycky [2020], extensive forward modeling efforts like He et al. [2020], and much more.

One challenge for dynamicists hoping to delve the depths of the Kepler data is that the

transit method measures only the radius of a planet, not its mass, while mass is the more important characteristic for dynamical interactions. One can use a mass-radius relation, such as Chen and Kipping [2017], to associate a predicted mass with a measured radius, but this is not a fully reliable method due to the intrinsic scatter in this relationship and dependence on other parameters, like the period [Neil and Rogers, 2020].

Ideally, actual mass measurements would be obtained from follow-up observations, but many of Kepler's targets are too faint for reliable radial velocity follow-up. Interactions between planets in multiplanet systems, even unseen planets, can have detectable effects that depend on mass, like transit timing variations (TTVs) [Holczer et al., 2016], when the time between transits changes from an exactly periodic timing. However, identifying a solution to observed TTVs requires fitting many parameters with degeneracies (e.g. between mass and eccentricity [Lithwick et al., 2012]) and is very computationally intensive. When the perturbing planet is unseen, the parameter space can be almost unbounded. Though some techniques can be applied to alleviate some of these issues (e.g. Deck and Agol [2015], Hadden and Lithwick [2017]), it remains a challenge.

Thus an indirect route to investigate the dynamics of the Kepler population is often required. The period ratio distribution offers insights into the frequency of mean-motion resonance, either directly from the observed distribution as in Steffen and Hwang [2015] or more indirect approaches such as Petrovich et al. [2013] or the one included in this thesis (Chapter 3). The various analyses of the Kepler population are too vast to list here, but these results have been an enormous opportunity to increase our understanding of planetary systems and their interactions.

1.3 Numerical Methods

As has been noted, the N-body problem is not one with a general solution for $N > 2$. Early approximations were truncated by necessity, as computation was limited to pen-and-paper

calculations.

Computers, however, offer a new level of computational ability to numerically solve the equations of motion for particles in a system. As computing power has become ever more abundant and ever cheaper over the past few decades, direct N-body integration has become more useful than ever.

The idea behind an N-body integrator is straightforward. At a single point in time, particles exist at a given location with given velocities, and the force of gravity is acting between every pair of particles. There is an acceleration associated with this gravitational force, which will change the velocity of the particles. The integrator will calculate that change in velocity over some timestep, update the particles' velocities accordingly, and update the particles' positions according to their velocities. This is now a new instant in time, and the gravitational force is recalculated and the process repeated.

In practice, of course, things get much more complicated. The timestep can be broken down in further steps, and the velocity change ("kick") and position change ("drift") might be applied in different orders and fractions of a timestep. Broadly speaking, the number of steps within a timestep is considered the order of the approximation.

1.3.1 Limitations

Integrators may be designed to be symplectic, where there is a conserved Hamiltonian for the system, such as the Wisdom-Holman integrators [Wisdom and Holman, 1991]. Symplectic integrators exploit the physical nature of the gravitational system and can be much faster and have lower total energy errors than other integrators; however, pure symplectic integration gives rise to spurious frequency signals and so symplectic correctors are often used to increase the accuracy [Wisdom et al., 1996]. Even with the use of correctors, these integrators can create inaccuracies in the long time-scale frequencies of a system [Rein et al., 2019], and it is difficult to add in features like additional non-gravitational forces, adaptive timesteps, or

non-hierarchical systems using symplectic integrators.

Higher order integrators provide greater accuracy, but the increased number of calculations slows down the integration. Likewise, reducing the size of a timestep increases the accuracy but also the required time for the integration to complete. Understanding the trade-offs between accuracy and efficiency, and what is needed in a given situation, is an important part of utilizing N-body simulations for scientific research. For example, Wisdom [2015] estimates the required timestep to resolve pericenter passage for an eccentric planet, which might range from 16 steps per orbit for a circular planet on an Earth-like orbit to 700 steps per orbit at $e = 0.9$!

Furthermore, it is important to understand that even the most precise numerical methods are subject to errors. One strong limitation is the floating-point accuracy of a computer, because any number stored is subject to a finite length (typically 64 bits on a modern computer, or about 16 decimal digits). Because of this, the minimum error will grow as a random walk as the number of steps (N) increases, proportional to $\sqrt{N}$, or proportional to $\sqrt{N}^3$ for angle-like quantities, a limitation known as Brouwer's law [Brouwer, 1937].

Errors arising from the numerical approximations can lead to numerical chaos, and the physical systems represented by an N-body integration can be chaotic themselves (e.g. our own solar system [Sussman and Wisdom, 1992]). Presence of chaos—that is, widely diverging outcomes due to small differences in initial conditions—means that any single N-body integration is only one iteration of what is more likely a distribution of possible outcomes for a system [Hernandez et al., 2020, Hussain and Tamayo, 2020].

Even so, N-body integrators are formidable tools in the belt of any celestial mechanic.

1.3.2 The `REBOUND` N-body Integrator

There are many software packages in many programming languages that have implemented various N-body integration schemes. In this thesis, I make use of the `REBOUND` package [Rein

and Liu, 2012], which can be downloaded freely at http://github.com/hannorein/rebound. `REBOUND` has both a C version and a Python version (which is a wrapper for the C package), the latter being the one used here.

`REBOUND` has many different integrators built into its functionality, and the user is able to choose among them. The default integrator is IAS15 [Rein and Spiegel, 2015], an adaptive-timestep, 15th-order integrator. Adaptive timestepping means that the integrator uses a predictor-corrector routine and a trial timestep to ensure that each timestep is accurate to machine precision. This allows for larger timesteps to speed up the integration and smaller timesteps to ensure accuracy (for example, by resolving pericenter passage of an eccentric planet), all without explicit instruction from the user. The energy error of IAS15 follows Brouwer's law, indicating that it is optimal.

IAS15 is one of the most accurate N-body integrators available, and is used heavily in this thesis. However, even with adaptive timestepping, IAS15 can be slower than other integrators. When the highest levels of accuracy are not needed, other faster integrators can be used instead. In this thesis, I also make use of the WHFast integrator [Rein and Tamayo, 2015]. WHFast is an improved version of a Wisdom-Holman symplectic integrator, achieving better speeds and increased accuracy, even approaching Brouwer's law for sufficiently small timesteps. WHFast is not adaptive, so the timestep must be explicitly set by the user and is constant for the entire integration. Smaller timesteps are slower but more accurate and vice versa.

Armed with `REBOUND` and various analytical approximations, I set out in this thesis to study various effects that planets have on one another in exoplanet systems. What starts with one small law of gravity turns out to have innumerable implications...let us investigate!

CHAPTER 2

NODAL PRECESSION IN CLOSELY SPACED PLANET PAIRS

In this chapter, we turn to the disturbing function to consider the secular change of the orbital element Ω, also known as the nodal precession.

Previous work has evaluated the nodal precession rate for planets in the limit of low α (semi-major axis ratio, $0<\alpha\leq1$). While conducting simulations using computers to numerically solve the equations of motion from Newtonian gravity (from Equation 1.1), however, I showed that 2-planet systems at high α (or low period ratio), similar to multiplanet systems found in the Kepler survey, have a nodal precession rate that is more strongly dependent on eccentricity and inclination.

I used the disturbing function from Murray and Dermott [1999] to present a complete expansion of the nodal precession rate to fourth order in the disturbing function and showed that this analytical solution much better describes the simulated N-body behavior of high-α planet pairs; at $\alpha \approx 0.5$, the fourth-order solution on average reduces the median analytical error by a factor of 7.5 from linear theory and 6.2 from a second-order expansion. I also set limits on eccentricity and inclination where the theory is precisely validated by N-body integrations, which can be useful in future secular treatments of planetary systems.

This chapter first appeared in *The Astronomical Journal* as Bailey and Fabrycky [2020]. The work described in this paper was performed by me under the guidance and supervision of my advisor (last author).

2.1 Introduction

When multiple planets orbit a star, the planets interact with one another and thus their orbits change over time. Systems with multiple planets are very common–aside from our own solar system with its 8 planets, 1735 of the confirmed 4084 exoplanets reside in multiplanet systems

(NASA Exoplanet Archive[1]), and it's likely that most of the single-planet systems have undetected companions. Understanding how planets interact is necessary to understanding the architectures, stability, and long-term behavior of exoplanet systems.

Laplace-Lagrange theory tells us how orbital parameters change over time for planets using linear secular theory. A pair of planets has one nonzero inclination-node eigenfrequency, given by solving the characteristic equation for the Laplace-Lagrange secular solution as shown in Murray and Dermott [1999, Equation 7.31]. This frequency is equivalent to the planet's change in ascending node per time ($\dot{\Omega}$). An expression for $\dot{\Omega}$ following this derivation is

$$\dot{\Omega}_{\rm LL} = -\frac{1}{4} b^{(1)}_{3/2}(\alpha)\alpha \left(n_1 \frac{m_2}{M_\star + m_1}\alpha + n_2 \frac{m_1}{M_\star + m_2} \right). \tag{2.1}$$

In this equation, for planets 1 and 2, α is the ratio of semi-major axes (a_1/a_2, $a_1 < a_2$), $n_{1,2}$ are the mean motions, and $b^{(1)}_{3/2}(\alpha)$ is the Laplace coefficient (see Equation 2.9 for the general definition). $\dot{\Omega}$ has the same units as the mean motions and is equal for both planets. All orbital elements are given relative to the invariable plane and the central star.

Lithwick and Wu [2011] examine the eccentricity and inclination dependence of the nodal precession. They find an expression for $\dot{\Omega}$ for a test particle interior to a circular massive planet, neglecting terms in $e^2 i^2$, e^4, i^4 and higher, in their Equation 33, reproduced here:

$$\dot{\Omega} = -\gamma(1 - \frac{1}{2}i^2 + 2e^2) \tag{2.2}$$

Their γ is equivalent to $\dot{\Omega}_{\rm LL}$ from Equation 2.1 (assuming m_1=0) except that Lithwick and Wu [2011] use the approximation that $b^{(1)}_{3/2}(\alpha) = 3\alpha$ for $\alpha \ll 1$ [Heyl and Gladman, 2007]. Additionally, for the case where the test particle is *exterior* to a massive planet (m_2=0), the γ expression would need to be modified with a factor of $1/\alpha$ (this difference between the

1. https://exoplanetarchive.ipac.caltech.edu, as of 28 October 2019

inner and outer particles can be seen in the two terms of Equation 2.1).

The focus of Lithwick and Wu [2011] is on the solar system, where the α values are low (particularly between terrestrial planets and Jupiter), and their analysis only includes the first order of α in the Hamiltonian. In exoplanet systems, however, α is frequently larger, and the effect of α on the nodal precession rate may be non-negligible. The goal of this work is to find how the nodal precession rate varies with inclination, eccentricity, and semi-major axis ratio, particularly for the values relevant for packed (though non-resonant) multiplanetary systems like those found by Kepler.

Previous work has largely focused on coplanar systems, both to simplify the problem and as a reasonable approximation given that the mutual inclination of exoplanet systems is generally either small [Fabrycky et al., 2014] or unknown. Coplanar studies have attempted to describe the secular eccentricity evolution of exoplanets systems, finding that fourth-order expansions are not sufficient [Veras and Armitage, 2007] but twelfth-order expansions can succeed [Libert and Henrard, 2006]. Similarly, it is to be expected that higher order terms will be needed to describe non-coplanar secular dynamics, as has been demonstrated in Libert and Henrard [2008] for 3-D secular frequencies modeling the υ Andromedae planetary system with a mutual inclination $\sim 20^\circ$. Additionally, studies that have included inclination effects (e.g. Volpi et al. 2019) tend to be focused on the stability and dynamical effects and not on nodal precession itself.

Secular nodal precession occurs on timescales unlikely to affect observable orbits, but the secular nodal precession frequency can have dynamical implications, particularly via secular resonances. A secular resonance occurs when a linear combination of the apsidal and/or nodal precession frequencies are integer multiples of one another. Because the location of the inclination-node secular resonance depends on the nodal precession frequency, it is potentially sensitive to higher-order effects.

Further, the overlap of these secular resonances can lead to chaos and instabilities in a

planetary system. Both Lithwick and Wu [2011] and Boué et al. [2012] have shown that, in the case of Mercury's excitation, the solar system's few-degree mutual inclinations play an important role in the system's transition to chaos. The location and width of the secular resonances depends on the nonlinear deviations from Laplace-Lagrange theory, and high-α effects could have implications for the onset of chaos in exoplanet systems even at mild inclinations and eccentricities.

In this work, we use both numerical and analytical methods to examine how the nodal precession rate varies with e, i, and α. Our analytical approach here is to expand the disturbing function to fourth order in e and i, keeping all associated higher orders of α. This approach contrasts with other approaches in the literature, such as Laskar and Boué [2010] in which e and i are arbitrary and the expansion of the disturbing function is in α as a small parameter.

In Section 2.2, we describe simulations of restricted and unrestricted 2-planet systems and their nodal precession compared with linear theory. In Section 2.3, we expand the nodal precession rate from Murray and Dermott [1999] to fourth order in e and i, keeping all orders of α, and compare this to our numerical results. In Section 2.4, we investigate the range of parameter space where our analytical solution is accurate. In Section 2.5, we discuss the implications for multiplanet systems similar to those discovered by Kepler. In Section 2.6, we show how an example of how the location of the secular resonance could be affected using the system Kepler-117. Finally, we discuss our conclusions in Section 2.7.

2.2 Numerical Investigation

2.2.1 Restricted Simulations

To examine the effect of α on nodal precession, we ran a suite of restricted three-body simulations with a massive circular planet and a test particle. There were two complete sets

of simulations, one with the test particle as the interior body and one with the test particle as the outer body. The outcomes of both were similar, so here we will present only the case of the massive planet interior to an outer test particle.

Initial Conditions and Integration

Period ratio and α describe the same property of the planet pair–their relative spacing–and are related via Kepler's Third Law:

$$\alpha^3 = \frac{m_1 + M_\star}{(m_2 + M_\star)(P_2/P_1)^2} \tag{2.3}$$

We choose to use period ratio as our parameter space here as it is the directly measurable quantity and for the ease in avoiding mean motion resonances (MMRs), where the planets' periods are integer multiples of one another.

The initial values for the system were randomly generated and then used consistently for each simulation. The inner planet's mass was chosen uniformly between 2 and 10 $M_\oplus$. The inner planet's period was chosen uniformly between 3 and 6 days. The outer planet's longitude of ascending node (Ω) and argument of pericenter (ω) were chosen uniformly between -π and π.

The period, eccentricity, and inclination of the outer test particle were varied across all 3 parameters to cover a region up to 50 in period ratio (avoiding first- and second-order MMRs by ± 0.1 such that $|P_2/P_1 - M/N| \geq 0.1$ for $M = N + 1$ and $M = N + 2$, which results in a lower bound of 1.77 in period ratio), from 0 to 0.1 in eccentricity, and from 0.5 to 6 degrees in inclination. The corresponding range of α is 0.0737 to 0.6834.

The values of Ω were saved every $0.4P_1$, and each system was integrated for $10^5 P_2$, allowing to observe the majority of a nodal precession cycle for even the highest period ratio. Initial system parameters are shown in Table 2.1. The integrations were computed using the `REBOUND` package with the IAS15 integrator [Rein and Liu, 2012, Rein and Spiegel,

2015].

Table 2.1: Initial conditions for the restricted simulations with outer test particle.

Stellar Mass	0.5 $M_\odot$	
Planet:	**b**	**c**
Period (days)	3.4834	$(P_2/P_1)\times 3.4834$
Mass	7.3336 $M_\oplus$	0
Eccentricity	0	e
Inclination	0	i
Ω	N/A	1.0519 rad
ω	N/A	1.0944 rad
Variable Parameters	**Min**	**Max**
P_2/P_1	1.77	50
e	0	0.1
i (deg)	0.5	6

Simulation Analysis

To analyze the output from the simulations, we first checked if the system was stable in period ratio and did not vary more than 0.03 from the starting period ratio. If such a departure occurred, only data from the initial time period before the departure was used for the analysis. Applying this check allowed the initial period ratio to be considered characteristic for the system as well as ensuring the secular approximation that semi-major axis and thus α are constant over time is valid.

Then from the values of Ω over time for each simulation, we fit a sinusoid to $\cos\Omega$ to determine the average period of nodal precession. Typical error bars associated with the period are smaller than the plotted points, although there is some time variation in the nodal precession (see Section 2.3.2). This method takes advantage of the fact that there is a single expected frequency for the pair and is faster and more accurate than more complicated methods, such as Fourier analysis.

We also calculated a predicted period from Laplace-Lagrange theory for each simulation as $P_{\rm LL} = {}^{2\pi}/_{|\dot{\Omega}_{\rm LL}|}$ to be used to scale the periods for uniform comparison.

Results

When the observed simulated nodal precession periods were compared to linear theory, the results were stark. Deviations were seen as high as 12% for relatively low values of inclination and eccentricity, with a very sensitive dependence on α. The changes were much greater than that predicted by Equation 2.2.

These results are shown in the two limiting cases (circular and the lowest inclination of 0.5°) in Figure 2.1. Note the color bar has a break in scale at $P_2/P_1 = 4$ to better show the range of period ratios, which was more densely sampled for $P_2/P_1 < 4$. Zero on the vertical axis corresponds to the predicted value according to Laplace-Lagrange theory. The full set of results can be found in Table 2.4.

The parameter space in period ratio was chosen to avoid first- and second-order mean motion resonances, where the secular interactions can no longer be considered as averaged over the orbits without considering their phase correlation. There was one third-order mean motion resonance in the period ratio grid at $P_2/P_1 = 4$. These simulations exhibited similar qualitative behavior but with a weaker α dependence than the other period ratio simulations, indicating that even third-order mean motion resonances can dominate over secular effects. The $P_2/P_1 = 4$ simulations were excluded from all future analyses and are not plotted in any figures.

2.2.2 Unrestricted Three Body Simulations

Given the marked deviations seen in the restricted simulations, we expanded our numerical approach to full three body simulations with two massive planets.

Initial Conditions, Integration, and Analysis

As before, initial system properties were randomly generated and then used for all simulations. The stellar mass was chosen uniformly between 0.3 and 1 $M_\odot$. The planets' masses

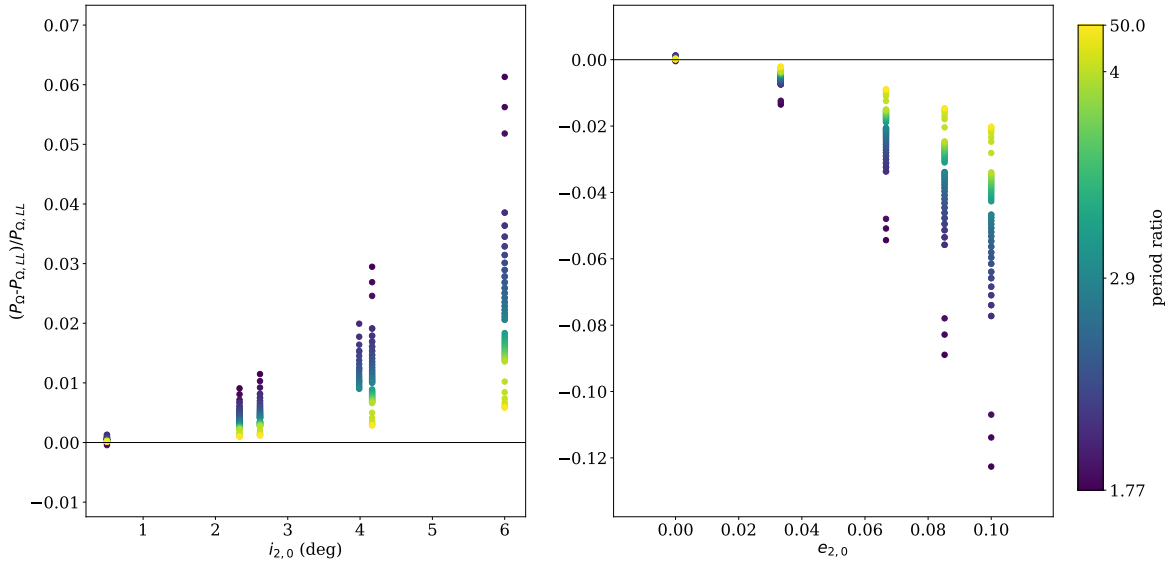

Figure 2.1: Fractional difference of simulated nodal precession period from linear theory ($P_{\rm LL} = {}^{2\pi}/_{|\dot{\Omega}_{\rm LL}|}$) of a test particle external to a massive planet as a function of (left panel:) inclination at zero eccentricity, and (right panel:) eccentricity at low inclination (0.5°). Period ratios are denoted with colors with a break in scale at $P_2/P_1 = 4$.

were chosen uniformly between 2 and 10 $M_\oplus$. The inner planet's period was chosen uniformly between 4 and 8 days. The arguments of pericenter were chosen uniformly between -π and π.

The same values of period ratio, eccentricity, and inclination were used as described in Section 2.2.1, where here both planets are given the same eccentricity e and i is the mutual inclination. Before simulating, the system was rotated into the invariable plane such that the total angular momentum vector is in the z direction (neglecting spin angular momentum, as each body is modeled as a point mass).

Table 2.2: Initial conditions for the three body simulations with two massive planets.

Stellar Mass	0.788 $M_\odot$	
Planet:	**b**	**c**
Period (days)	6.2448	$(P_2/P_1)\times 6.2448$
Mass ($M_\oplus$)	7.6086	8.3235
Eccentricity	e	e
ω (rad)	2.5540	2.1423
Ω (rad)	π	0
Mutual Inclination	i	
Variable Parameters	**Min**	**Max**
P_2/P_1	1.77	50
e	0	0.1
i (deg)	0.5	6

The initial conditions are shown in Table 2.2. As with the restricted simulations, the values of $\Omega_{1,2}$ were saved every $0.4P_1$, and each system was integrated for $10^5 P_2$ using `REBOUND` with IAS15 integrator.

The nodal precession period was analyzed as described in Section 2.2.1 for both the inner planet and the outer planet.

Due to some time-dependent effects (see Section 2.3.2), inaccuracies arose in the higher period ratio systems because only a partial period of nodal precession was simulated in the $10^5 P_2$ time. In order to simulate a long enough time period to observe multiple cycles of nodal precession, the simulations with P_2/P_1 >5 were extended to five times the initially-fit nodal

period. To reduce computational time and memory, these longer simulations were done using the WHFast integrator [Rein and Tamayo, 2015] with timestep $= 0.02 P_1$ and saving outputs approximately every 16000 steps. Because this integrator can introduce additional error in secular frequencies [Rein et al., 2019], we ran a comparison with the previous IAS15 results. This comparison showed that the use of WHFast and decreased sampling had negligible effect on the accuracy of the nodal precession period, agreeing within 10^{-5}.

Results

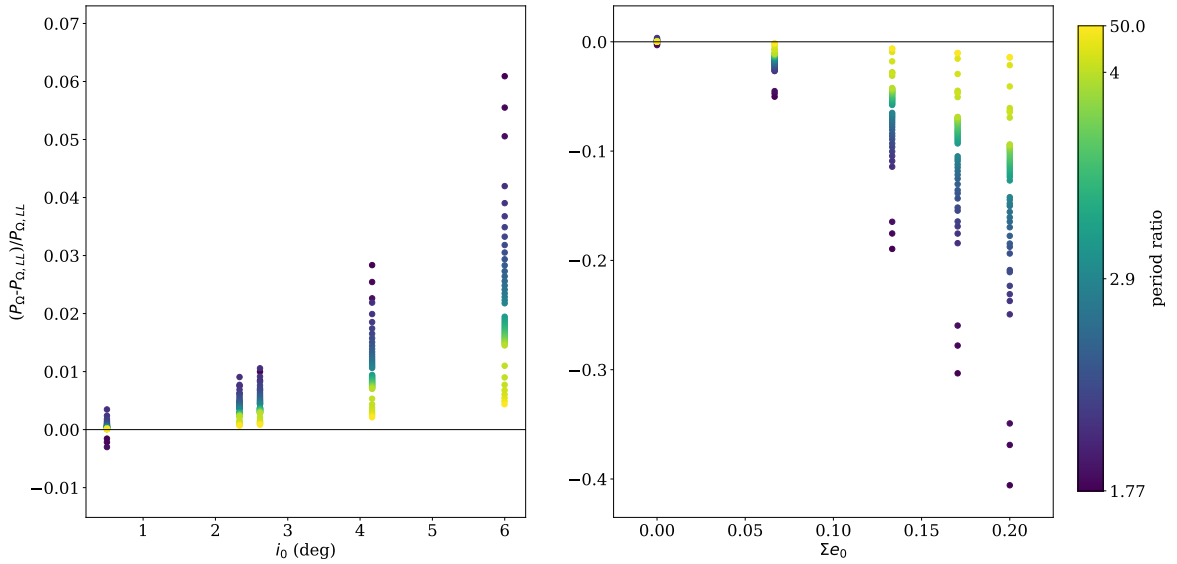

Figure 2.2: Fractional difference of simulated nodal precession period from linear theory in a system with two massive planets as a function of (left panel:) mutual inclination at zero eccentricity, and (right panel:) combined eccentricity ($\Sigma e_0 = e_{1,0} + e_{2,0} = 2e$; see Table 2.2) at low mutual inclination (0.5°). Period ratios are denoted with colors with a break in scale at $P_2/P_1 = 4$. Plotted are the results for the outer planet; the inner planet data is similar.

The fractional deviation from the linear theory period is plotted in Figure 2.2. Only the outer planet is plotted in each panel, but the inner planet data is similar, as expected. The full set of results can be found in Table 2.5.

The nodal precession periods of the unrestricted three body simulations are similar to the restricted simulations in Section 2.2.1. As α increases (period ratio decreases), the eccentricity and inclination dependence also increases.

There is a greater range in the effect of eccentricity here than compared to the test particle case. This is expected because here both the inner and outer planet have eccentricity, whereas in the restricted case only the test particle was given eccentricity. To better illustrate this difference and for comparison with the restricted case, we have used combined eccentricity, $\Sigma e_0 = e_{1,0} + e_{2,0}$, to plot results for the unrestricted systems. Our simulations use equal eccentricities for the unrestricted planets, and therefore do not examine the effect of the partitioning of the total eccentricity between both planets. The scale of the effect is similar when considering only combined eccentricity in the same range as the test particle's eccentricity ($<$0.10).

2.3 Analytical Investigation

As is clearly seen in the results of our numerical simulations (Sections 2.2.1, 2.2.2), including only low order terms of e, i, and α is not adequate to describe the nodal precession period of our simulated systems. Using Murray and Dermott [1999], we developed a higher order expression for $\dot{\Omega}$.

Murray and Dermott [1999] Equation 6.148 shows the change in the ascending node over time. This equation can be combined with the disturbing function in their Equation 6.44/6.45 and the fourth-order expansion in e and i of the disturbing function parts in their Appendix B, solved for secular case of $j = 0$ and averaged over the orbits (i.e., neglecting terms containing mean longitudes in the cosine arguments). The resulting $\dot{\Omega}$ expressions are shown in Equations 2.4 and 2.5 with the disturbing function derivatives shown in Equations 2.6 and 2.7.

$$\dot{\Omega}_1 = \frac{m_2 n_1 \alpha}{4(m_1 + M_\star) s_1 \sqrt{1 - e_1^2}} \frac{\partial R_D}{\partial s_1} \tag{2.4}$$

$$\dot{\Omega}_2 = \frac{m_1 n_2}{4(m_2 + M_\star) s_2 \sqrt{1 - e_2^2}} \frac{\partial R_D}{\partial s_2} \tag{2.5}$$

$$\begin{aligned}\frac{\partial R_D}{\partial s_1} = {} & 2s_1 f_3 + 2s_1(e_1^2 + e_2^2) f_7 + 4s_1^3 f_8 + 2s_1 s_2^2 f_9 - (2s_1 f_{13} - s_2 f_{22} - s_2 f_{23}) e_1 e_2 cos(\omega_2 - \omega_1) \\ & - s_2 f_{14} - (e_1^2 + e_2^2) s_2 f_{15} - (3s_1^2 s_2 + s_2^3) f_{16} + (2s_1 f_{18} - s_2 f_{21}) e_1^2 cos(2\omega_1) \\ & - (2s_1 f_{19} - s_2 f_{24}) e_1 e_2 cos(\omega_2 + \omega_1) + (2s_1 f_{20} - s_2 f_{25}) e_2^2 cos(2\omega_2) + 2s_1 s_2^2 f_{26}\end{aligned} \tag{2.6}$$

$$\begin{aligned}\frac{\partial R_D}{\partial s_2} = {} & 2s_2 f_3 + 2s_2(e_1^2 + e_2^2) f_7 + 4s_2^3 f_8 + 2s_2 s_1^2 f_9 - (2s_2 f_{13} - s_1 f_{22} - s_1 f_{23}) e_1 e_2 cos(\omega_2 - \omega_1) \\ & - s_1 f_{14} - (e_1^2 + e_2^2) s_1 f_{15} - (3s_2^2 s_1 + s_1^3) f_{16} + (2s_2 f_{18} - s_1 f_{21}) e_1^2 cos(2\omega_1) \\ & - (2s_2 f_{19} - s_1 f_{24}) e_1 e_2 cos(\omega_2 + \omega_1) + (2s_2 f_{20} - s_1 f_{25}) e_2^2 cos(2\omega_2) + 2s_2 s_1^2 f_{26}\end{aligned} \tag{2.7}$$

Here, $s_{1,2}$ =sin($i_{1,2}/2$). The f equations are functions of α only and are given in Appendix 2.8.1.

Because of the $s_{1,2}$ derivative and denominator term in Equations 2.4 and 2.5, the highest order of $s_{1,2}$ is 2 in the expression for $\dot{\Omega}_{1,2}$. Similarly, the highest order of $e_{1,2}$ is 2. The highest explicit order of α is 5, with additional α dependence arising from the Laplace coefficients (see Appendix 2.8.1).

For a 2-planet system, $\dot{\Omega}_1$ and $\dot{\Omega}_2$ are expected to be equal. Using this analytical solution, $\dot{\Omega}_1 \simeq \dot{\Omega}_2$ within about 0.1% for our simulations, a good check on the derivation. Additionally, this means the use of restricted test particle simulations, where only $\dot{\Omega}_2$ is calculated, provides

reasonably generalizable results.

2.3.1 Analytical Results

Calculating the expected nodal precession period with the fourth-order derivation and comparing it to our restricted test particle simulations from Section 2.2.1, we find that this approximation is much improved from Equation 2.2. Figure 2.3 shows a sampling of calculated P_Ω for various values of α along with the data from the restricted simulations. This figure is similar to Figure 2.1, but showing a wider range of combinations of inclination and eccentricity as well as the calculated fourth-order model and the second-order prediction from Equation 2.2.

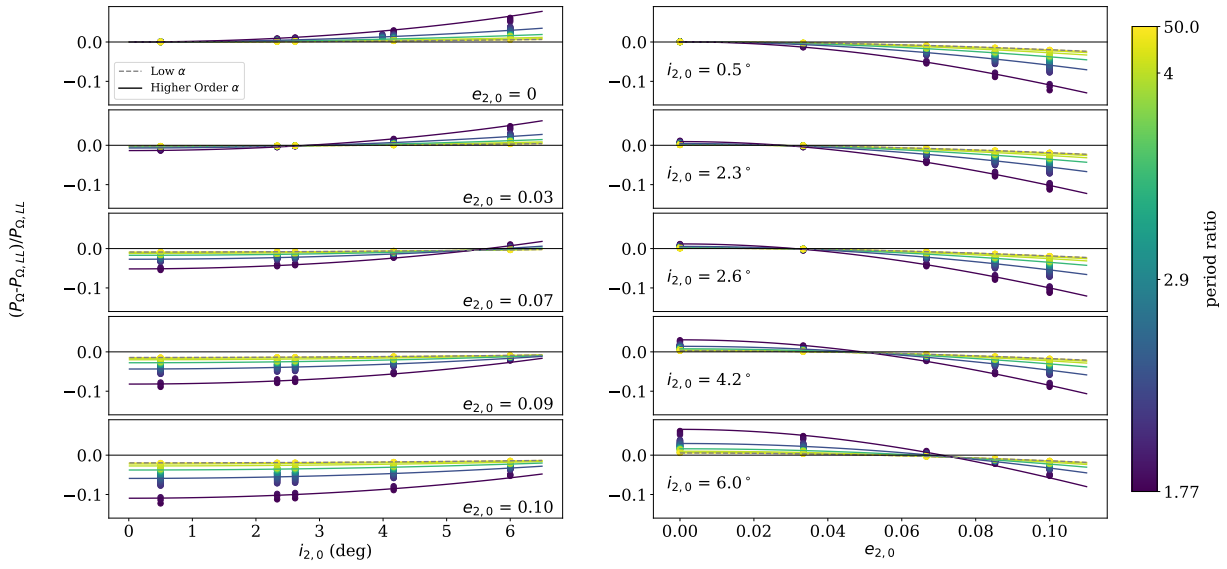

Figure 2.3: Fractional difference of simulated nodal precession period from linear theory of a test particle external to a massive planet as a function of (left panel:) inclination at various eccentricities, and (right panel:) eccentricity at various inclinations. Period ratios are denoted with colors with a break in scale at $P_2/P_1 = 4$. Points show the data from simulations while the solid lines show the results from the analytical solution from Equation 2.5 ($P_\Omega = {}^{2\pi}/_{|\dot{\Omega}|}$) at a sampling of different period ratios. The dashed gray line shows the analytical solution from Equation 2.2.

The analytical solution approaches that of Lithwick and Wu [2011] for low α and matches the stronger inclination and eccentricity dependence that we see for high α. However, because this is a restricted test particle case, the calculation is greatly simplified by the fact that $m_2 = e_1 = s_1 = 0$ and only $\dot{\Omega}_2$ is calculated. To better evaluate the accuracy of the full analytical solution, we evaluate the comparison with the full unrestricted three body simulations. The results are shown in Figure 2.4.

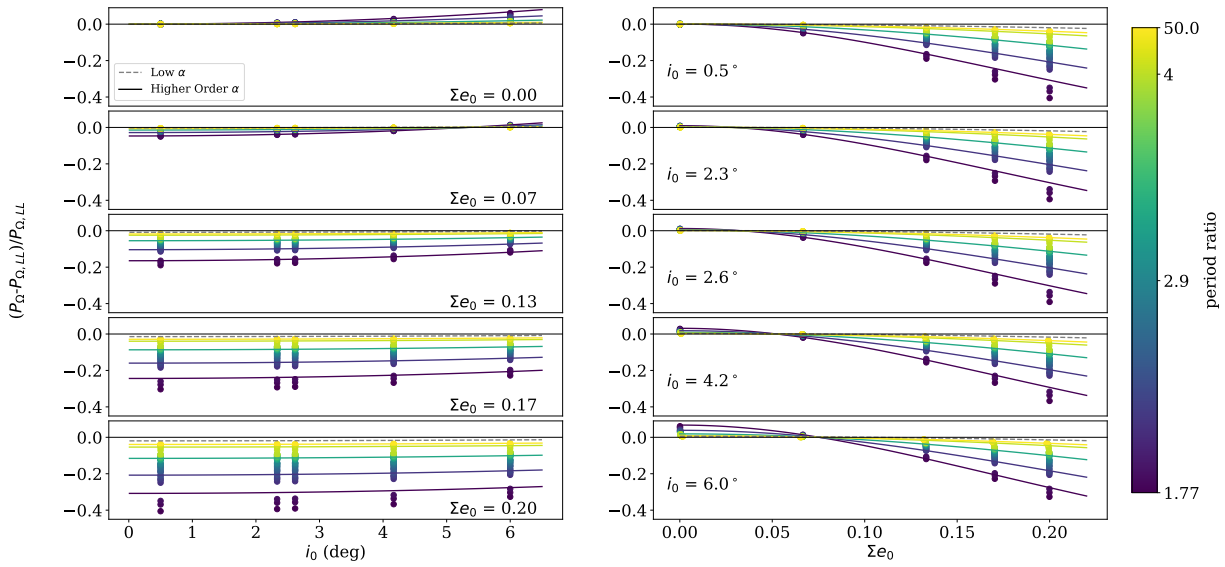

Figure 2.4: Nodal precession rate variation in a system with two massive planets as a function of (left panel:) mutual inclination at various combined eccentricities, and (right panel:) combined eccentricity at various mutual inclinations. Period ratios are denoted with colors with a break in scale at $P_2/P_1 = 4$. Plotted are the results for the outer planet, the inner planet data is similar. Points show the data from simulations while the solid lines show the results from the analytical solution from Equation 2.5 at a sampling of different period ratios. The dashed gray line shows the analytical solution from Equation 2.2.

Here we see that the analytical solution is again a reasonable descriptor of the simulation behavior (with a median accuracy of 0.11%), although the highest-α systems deviate more strongly than predicted, presumably due to higher-order effects. The low-α solution still approximates Equation 2.2, although not as exactly as in the test particle case. This difference

is not unexpected as Lithwick and Wu [2011] consider a test particle and a circular massive perturber, whereas in this case both planets have mass and eccentricity; we use mutual inclination and average eccentricity in calculating Equation 2.2 to account for this change. The results for the inner and outer planets are almost functionally identical, as expected. Only the outer planet results are plotted in Figure 2.4 for clarity.

A direct comparison of this derivation with that of Lithwick and Wu [2011] requires combining their Equations 1, 6, 15, and 33 to obtain an expression for $\dot{\Omega}$ and comparing that to this chapter's Equations 2.4 and 2.6 with $m_1 = 0$, $s_2 = 0$, and $e_2 = 0$. The general form of the solutions is similar, indicating dependence on $-e_1^2$ and s_1^2. The primary difference arises from the higher-order α terms in the f functions (see Appendix 2.8.1) and the explicit calculation of the Laplace coefficients. Figure 2.5 shows how terms that are negligible at low α become much stronger at higher α, as well as how the $b^{(1)}_{3/2} = \alpha$ approximation loses accuracy. Another difference arises from the dependence on ω_1, but this is negligible when $e_2 = 0$ (see Section 2.3.2 for details). Additionally, the Lithwick and Wu [2011] solution is only valid for a test particle and a circular massive planet, and several additional terms arise when considering the more general case of two planets with inclinations and eccentricities, including a significant dependence on the relative orientation of the orbits ($\omega_2 - \omega_1$).

It should be noted that Equations 2.4 to 2.7 use orbital elements taken relative to the central star (astrocentric). The default orbital elements in `REBOUND` are Jacobian. However, comparing the calculated analytical results for using Jacobian versus astrocentric coordinates in the unrestricted system has an effect no larger than 0.012% and on average 0.015%, so we did not recalculate the previously saved Jacobian elements and used them for all calculations. This effect could be more significant in other systems, particularly those with a higher planet-to-star mass ratio, and it is recommended to use astrocentric elements when applying the analytical solution.

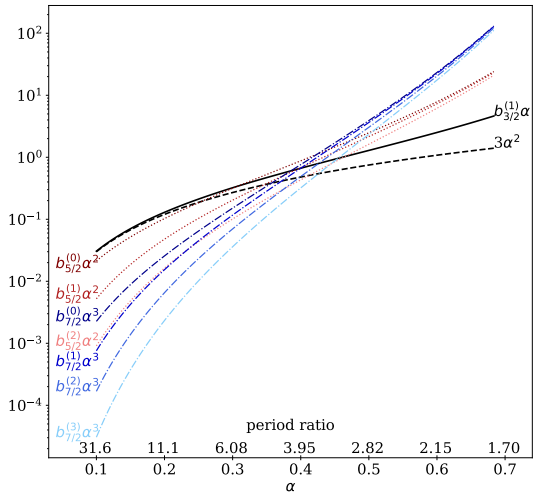

Figure 2.5: Calculated values for the Laplace coefficients terms with the lowest order of α that appears in Equations 2.4 to 2.7. The black line shows the $b^{(1)}_{3/2}\alpha$ term that appears in both this solution and in Lithwick and Wu [2011] as the $3\alpha^2$ approximation (black dashed line). The red dotted lines show the $b^{(j)}_{5/2}\alpha^2$ terms, with the darker shades showing lower values of j. The blue dashed-dotted lines show the same for the $b^{(j)}_{7/2}\alpha^3$ terms.

2.3.2 Time Dependence

The expressions for $\dot{\Omega}_1$ and $\dot{\Omega}_2$ depend on terms that change over time. In the secular regime, the semi-major axes (and therefore α) are constant, but inclination, eccentricity, and ω vary periodically. The change in inclination is small, but the variations in eccentricity and ω can be significant. The result of this change in orbital elements is to change the rate of nodal precession over time.

Using data from the three body simulations over time, we were able to examine the magnitude of this change by calculating the instantaneous analytical solution at each timestep. The data showed that the term contributing the most time variation arises from $\omega_2 + \omega_1$, and that the mean over time is driven by $\omega_2 - \omega_1$. Because the time variations are periodic on a shorter timescale than the nodal precession period, the mean analytical solution over time is the observed nodal precession period. Using the orbital elements from a single point in time can then produce an instantaneous analytical solution that varies from the mean underlying period by a potentially significant amount. However, this error is easily eliminated by removing the terms that vary on short timescales (these are the terms with $\cos(2\omega_1)$, $\cos(\omega_2 + \omega_1)$, and $\cos(2\omega_2)$ in Equations 2.4/2.5). This method of calculating $\dot{\bar{\Omega}}$ has been

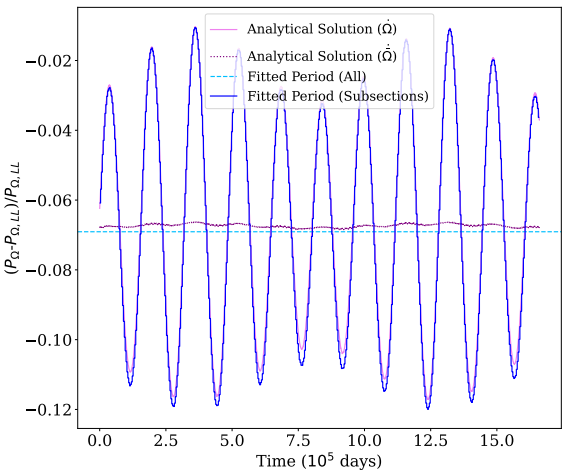

Figure 2.6: An example of how the analytical and simulated precession rate changes over time. For this simulation, $e_0 = e_{1,0} = e_{2,0}$ =0.07, i_0=2.6°, and P_2/P_1 = 2.6590. The instantaneous fourth-order analytical solution at each timestep is shown in solid pink. The mean fourth-order analytical solution at each timestep is shown in dotted purple. The light blue dashed line shows the period fitted from the analysis in Section 2.2.1 (this is the value plotted in Figure 2.4). The solid blue lines show a value for a fitted period within a shorter subset of the simulation time. The time variations are on a shorter timescale than the nodal precession period, $P_\Omega \approx 5.7 \times 10^5$ days.

used to calculate all the higher-order-α analytical solutions used in this chapter.

The variation of $\dot{\Omega}$ is also seen in the simulated data, confirmed by fitting periods to subsets of Ω over time. The period found via the analysis in Section 2.2.1 by fitting to the entire output dataset is the average period. As expected, this average period is very well-defined given the difference in time scales. An example from one simulation is shown in Figure 2.6 to illustrate. Using the mean analytical solution as described greatly reduces the time-variation of the calculated solution and provides an accurate average period from the system parameters at a single point in time.

2.3.3 Effect of General Relativity

General relativity predicts that the curvature of spacetime can lead to apsidal precession of planetary orbits [Einstein, 1916]. Given the dependence of the $\dot{\Omega}$ on ω, it is possible for this effect to couple to the nodal precession rate.

Calculating the predicted apsidal precession from general relativity and comparing it to the simulated apsidal precession rate, the general relativity effect only becomes comparable for period ratios $\gtrsim$10. Given that the effect of ω is much reduced at high period ratios, due

to the strong α dependence in those terms, neglecting general relativity (or other sources of extra apsidal precession) in our simulations is not expected to have a significant effect on our results.

2.4 Limits of Applicability

In many cases, the simpler nodal precession period given by Laplace-Lagrange theory is adequate. However, for cases where a more precise period is desired, a higher order approximation might be needed. To find the parameter space where the higher-order-α analytical solution given in Section 2.3 attains a high accuracy, over 9900 additional systems with higher inclinations and eccentricities were simulated. These systems were the same as those described in Section 2.2.2, except with a wider range of eccentricities and inclinations, going as high as 1.8 in combined eccentricity and 30 degrees in mutual inclination, although the majority were at combined eccentricities of $\leq$0.4 to determine the location of the transition for analytical accuracy. Many of the $\Sigma e_0 > 0.4$ systems were not stable, changing rapidly in semi-major axis.

Figure 2.7 shows the fraction of simulations per bin in combined eccentricity, mutual inclination, and period ratio space that were under a given threshold of accuracy. These distributions are for only for our one particular simulated system (see Section 2.2.2), and a simple one-dimensional distribution does not capture the more complicated interplay between the three parameters. However, this plot does provide a general guideline for when certain approximations are sufficient. As expected, the accuracy decreases for larger eccentricity and inclination and for smaller period ratio (larger α).

When high accuracy, within 1%, is desired, the higher-order-α approximation (Equations 2.4/2.5) is needed, especially for low period ratios ($\lesssim$4). For very low period ratios ($\lesssim$2.1), an N-body simulation is likely required unless the eccentricities and inclinations are low. The higher-order-α approximation is typically accurate for mutual inclinations $\lesssim$15°

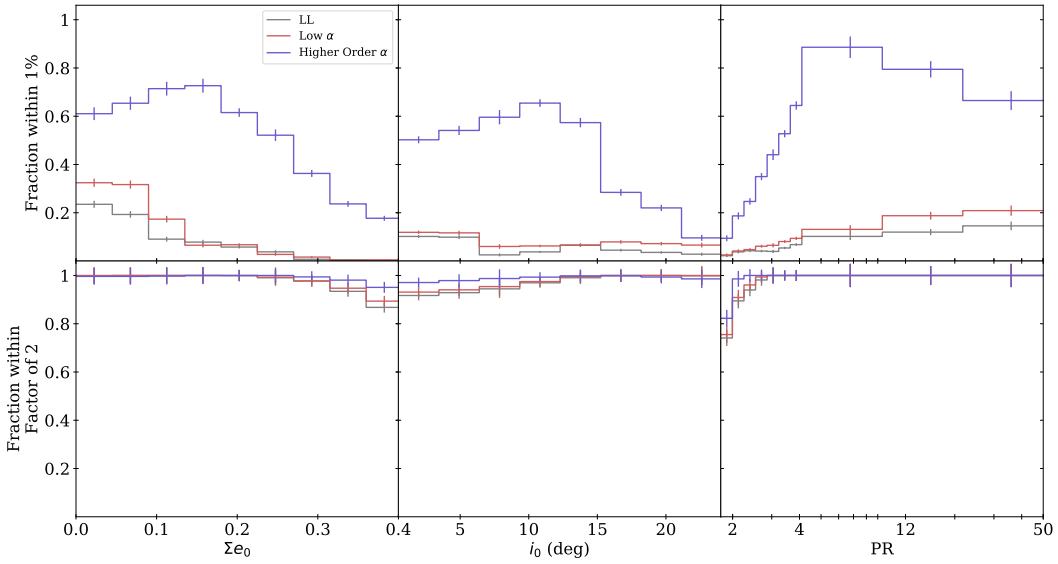

Figure 2.7: The fraction of simulations per bin that are below a given threshold of accuracy, where accuracy is calculated as $(P_{\Omega,sim} - P_{\Omega,model})/P_{\Omega,model}$ for three models: Laplace-Lagrange theory, low-α approximation [Lithwick and Wu, 2011], higher-order-α approximation (Section 2.3). Error bars on each bin are calculated from a binomial distribution.

and for a combined eccentricity $\lesssim$0.27. Across all stable simulations, the median accuracy of the higher-order-α approximation is 1.37%.

The choice of 1% as the threshold for high accuracy can be compared with scales of interest for application. For example, imposing a 1% error on the nodal precession frequency values when calculating the secular resonance location in the Kepler-117 system (see Section 2.6 for details) produces the same order of magnitude error that arises from observational uncertainty.

The location of the secular resonance, even with exactly known input parameters, has an intrinsic width. This width gives another scale for the accuracy of the nodal precession frequency, and here we have calculated it by finding where the inclination of a test particle is forced to three times its natural inclination (i.e., its forced inclination if the two perturbing planets were on fixed orbits) using linear theory. The width varies based on the system configuration. For example, in the Kepler-117 system, the secular resonance widths are of order 0.1 times the resonance location. A random 1% error on the nodal precession frequency would then always place the calculated resonance location inside of the actual resonance, with inaccurate placement beginning at about 3% error on the nodal precession frequency. To check the generality of this, we generated 100 random 2-planet systems. The relative resonance width (the width of the resonance divided by its location) was typically 0.1-0.2, with the inner resonance usually being larger by a factor of about 2-3, similar to the Kepler-117 system. High-α systems tended to the lower end of the range. Thus a 1% accuracy on the nodal precession frequency is adequate to ensure correctly identifying the predicted location of the secular resonance.

A more detailed examination of the applicable parameter space is shown in Figure 2.8. For high period ratios, the fourth-order analytical solution is very accurate up to $\sim$18° mutual inclination and over 0.4 in combined eccentricity. For lower period ratios, the region of parameter space where the model is accurate shrinks to lower mutual inclination and

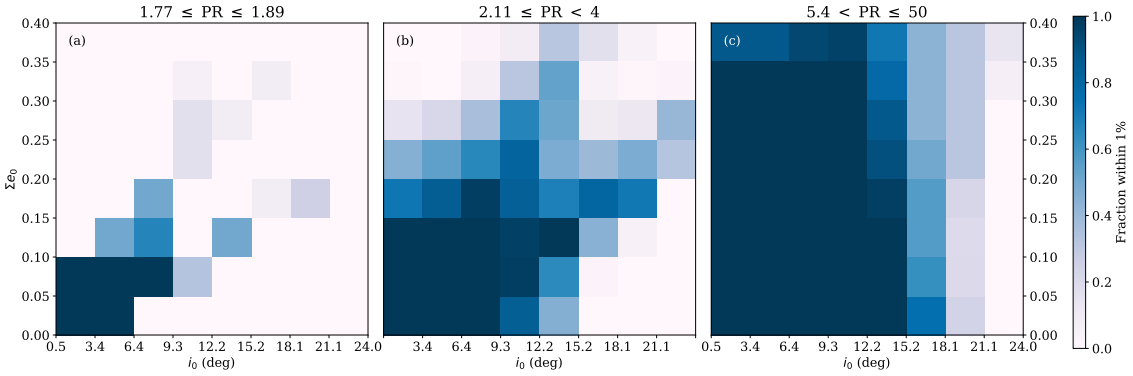

Figure 2.8: The fraction of simulations per bin that are accurate to within 1%, where accuracy is calculated as $(P_{\Omega,sim} - P_{\Omega,model})/P_{\Omega,model}$ for the higher-order-α approximation (Section 2.3). Shown for three different ranges of period ratio: (a) 1.77 to 1.89, (b) 2.11 to 4, and (c) 5.4 to 50.

combined eccentricity, as expected. There is also a region of moderate mutual inclination and combined eccentricity where the accuracy is very good. This region of accuracy arises due to the offsetting effects of inclination and eccentricity. For period ratios between 2.11 and 4, the model is accurate up to $\sim 15^\circ$ mutual inclination and ~ 0.2 in combined eccentricity. For very low period ratios, between 1.77 and 1.89, the model is accurate at mild mutual inclinations of $\leq 6^\circ$ and combined eccentricities of 0.1.

If only an order of magnitude estimate is needed for the nodal precession period, then linear Laplace-Lagrange theory suffices over almost the entire range examined: mutual inclinations up to 30° and combined eccentricity up to 0.4. For higher eccentricities, the accuracy is typically limited not by the analytical approximation but by instability, and this region of parameter space was not well-sampled, particularly at higher period ratios. Across all stable simulations, the median accuracy of the linear theory solution is 12.8%.

The consideration of nodal precession within a mean-motion resonance is beyond the scope of this chapter. We have considered only period ratios well away from a mean-motion resonance, but have not carefully defined where the transition between resonant and non-resonant nodal precession behavior occurs.

We have considered here primarily a single system with a low planet-to-star mass ratio ($\sim 6 \times 10^{-5}$) and planets of similar masses (~ 0.91 mass ratio). A small set of preliminary simulations of a system with the same planetary mass ratio but a higher planet-to-star mass ratio ($\sim 6 \times 10^{-3}$) and a system with the same planet-to-star mass ratio but differing planetary masses (~ 0.54 mass ratio) showed similar behavior to that seen here. Additionally, the dynamics of a planetary system are expected to be scale invariant, and so these effects are expected to be independent of the absolute semi-major axes of the planets. Thus we expect that these results are generally applicable.

2.5 Application to Kepler Population

To estimate the effect on a population of multiplanet systems like those found in the Kepler mission (e.g. Fabrycky et al. 2014), we drew 10^5 samples from a period ratio distribution, inclination distribution, and eccentricity distribution that describes the Kepler multiplanet systems. The period ratio samples were drawn from a log-uniform distribution in between 1.2 and 4, resampling any period ratios that fell within 0.1 of a 1st or 2nd order resonance or within 0.05 of a 3rd order resonance (ensuring $|P_2/P_1 - M/N| \geq 0.1$ for $M = N + 1$ and $M = N + 2$ and $|P_2/P_1 - M/N| \geq 0.05$ for $M = N + 3$). The mutual inclinations were drawn from a Rayleigh distribution with scale $\sigma = 0.032$ radians [Fabrycky et al., 2014], and the eccentricities were drawn from a Rayleigh distribution with scale $\sigma = 0.049$ [Van Eylen and Albrecht, 2015]. The resulting sample distributions are shown in Figure 2.9.

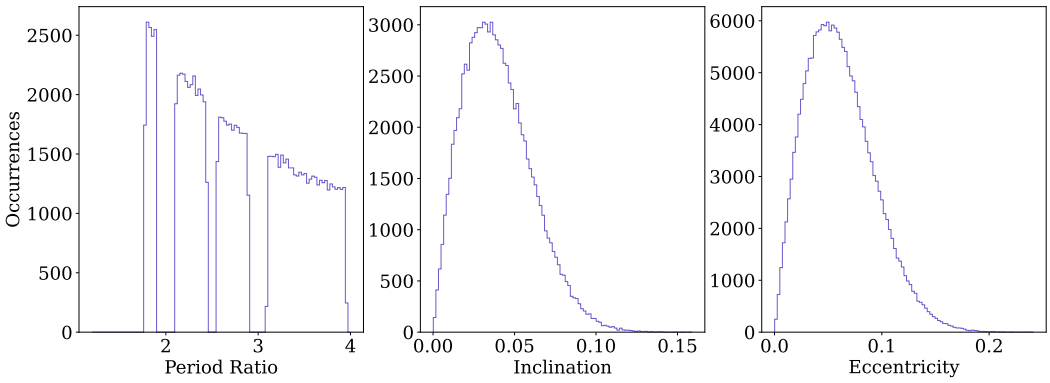

Figure 2.9: Distributions of period ratio, mutual inclination, and eccentricity drawn for a population of Kepler-like multiplanet systems.

In order to calculate the expected nodal precession deviation given by the analytical solution in Section 2.3, system properties including stellar and planetary masses, inner planet period, and arguments of pericenter are needed. For the purposes of finding trends from inclination, eccentricity, and semi-major axis ratio, the calculation was repeated 100 times for each set of e, i, and α with random draws of the remaining parameters. The effect of the masses and inner planet period are expect to scale away and should not affect the resulting

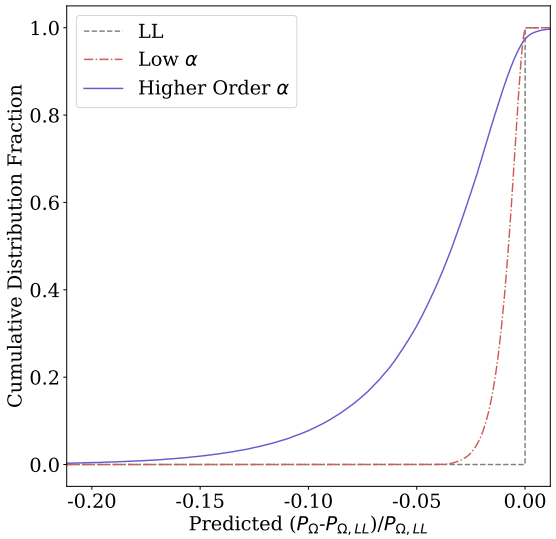

Figure 2.10: Cumulative distribution of expected deviation of nodal precession period from the linear theory prediction for the sample of Kepler-like multiplanet systems for our model (solid blue) and the $\alpha \ll 1$ prediction from Lithwick and Wu [2011] (dash-dot red). The reference linear theory at zero is shown in dashed gray. The x-axis limits are the 0.3 and 99.7 percentiles of the fourth-order model distribution.

calculation.

The period ratio was converted to α using Equation 2.3. Each planet's eccentricity was drawn individually, and their inclinations were calculated from the mutual inclination such that the reference plane was the invariable plane. The analytical solution was calculated as described in Section 2.3.2 to remove the time-dependent effect of the arguments of pericenter.

The resulting expected deviations from the linear theory prediction are shown in Figure 2.10, along with the predictions from the $\alpha \ll 1$ case from Lithwick and Wu [2011]. To calculate the distribution, only sets of e, i, and α where the combined eccentricity is <0.27 and the mutual inclination is $<15^\circ$ (where the analytical solution is expected to be accurate) are used, and the median nodal period from the 100 sub-samples for each set are used to calculate the distribution. The spread of deviations is much wider when the higher order effects are taken into account using our solution, varying up to tens of percent and with *approximately 50% having greater than 5% deviation from linear theory*. Therefore, for precision work on realistic planetary systems, a higher-order theory than linear Laplace-Lagrange theory is essential.

2.6 Secular Resonance

For a test particle in a system with two planets, it will experience a large forced inclination at locations where its secular frequency is equal to the planets' nodal precession frequency. In Laplace-Lagrange theory, the test particle's secular frequency can be calculated as:

$$B = -n\frac{1}{4}\sum_{j=1}^{2}\frac{m_j}{M_\star}\alpha_j\bar{\alpha_j}b_{3/2}^{(1)}(\alpha_j) \tag{2.8}$$

[Murray and Dermott, 1999, Equation 7.57]. This frequency is equal to the sum of the linear theory frequencies of each test particle-planet pair. Replacing the linear theory frequency instead with the fourth-order frequency calculated from Equations 2.4/2.5, we can calculate how the expected location of the secular resonance will change.

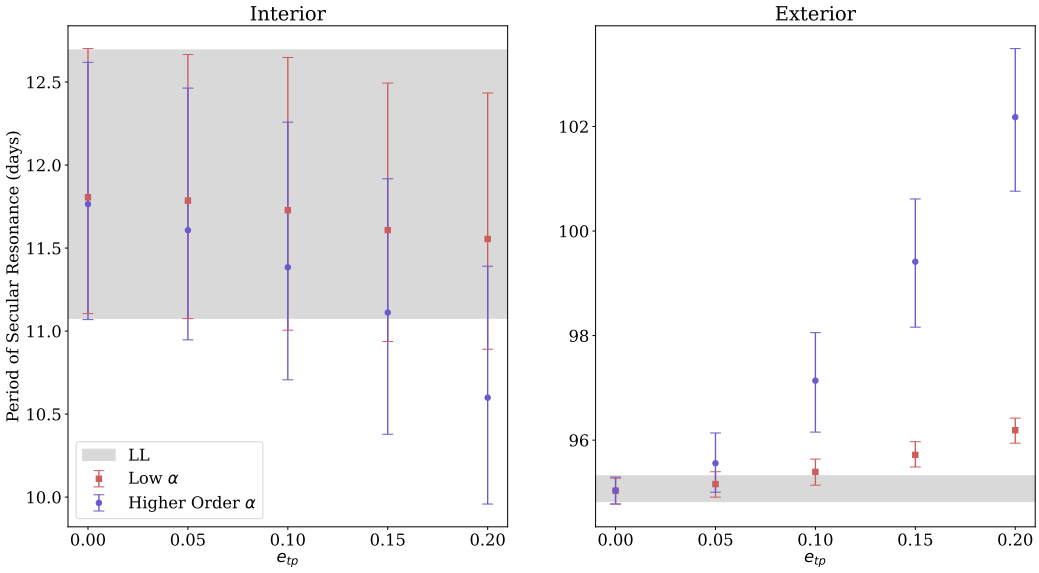

Figure 2.11: Predicted location of the secular resonance locations of a test particle in the Kepler-117 system. Error bars show the 68% interval around the median value.

To examine the secular resonance locations, we looked at the Kepler-117 system. This is a 2-planet system at a low period ratio, not in mean-motion resonance, with known masses

Table 2.3: Kepler-117 system parameters from Bruno et al. [2015]. Angles marked with an asterisk are referenced to the invariable plane, assuming $\Omega_b = \Omega_c = 0$ in the sky plane and $\Delta\Omega = 180^\circ$ in the invariable plane.

Stellar Mass	$1.129^{+0.13}_{-0.023}\ M_\odot$	
Planet:	**b**	**c**
P (days)	18.7959228(75)	50.790391(14)
a (AU)	$0.1445^{+0.0047}_{-0.0014}$	$0.2804^{+0.0014}_{-0.0028}$
m (M_J)	0.094 ± 0.033	1.84 ± 0.18
e	0.0493 ± 0.0062	0.0323 ± 0.0033
ω (deg)	254.3 ± 4.1	305.0 ± 7.5
	74.3 ± 4.1 *	304.6 ± 11.4 *
i (deg)	88.74 ± 0.12	89.64 ± 0.10
	0.87 ± 0.16 *	0.032 ± 0.01 *

and orbits. The planetary properties and stellar mass are taken from Bruno et al. [2015, Table 3] and summarized here in Table 2.3. The system is rotated into the invariable plane for each calculation.

We account for observational uncertainties by making a sample of 1000 sets of system properties drawn from normal distributions based on the published best fit values and uncertainties. We also account for the possible orientation of the test particle by sampling for 30 ω values. The test particle is placed in the system's invariable plane, and the linear, second-order, and fourth-order solutions are calculated with various eccentricities of the test particle. Results are shown in Figure 2.11.

For the interior resonance, observational uncertainty is large enough that the higher order solutions are not separated from the linear theory solution. The uncertainty for this resonance is dominated by the uncertainty in the mass measurement of Kepler-117 b, and improved observations could result in differentiation between the models. For the exterior resonance, the difference in location in the higher order solutions is significant from that of linear theory. The uncertainty for this resonance is dominated by the hypothetical orientation (ω) of the test particle and not the observational uncertainties.

Because of the large inclination expected for a test particle in secular resonance, accu-

rately understanding the location of the secular resonance can help predict where planets might be expected to be transit. The dependence on eccentricity could provide a constraint on the eccentricity of a transiting planet near the resonance location.

Additionally, secular resonances within a system, both in the nodal and apsidal frequencies, can interact and lead to chaos when they overlap [Lithwick and Wu, 2011, Lithwick and Wu, 2014]. These overlapping secular resonances could lead to systems maintaining marginal stability over their lifetimes; for example, Mercury in the present-day Solar System [Laskar, 1996]. Understanding the impact of higher-order effects on the location and width of secular resonances could lead to a better understanding and prediction of exoplanet system architectures.

2.7 Conclusions

We used numerical and analytical methods to probe the nodal precession rate of exoplanet systems. From our simulated systems, we find that the second-order nonlinear nodal precession rate given by Lithwick and Wu [2011] is a good approximation when $\alpha \ll 1$. However, the sensitivity of this precession rate to inclination and eccentricity is a factor of several times more for period ratios relevant to the planetary systems observed by Kepler (see Section 2.5). Inclination values of a few degrees and eccentricity values of a few percent are expected to change the nodal rates by a few or even tens of percent. Given that the dependence is on the square of these quantities, the effect would be even more significant at higher values of inclination and eccentricity.

We present a higher-order nonlinear solution for the nodal precession rate, using Murray and Dermott [1999]'s expansion of the disturbing function to fourth order in eccentricity and inclination, maintaining all associated α terms. We find that this solution is a good descriptor of nodal precession rates for simulated systems with moderate eccentricity and inclination at a wide range of period ratios (see Section 2.4).

The locations and widths of secular resonances in Kepler-like systems could deviate significantly from that expected from linear theory, as seen in the expected locations of the inclination-node secular resonances for an eccentric test particle in the Kepler-117 system. Further, the overlap of secular resonances can lead to secular chaos in exoplanet systems, which could drive architecture ordering as systems maintain marginal stability on the edge of the overlapping secular resonances. Understanding the nonlinearity of precession rates is critical to understanding the interaction of secular resonances and their effect on exoplanet system architectures.

2.8 Appendix

2.8.1 Expressions of $f(\alpha)$

These expressions make use of of the Laplace coefficients $b_s^{(j)}$, defined as

$$b_s^{(j)}(\alpha) = \frac{1}{\pi}\int_0^{2\pi} \frac{cos\, j\psi \,\mathrm{d}\psi}{(1-2\alpha cos\psi+\alpha^2)^s}. \tag{2.9}$$

$$f_3 = -\tfrac{1}{2}\alpha b_{3/2}^{(1)} \tag{2.10}$$

$$f_7 = \tfrac{1}{16}\Big[-4\alpha b_{3/2}^{(1)} - 12\alpha^2(b_{5/2}^{(0)}+b_{5/2}^{(2)}) + 30\alpha^3 b_{5/2}^{(1)} \\ -\tfrac{15}{2}\alpha^3(b_{7/2}^{(3)} - 4\alpha b_{7/2}^{(2)} + (4\alpha^2+3)b_{7/2}^{(1)} - 4\alpha b_{7/2}^{(0)})\Big] \tag{2.11}$$

$$f_8 = \tfrac{3}{4}\alpha^2\left(\tfrac{1}{2}b_{5/2}^{(2)} + b_{5/2}^{(0)}\right) \tag{2.12}$$

$$f_9 = \tfrac{1}{4}\alpha\left(2b^{(1)}_{3/2} + 3\alpha b^{(2)}_{5/2} + 15\alpha b^{(0)}_{5/2}\right) \tag{2.13}$$

$$\begin{aligned} f_{13} = \tfrac{1}{8}\Big[&6\alpha^2(b^{(3)}_{5/2} + 3b^{(1)}_{5/2}) - 15\alpha^3(b^{(2)}_{5/2} + b^{(0)}_{5/2}) \\ &+\tfrac{15}{4}\alpha^3(b^{(4)}_{7/2} - 4\alpha b^{(3)}_{7/2} + (4\alpha^2+4)b^{(2)}_{7/2} - 12\alpha b^{(1)}_{7/2} + (4\alpha^2+3)b^{(0)}_{7/2})\Big] \end{aligned} \tag{2.14}$$

$$f_{14} = \alpha b^{(1)}_{3/2} \tag{2.15}$$

$$\begin{aligned} f_{15} = \tfrac{1}{4}\Big[&2\alpha b^{(1)}_{3/2} + 6\alpha^2(b^{(0)}_{5/2} + b^{(2)}_{5/2}) - 15\alpha^3 b^{(1)}_{5/2} \\ &+\tfrac{15}{4}\alpha^3\left(b^{(3)}_{7/2} - 4\alpha b^{(2)}_{7/2} + (4\alpha^2+3)b^{(1)}_{7/2} - 4\alpha b^{(0)}_{7/2}\right)\Big] \end{aligned} \tag{2.16}$$

$$f_{16} = -\alpha\left(\tfrac{1}{2}b^{(1)}_{3/2} + 3\alpha b^{(0)}_{5/2} + \tfrac{3}{2}\alpha b^{(2)}_{5/2}\right) \tag{2.17}$$

$$\begin{aligned} f_{18} = \tfrac{1}{16}\Big[&12\alpha b^{(1)}_{3/2} + 12\alpha^2(b^{(2)}_{5/2} + b^{(0)}_{5/2}) - 27\alpha^3 b^{(1)}_{5/2} \\ &+\tfrac{15}{4}\alpha^3\left(b^{(3)}_{7/2} - 4\alpha b^{(2)}_{7/2} + (4\alpha^2+3)b^{(1)}_{7/2} - 4\alpha b^{(0)}_{7/2}\right)\Big] \end{aligned} \tag{2.18}$$

$$f_{19} = \tfrac{1}{8}\left[-12\alpha^2 b^{(1)}_{5/2} + 15\alpha^3 b^{(2)}_{5/2} - \tfrac{15}{4}\alpha^3\left(2b^{(2)}_{7/2} - 8\alpha b^{(1)}_{7/2} + (4\alpha^2+2)b^{(0)}_{7/2}\right)\right] \tag{2.19}$$

$$f_{20} = \tfrac{1}{16}\left[\tfrac{15}{4}\alpha^3\left(b^{(3)}_{7/2} - 4\alpha b^{(2)}_{7/2} + (4\alpha^2+3)b^{(1)}_{7/2} - 4\alpha b^{(0)}_{7/2} - 4/5 b^{(1)}_{5/2}\right)\right] \tag{2.20}$$

$$f_{21} = -2f_{18} \tag{2.21}$$

$$f_{22} = 2f_{19} \tag{2.22}$$

$$\begin{aligned} f_{23} = \tfrac{1}{4}\Big[&-6\alpha^2(b^{(1)}_{5/2} + b^{(3)}_{5/2}) + 15\alpha^3 b^{(2)}_{5/2} \\ &-\tfrac{15}{4}\alpha^3\left(b^{(4)}_{7/2} - 4\alpha b^{(3)}_{7/2} + (4\alpha^2+2)b^{(2)}_{7/2} - 4\alpha b^{(1)}_{7/2} + b^{(0)}_{7/2}\right)\Big] \end{aligned} \tag{2.23}$$

$$f_{24} = -2f_{19} \tag{2.24}$$

$$f_{25} = -2f_{20} \tag{2.25}$$

$$f_{26} = \tfrac{1}{2}\alpha\left(b^{(1)}_{3/2} + \tfrac{3}{2}\alpha b^{(0)}_{5/2} + 3\alpha b^{(2)}_{5/2}\right) \tag{2.26}$$

2.8.2 Tabulated Results

P_1 (d)	P_2 (d)	Period Ratio	$e_{1,0}$	$e_{2,0}$	$i_{1,0}$ (rad)	$i_{2,0}$ (rad)	$\omega_{1,0}$ (rad)	$\omega_{2,0}$ (rad)	$P_{\Omega,2}$ (d)	$\sigma_{P_{\Omega,2}}$ (d)	$t_{\rm stable}$ (d)	$t_{\rm sim}$ (d)	$P_{\Omega,\rm LL}$ (d)	$P_{\Omega,\rm 2nd}$ (d)	$P_{\Omega,\rm 4th}$ (d)	Figures Used
3.48	6.17	1.77	2.09E-16	4.49E-17	0	0.0407	0.827	1.094	122124.51	0.00238	616559.81	616559.81	121025.25	121125.7	122162.63	1,3
3.48	6.32	1.816	2.09E-16	0.033	0	0.0457	0.827	1.094	135455.84	0.01463	632497.09	632497.09	135768.52	135834.68	135521.25	3
3.48	7.33	2.105	2.09E-16	6.33E-17	0	0.0696	0.827	1.094	253685.21	0.03683	109987.5	109987.5	249262.47	249867.71	253485.62	1,3
3.48	7.67	2.201	2.09E-16	0.085	0	0.1047	0.827	1.094	290324.28	0.16596	766868.72	766868.72	295058.11	295605.46	289729.69	3
3.48	8.15	2.339	2.09E-16	0.1	0	0.0457	0.827	1.094	345870.47	0.30217	814679.14	814679.14	367177.73	365730.4	346743.21	3
3.48	9.26	2.659	2.09E-16	0.067	0	0.0087	0.827	1.094	555062.52	0.17255	926234.47	926234.47	568096.28	566858.18	555203.21	1,3
3.48	11.15	3.201	2.09E-16	0.067	0	0.0457	0.827	1.094	1001488.27	0.26432	1115209.17	1115209.17	1016797.08	1015599.07	1001465.71	3
3.48	11.47	3.293	2.09E-16	0.085	0	0.0407	0.827	1.094	1076858.79	0.43548	1147082.32	1147082.32	1106370.23	1103278.56	1077204.18	3
3.48	26.2	7.521	2.09E-16	0.033	0	0.0727	0.827	1.094	10254247.81	0.33899	2619938.2	2619938.2	10240518.29	10261952.35	10252821.81	3
3.48	174.17	50	2.09E-16	0.1	0	0.1047	0.827	1.094	947110434.65	1.01768	17417019.8	17417019.8	961145943.34	961610510.41	947155267.41	3

Note: Table 2.4 is published in its entirety in the machine-readable format. A random subset of rows are shown here for guidance regarding its form and content.

Table 2.4: Restricted Simulations Data

P_1 (d)	P_2 (d)	Period Ratio	$e_{1,0}$	$e_{2,0}$	$i_{1,0}$ (rad)	$i_{2,0}$ (rad)	$\omega_{1,0}$ (rad)	$\omega_{2,0}$ (rad)	$P_{\Omega,1}$ (d)	$\sigma_{P_{\Omega,1}}$ (d)	$P_{\Omega,2}$ (d)	$\sigma_{P_{\Omega,2}}$ (d)	$t_{\rm stable}$ (d)	$t_{\rm sim}$ (d)	$P_{\Omega,\rm LL}$ (d)	$P_{\Omega,\rm 2nd}$ (d)	$P_{\Omega,\rm 4th}$ (d)	Figures Used
6.24	11.05	1.77	2.95E-07	3.57E-07	0.00497	0.00376	-1.202	-1.489	141663.88	0.00276	141663.88	0.00276	1105326.61	1105326.61	141883.75	141889.15	141945.60	2,4,6,7
6.24	16.89	2.705	0.112	0.112	0.11861	0.07770	2.556	2.144	577689.39	3.92005	577691.82	3.92102	1689057.79	1689057.79	648060.03	644268.54	573627.92	6,7
6.24	16.89	2.705	0.149	0.149	0.19252	0.12583	2.558	2.146	584151.97	7.40156	584158.33	7.39694	1689057.79	1689057.79	648060.03	652144.30	560039.82	6,7
6.24	18.03	2.888	1.99E-05	2.40E-05	0.02781	0.01785	-1.202	-1.489	791773.06	0.01935	791773.17	0.01936	1803337.58	1803337.58	788337.06	789159.83	791589.78	2,4,6,7
6.24	19.99	3.201	0.099	0.099	0.15899	0.09833	2.558	2.147	1049403.61	6.96787	1049428.86	6.98544	1999266.84	1999266.84	1060123.12	1074537.96	1041708.09	6,7
6.24	20.85	3.339	8.85E-07	1.07E-06	0.00541	0.00331	-1.202	-1.489	1191726.67	0.00915	1191726.70	0.00915	2084977.93	2084977.93	1191449.91	1191495.27	1191594.60	2,4,6,7
6.24	21.71	3.476	0.200	0.200	0.02848	0.01718	2.554	2.142	815342.02	14.11037	815342.06	14.11079	2170686.53	2170686.53	1330353.71	1233025.66	895405.98	6,7
6.24	24.85	3.979	0.112	0.112	0.12457	0.07172	2.557	2.145	1769718.56	16.38353	1769718.22	16.41041	2484957.20	2484957.20	1904627.02	1893673.45	1765846.63	6,7
6.24	64.41	10.313	0.084	0.084	0.11679	0.04892	2.560	2.149	17709895.06	73.78958	17709940.33	74.17984	93574880.08	93574880.08	18050503.76	18041931.10	17708250.30	6,7
6.24	121.10	19.392	8.04E-05	9.72E-05	0.03039	0.01034	-1.202	-1.489	71090700.91	0.25767	71090774.55	0.75852	361761267.20	361761267.20	71020986.85	71079921.86	71097363.14	2,4,6,7
6.24	13.18	2.11	0.900	0.900	0.02378	0.01695	2.554	2.142	nan	nan	nan	nan	2945.05	1317649.72	285089.41	108849.70	5453.29	
6.24	312.24	50	0.066	0.066	0.08389	0.02077	2.561	2.149	514094177.93	142.50032	514102083.46	146.94138	2547874656.26	2547874656.26	520413164.36	518753723.38	514589013.77	4,6,7

Note: Table 2.5 is published in its entirety in the machine-readable format. A random subset of rows are shown here for guidance regarding its form and content.
A nan value for the simulated precession period indicates that a sinusoid could not be fit to the Ω data, usually in the case of non-secularly stable systems.

Table 2.5: Unrestricted Simulations Data

CHAPTER 3

PERIOD RATIO SCULPTING NEAR SECOND-ORDER MEAN-MOTION RESONANCES

Second-order mean-motion resonances lead to an interesting phenomenon in the sculpting of the period ratio distribution due to their shape and width in period-ratio/eccentricity space. As the osculating periods librate in resonance, the time-averaged period ratio approaches the exact commensurability—that is, the period ratio where mP_1 exactly equals $(m-2)P_2$ for a $m : m-2$ (second order) resonance. The width of second-order resonances in period ratio increases with increasing eccentricity, and thus more eccentric systems have a stronger peak at commensurability when averaged over sufficient time. The libration period is short enough that this time-averaging behavior is expected to appear on the timescale of the Kepler mission.

Using N-body integrations of simulated planet pairs near the 5:3 and 3:1 mean-motion resonances, I investigated the eccentricity distribution consistent with the planet pairs observed by the Kepler survey. This analysis, an approach independent from previous studies, shows no statistically significant peak at the 3:1 resonance and a small peak at the 5:3 resonance, placing an upper limit on the Rayleigh scale parameter, σ, of the eccentricity of the observed Kepler planets at $\sigma = 0.245$ (3:1) and $\sigma = 0.095$ (5:3) at 95% confidence, consistent with previous results from other methods.

This chapter first appeared in *The Astronomical Journal* as Bailey et al. [2022]. The majority of the work described in this paper was performed by me under the guidance and supervision of my advisor (last author). The second author assisted with the TTV analysis, editing of the paper, and a large section on new TTV measurements that was deferred to another paper.

3.1 Introduction

The interactions between two planets orbiting a star become especially strong when the planets' periods are integer multiples of one another. These period commensurabilities are called mean-motion resonances (MMRs), and their order is determined by the difference in the integer multiples; e.g. a first-order resonance has an $m : (m - 1)$ period ratio. Different order MMRs have different characteristics, and in this chapter we will examine how the symmetrical shape of second-order MMRs affects the aggregate period ratio distribution for a population of planets.

A general overview of MMRs is given in Murray and Dermott [1999] and a recent detailed analytical treatment can be found in Hadden [2019]. An analysis of the period ratio distribution of Kepler multi-transiting systems, including features related to MMRs, was in Fabrycky et al. [2014].

When planets are in resonance, their orbital periods vary. The typical rate at which this variation occurs is faster than the orbital precession by a factor of $\sqrt{M_\star/m_p}$ [Murray and Dermott, 1999]. Therefore, to keep the resonant angles in a librating state, the orbital period ratio averages to very close to the ratio of integers that defines the resonance.

Orbital eccentricities play a role in the maintenance of a resonance, because it is the eccentricity that supplies torque between two planets [Peale, 1976]. Therefore, the more eccentric the planets of a system are, the more likely they will be in resonance, and the more likely their period ratios will average out to the nominal value of the resonance. The high-order resonances are more sensitive to eccentricity; the strength of the coupling is proportional to the eccentricity to the power of the order of the resonance [Murray and Dermott, 1999].

Eccentricities are challenging to measure for transiting exoplanets. The transit timing variation (TTV) method is the most precise for measuring eccentricities, but it favors planets near first-order MMRs and presents a degeneracy between mass and eccentricity [Lithwick

et al., 2012].

Examining the effect of eccentricity on transit durations is a more general but less precise technique. Fabrycky et al. [2014] (building on Moorhead et al. [2011]) compared transit durations between planets in the same system to derive a typical Rayleigh scale. Ford et al. [2008] proposed a similar technique with dependence on the stellar density; later studies were able to apply this technique as improved stellar parameters became available [Van Eylen and Albrecht, 2015, Xie et al., 2016, Van Eylen et al., 2019, Mills et al., 2019].

Shabram et al. [2016] used transit and occultation detections to measure projected eccentricity via transit duration ratios and phase offsets, independent of the stellar density, but this probes generally the Hot Jupiter population.

Alternatively, forward modeling can use observed populations to constrain intrinsic population distributions, e.g. He et al. [2019, 2020].

The general picture that has emerged from these studies are that multi-planet systems of small (i.e. non-giant) exoplanets tend to have low eccentricities. Both multi-planet giant systems, such as those probed by radial velocity measurements, and single-planet systems tend to have a distinctly excited eccentricity distribution compared to multi-planet sub-giant systems.

We develop a new method to measure the eccentricity distribution of multi-planet systems observed by Kepler using second-order MMRs. This method has different associated systematics and does not depend on precisely measured stellar properties or specific transit observations. Although this method relies on MMRs, given that migration likely doesn't easily trap planets in second-order MMRs [Delisle et al., 2014, Migaszewski, 2015, Xu and Lai, 2017], we expect it traces post-scattering systems.

The structure of this chapter is as follows: Section 3.2 discusses the methodology used to generate and analyze our simulated systems; the results are covered in Section 3.3; an analytical approximation is discussed in Section 3.4; Section 3.5 discusses the importance of

the results and further considerations, including consideration of the TTVs of the observed planets in K02261; and Section 3.6 summarizes our key findings.

3.2 Methods

For our investigation, our goal was to create a synthetic population of planet pairs that was similar to those found in the Kepler sample. We intentionally emulate the properties of the sample as observed; i.e., we seek to probe the observed distribution and not the intrinsic distribution. To isolate the effects of eccentricity, we use a wide variety of planet pairs like those observed by Kepler to marginalize over other factors, particularly the mass which has a strong degeneracy with eccentricity in MMRs (see Section 3.5.4). We then seek to quantitatively compare the resulting second-order MMR peaks at 3:1 and 5:3 for various eccentricity distributions, particularly in comparison to that of the Kepler sample.

3.2.1 System Generation

In order to numerically investigate planetary behavior near the second-order MMRs, we needed a population of planet pairs. Our intent was to create a population that was similar to that of Kepler, although without being rigorously Kepler-like.

To develop a population of planet pairs near the 5:3 and 3:1 MMRs, we first randomly generated a large number of planet pairs evenly in period ratio near the commensurability location. The mutual inclination of the two planets was chosen randomly from a Rayleigh distribution with scale 0.032 radians [Fabrycky et al., 2014]. The inner planet period, each planet mass, and the stellar mass were randomly assigned using distributions based on the population of multi-planet systems observed by Kepler. Arguments of pericenter were chosen uniformly between $-\pi$ and π.

This set of generated planet pairs is intended to be used to probe pairs at various eccentricities. Therefore, to ensure a wide coverage of eccentricity, several methods of assigning

eccentricities were used, including uniformly between 0 and 1, uniformly between 0 and 0.5, and linearly decreasing from 0 to 0.5. For each planet pair, multiple systems were created varying only in the mean longitude of the planets.

This initial population of planet pairs was then integrated for 10^6 orbits of the outer planet to remove any "unstable" pairs. In this context, pairs were considered unstable when they departed from the period ratio range of interest and not as a strict determination of instability. The bounds at which pairs were removed were <2.5 or >3.5 for the 3:1 resonance and <1.55 or >1.88 for the 5:3 resonance. The integrations were computed using the IAS15 integrator in the `REBOUND` package [Rein and Liu, 2012, Rein and Spiegel, 2015].

At the end of the first stability run, 50 surviving systems were randomly chosen for each resonance to be integrated for ten times longer. Of these 50 systems, an additional 4 went "unstable" (departed the specified period ratio bounds) for the 3:1 systems and an additional 8 for the 5:3 systems, with no apparent preferential location in period ratio. These low percentages indicated that the initial stability run was sufficient to ensure a robust sample that would not be dominated by planet pairs on the verge of instability.

From the planet pairs that remained in the sample after the stability cut, one pair was randomly chosen from each initial set of mean-longitude systems to be used in the analysis, and thus each pair used in the analysis has unique parameters. Finally, of these pairs, those that had an average period ratio in close proximity to exact commensurability were selected for the analysis. This last cut was done between 2.94 and 3.06 for the 3:1 resonance (3.00 ± 0.06) and between 1.62 and $1.71\bar{3}$ for the 5:3 resonance ($5/3 \pm 7/150$). The limits are chosen to be wide enough to capture the expected resonant behavior but narrow enough not to include additional higher-order resonances. Specifically, the limits around the 5:3 were chosen to exclude the 8:5 and 7:4 mean-motion resonances.

Detailed distributions of the properties of the final generated sets of 913 (near 3:1) and 670 (near 5:3) planet pairs are shown in Appendix 3.7.2.

3.2.2 Analysis

The final results of simulations described in Section 3.2.1 provide an instantaneous snapshot of the orbital properties of the planet pairs. These properties change over time, however, as the planets perturb each other, particularly planets that are caught in the mean-motion resonance and librate around a fixed point configuration. Given the time baseline of the Kepler mission, we can actually observe the average orbital properties. Thus the first step of the analysis was to integrate each planet pair for 3.5 years and to time-average the osculating orbital properties over this period. This is done by saving the orbital properties at 2000 steps during the 3.5 year integration and then taking the mean.

The approximate TTV period of planets near a $m : n$ mean-motion resonance is given by Deck and Agol [2016]:

$$P_{TTV} = \left| \frac{m}{P_2} - \frac{n}{P_1} \right|^{-1}, \tag{3.1}$$

and pairs actually in the resonance will experience libration around the center of the resonance on a timescale shorter than that [Nesvorný and Vokrouhlický, 2016]. Calculating the TTV period for the final planet pairs in our set of generated systems and comparing to the time-averaging period of 3.5 years, we find that the majority of these planet pairs, 54.2% for the 3:1 and 81.8% for the 5:3, will have completed at least one libration cycle. We can also calculate an analytical approximation of the libration periods with the Andoyer module of the `celmech` package. This predicts a libration period of less than 3.5 years for 31.2% for the 3:1 pairs and 55.7% for the 5:3 pairs. Note however that this approximation generally assumes low eccentricities, which is not the case for many of these pairs. Thus we expect that for both generated populations, the average period ratio would fall much closer to the nominal resonance period ratio than the instantaneous period ratio.

This peaking can be seen in Figure 3.1. There is also some stability sculpting from the initial uniform period ratio distribution (see Figure 3.21). This sculpting is expected, as

being near resonance can increase instability, but being in resonance can provide protection against instability, thus leading to an excess of planet pairs near each resonance. However, at any random point, the peak of the excess planet pairs is much more spread out and indistinct than the time-averaged peak. This narrow time-averaged peak is a distinct signature, and is even expected when there is no excess planet pairs (see Figure 3.9). In our generated systems, we find that no more than approximately one-third of the planet pairs located in the time-averaged peak can be attributed to a stability-induced excess. Thus the effect of sculpting from instability is both expected in real populations and not necessary for the appearance of the time-averaged resonant peak.

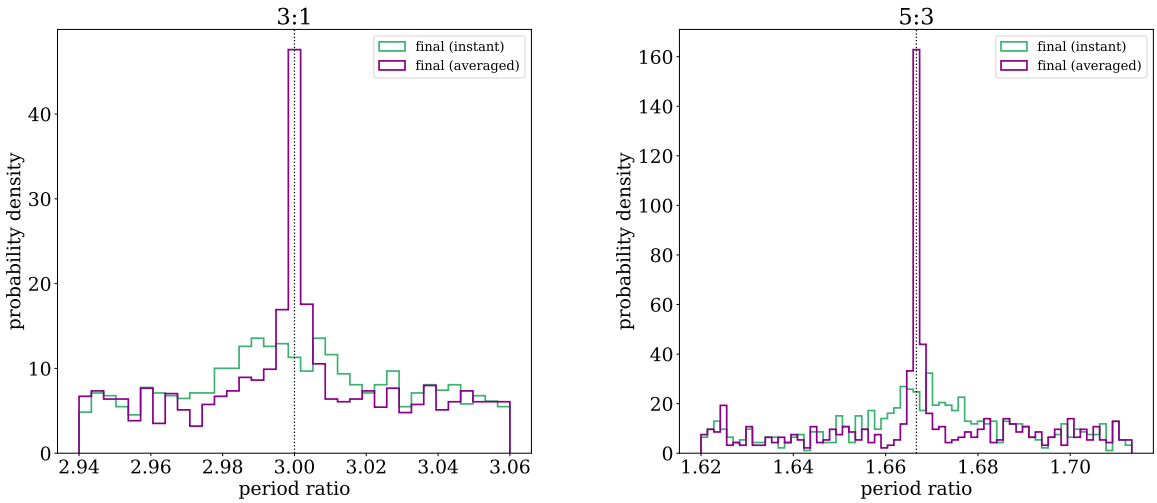

Figure 3.1: The probability density of period ratios near the (left) 3:1 and (right) 5:3 mean-motion resonances. The nominal resonance value is marked with a dotted line. The instantaneous final and averaged final distributions are shown for the specified set of generated systems as described in Section 3.2.1. There is an excess of planet pairs due to the resonance seen in the instantaneous distribution (a result of stability sculpting), but the signal of interest is the narrow peak that is clearly revealed by time-averaging.

3.2.3 Model

To quantify the size and shape of this peak, we use a model comprised of a linear background and a Gaussian peak centered on the nominal resonance value. The normalized equation for

this model is

$$P(r) = \frac{c_1(r - r_0) + c_2\mathcal{N}(r_0, c_3) + 1}{\int_{r_{min}}^{r_{max}} (c_1(r - r_0) + c_2\mathcal{N}(r_0, c_3) + 1)\, dr}, \tag{3.2}$$

and it has three parameters to be fitted: c_1, c_2, and c_3, where c_1 is the slope of the linear background distribution, c_2 is the amplitude of the Gaussian peak, and c_3 is the width of the Gaussian peak (standard deviation). The $\mathcal{N}$ indicates a normal distribution for the given center and width. The period ratio is denoted by r, and r_0 is the nominal period ratio of the mean-motion resonance. The limits on the period ratio range, r_{min} and r_{max}, are taken to be 2.94 and 3.06 for the 3:1 resonance (3.00 ± 0.06) and 1.62 and $1.71\bar{3}$ for the 5:3 resonance ($^5/_3 \pm {}^7/_{150}$).

3.2.4 Fitting

To fit for these parameters to our simulated period ratio distribution, we implemented a Markov chain Monte Carlo (MCMC) sampler using the `emcee` package [Foreman-Mackey et al., 2013]. We treat each period ratio in our sample as a Poisson process, calculating their probabilities as individual independent events, which requires no binning of the data. Given that we expect to find a well-defined peak for this set of systems, the priors are uninformative, using a flat log prior for the peak height and width and a prior for the slope that is flat in the angle of the line with the axis, to avoid biasing the slope fit towards higher slopes.

We initialized the MCMC analysis with 32 walkers based on an initial least squares fit to the data. The chains were considered converged when the number of steps was more than 100 times the maximum autocorrelation time calculated using `emcee` and the autocorrelation time changed less than one percent over 100 steps (<10,000 steps in total). We used a burn-in of twice the maximum autocorrelation time and thinned the sample by half the minimum autocorrelation time.

After fitting for the full set of systems, we then use the resulting posterior of the peak

width as a prior for the remaining fittings, including fits to the observations. As some of these fits do not have well-defined peaks, keeping this strict prior allows us to compare whether similar peaks are present in other sets of systems. Without this prior, for a set of systems with no peak, the peak height and width are highly correlated and the peak width is unconstrained. Additionally, this narrow width is a signature of the peak that we are interested in, and using this strict prior ensures we are investigating the peak arising from the time-averaging effect and not, for example, from stability-enhanced MMR protection.

We fit for the Kepler data set around each commensurability to find values for the three parameters. The KOIs included in this data set are listed in Table 3.4. We take the KOIs from the NASA Exoplanet Archive[1] for all candidate and confirmed KOIs. Including candidate KOIs may mean some pairs are not genuine planets. Looking at planet pairs is an intrinsically multi-planet phenomena, which leads to some detection biases from masking of transits in the light curve [Zink et al., 2019]. For planets with periods <200 days, this is only a 5.5% efficiency loss, so we neglect this potential bias. Additionally, eccentricity affects the probability of transit [Burke, 2008]. However, these effects are offsetting, and any net effect would be to make it more likely for eccentric planets to be detected.

To quantify how many additional planets are present due to the time-averaged resonance peak, we find the fractional area of the Gaussian curve that is in excess from the background.

3.2.5 Sampling and Fitting Eccentricity Scales

Figure 3.2 shows the eccentricity distributions of the generated system sets. While there is a clear amount of stability sculpting in the eccentricity distributions, there are many highly-eccentric planet pairs that remain in our stable samples. In order to compare the Kepler distributions to various eccentricity distributions, we take sub-samples of our generated system sets that are consistent with a given eccentricity distribution. This sampling is done

1. https://exoplanetarchive.ipac.caltech.edu

by calculating a probability for each eccentricity using the desired eccentricity probability distribution function and then using those probabilities as weights for drawing planet pairs without replacement. The sub-sample size was fixed at the same number of planet pairs as in the Kepler samples, 30 for the 3:1 resonance and 73 for the 5:3 resonance to allow for the same amount of systematic error from the sample size. The sub-samples were checked against a sample of the same size generated from the desired distribution using a 2-sample Kolmogorov–Smirnov test and a 2-sample Anderson-Darling test and accepted only if both p-values were ≥ 0.1.

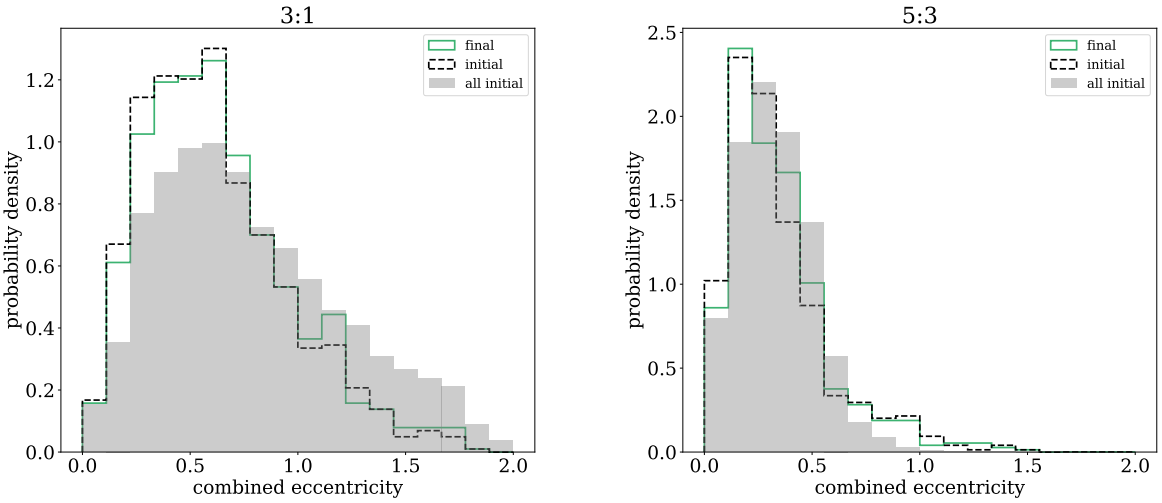

Figure 3.2: Distribution of the instantaneous eccentricities of the final selected planet pairs at the beginning (dashed black) and end (solid green) of the stability run. Their similarity shows they are in statistical steady-state. The gray background shows the initial combined eccentricity for all planet pairs, including those that went unstable and were excluded from the final selection. There is some stability sculpting, particularly at higher eccentricities, but many highly eccentric planet pairs remain. Distributions are shown for the (left) 3:1 and (right) 5:3 resonances.

The eccentricity distributions used are visualized in Figure 3.3. Given that we are considering planet pairs, the eccentricity distributions are those for combined eccentricities, $e_1 + e_2$. We considered the individual eccentricities to be independent.

The combined Rayleigh distributions were calculated analytically. The distribution of the

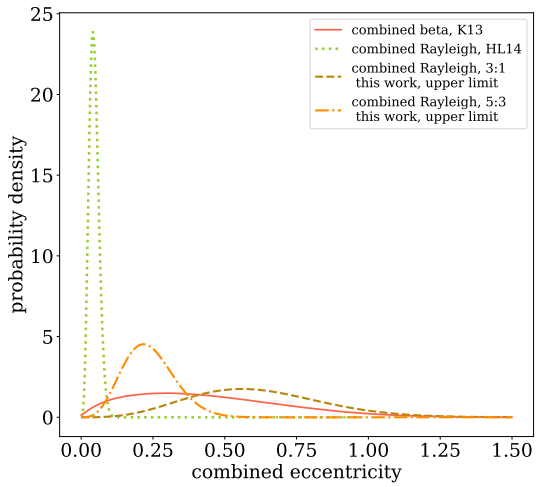

Figure 3.3: Several probability density functions with example parameters for the combined eccentricity of the planet pairs ($e_1 + e_2$). The combined beta distribution was derived numerically from samples taken in accordance with Kipping [2013] parameters and plotted using a Gaussian kernel-density estimate. Combined Rayleigh distributions for various scales were calculated analytically from Equation 3.3 and plotted for several samples scales: the best-fit value from Hadden and Lithwick [2014], $\sigma = 0.018$; the upper limit for 3:1 from this work, $\sigma = 0.245$; and the upper limit for 5:3 from this work, $\sigma = 0.095$.

sum of two independent variables is expressed by the convolution of the two distributions, $P(x_1 + x_2) = P(x_1) * P(x_2)$. Thus, the sum of two independent Rayleigh random variables with the same scale parameter σ has a probability density function of the form

$$P(x, \sigma) = \frac{e^{-x^2/2\sigma^2}}{4\sigma^3}\left(2\sigma x - e^{x^2/4\sigma^2}\sqrt{\pi}(2\sigma^2 - x^2)\mathrm{erf}(\frac{x}{2\sigma})\right). \tag{3.3}$$

The combined beta distribution was calculated numerically, incorporating the uncertainties in the distribution parameters from Kipping [2013]. A set of 10^6 eccentricities were drawn, each time with parameters drawn from a normal distribution with the mean and sigma given by the error bars from Kipping [2013], $\alpha = 0.867 \pm 0.044$ and $\beta = 3.03 \pm 0.17$ (this is slightly modified from $\beta = 3.03^{+0.17}_{-0.16}$ as listed by Kipping [2013] for ease of computation, with negligible effects). The probability density function was then calculated using a Gaussian kernel-density estimate.

We repeated this ten times, using a new random sub-sample, for each eccentricity distribution and combined the resulting chains to get the final posterior for a given eccentricity distribution. For the beta distribution, we increased the number of calculations to fifty, but found negligible improvement in the fit and so only ten were used for the remaining sub-

samples. Finally, we used the MCMC analysis on the sub-samples of the generated systems and calculated the fitted fractional peak area at each resonance. The peak area was found by calculating the area due solely to the continuum distribution and subtracting that from one (the normalized area). The results of this fitting and comparison with the Kepler data are discussed next.

3.3 Results

Our first result is the detection and quantification of the presence of an excess in planet pairs near the 3:1 and 5:3 resonance in our simulated systems. The fitted parameters are shown in Table 3.1, with errors listed from the 68.2% interval, along with the derived parameter of peak area. The data and median models, along with a sample of posterior draws, are shown in Figure 3.4.

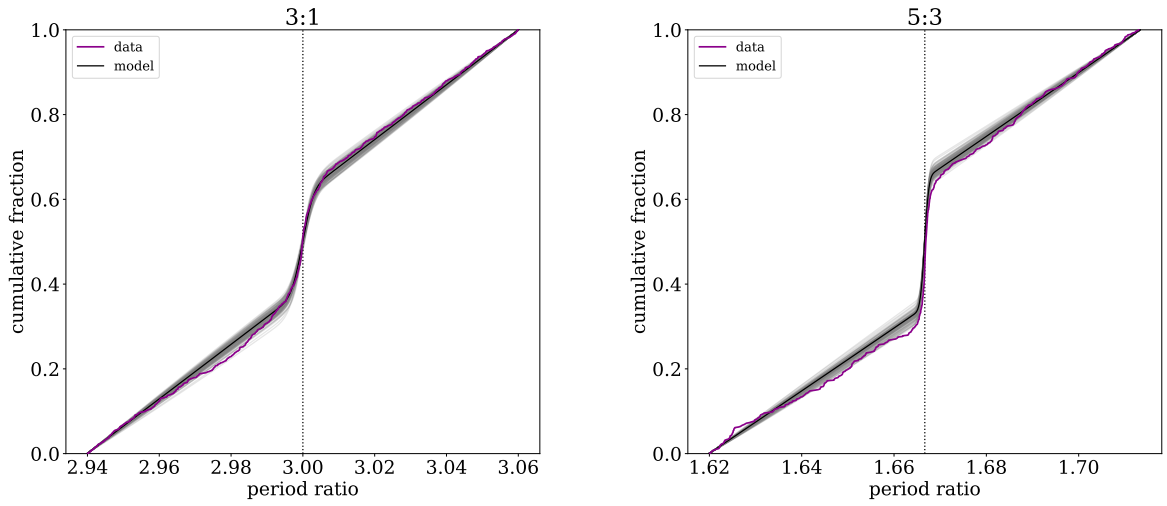

Figure 3.4: The cumulative distribution functions of the generated system set (magenta) along with the median model of the posteriors (black) and 100 sample draws from the MCMC posteriors (gray) for the (left) 3:1 and (right) 5:3 mean-motion resonances. The model is tightly fit to the data and shows a clear narrow peak at the resonance.

Next, we classify the presence of a peak near the 3:1 and 5:3 resonances in the Kepler

	c_1	c_2	c_3	A_{pk}
3:1				
Kepler	$0.1^{+1.0}_{-0.8}$	$-0.003^{+0.005}_{-0.002}$	0.0024 ± 0.0003	$-0.03^{+0.04}_{-0.02}$
Generated Sys (All)	0.1 ± 0.6	0.035 ± 0.004	0.0023 ± 0.0003*	0.23 ± 0.03
Generated Sys (beta)	$0.0^{+1.0}_{-0.9}$	$0.02^{+0.02}_{-0.01}$	0.0024 ± 0.0003	$0.16^{+0.11}_{-0.09}$
Generated Sys (Rayleigh, σ=0.07)	$-0.1^{+0.9}_{-1.0}$	$0.02^{+0.02}_{-0.01}$	0.0024 ± 0.0003	$0.11^{+0.12}_{-0.08}$
Generated Sys (Rayleigh, σ=0.245)	0.0 ± 1.0	0.03 ± 0.02	0.0024 ± 0.0003	0.2 ± 0.1
Generated Sys (Rayleigh, σ=0.34)	0.0 ± 0.9	$0.06^{+0.03}_{-0.02}$	0.0023 ± 0.0004	0.3 ± 0.1
Generated Sys (Rayleigh, σ=0.57)	$-0.1^{+0.9}_{1.0}$	$0.13^{+0.09}_{-0.05}$	0.0024 ± 0.0003	0.5 ± 0.1
Generated Sys (Rayleigh, σ=0.70)	0.0 ± 0.9	$0.17^{+0.12}_{-0.07}$	0.0023 ± 0.0003	0.6 ± 0.1
5:3				
Kepler	$0.2^{+1.1}_{-0.8}$	$0.004^{+0.004}_{-0.003}$	$(72 \pm 6) \times 10^{-5}$	0.04 ± 0.03
Generated Sys (All)	$0.4^{+1.0}_{-0.7}$	0.041 ± 0.004	$(72 \pm 6) \times 10^{-5}$*	0.31 ± 0.03
Generated Sys (beta)	$0.1^{+1.0}_{-0.9}$	$0.04^{+0.02}_{-0.01}$	$(73 \pm 6) \times 10^{-5}$	0.32 ± 0.08
Generated Sys (Rayleigh, σ=0.06)	$-0.1^{+0.8}_{-1.0}$	$0.012^{+0.007}_{-0.005}$	$(72 \pm 6) \times 10^{-5}$	$0.11^{+0.05}_{-0.04}$
Generated Sys (Rayleigh, σ=0.095)	0.1 ± 0.9	$0.024^{+0.012}_{-0.008}$	$(73 \pm 6) \times 10^{-5}$	$0.21^{+0.07}_{-0.06}$
Generated Sys (Rayleigh, σ=0.125)	$0.3^{+1.5}_{-0.8}$	$0.033^{+0.01}_{-0.009}$	$(73 \pm 6) \times 10^{-5}$	0.26 ± 0.06
Generated Sys (Rayleigh, σ=0.16)	$0.2^{+1.3}_{-0.9}$	$0.06^{+0.02}_{-0.01}$	$(73 \pm 6) \times 10^{-5}$	$0.38^{+0.07}_{-0.06}$
Generated Sys (Rayleigh, σ=0.205)	$0.2^{+1.1}_{-0.9}$	$0.09^{+0.03}_{-0.02}$	$(75 \pm 6) \times 10^{-5}$	0.48 ± 0.08

Table 3.1: Summary of the fitted parameters from our MCMC posteriors. c_1 is the slope of the linear background distribution, c_2 is the amplitude of the Gaussian peak, and c_3 is the width of the Gaussian peak (standard deviation). The prior on c_3 used on the all generated systems set (*) was different from the other fittings; see text for details. The fractional peak area, A_{pk}, is derived from the fitted parameters to quantify the additional excess or lack at the resonance location. We include here only the Rayleigh distribution results corresponding with 1-, 2-, 3-, 4-, and 5-σ discrepancy with Kepler.

data. The 3:1 for Kepler has no indication of a peak, and in fact the median model is a slight dip at the resonance location; however, the model fit is consistent with a flat background and zero peak. The 5:3 for Kepler has a small peak at the resonance location. The fitted parameters are shown in Table 3.1, with errors listed from the 68.2% interval, along with the derived parameter of peak area. The data and median models are shown in Figure 3.5. While the models are not as closely fit to the data as with the generated systems, this can be attributed to the much smaller sample size. For illustration, we drew ten samples with size equal to that of the Kepler data from the median model for each resonance, also shown in Figure 3.5. For both resonances, the Kepler distributions fall within the range of these samples.

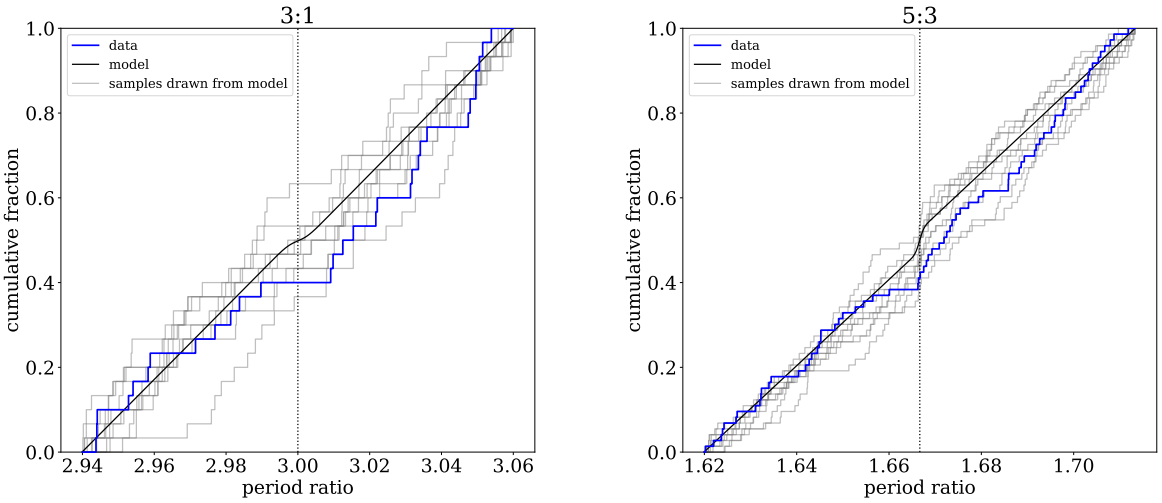

Figure 3.5: The cumulative distribution functions of the Kepler data (blue) along with the median model of the posteriors (black) and ten samples with size equal to that of the Kepler data drawn from the median model (gray) for the (left) 3:1 and (right) 5:3 mean-motion resonances. The difference in the data and model can be explained by the small sample size of the Kepler data.

We use our sub-sampling as described in Section 3.2 to generate a posterior for the peak area of a set of planet pairs with eccentricity consistent with a beta distribution as described in Kipping [2013]. These posteriors, along with the posteriors of the peak area for the Kepler

samples, are shown in Figure 3.6. The Kepler samples are not consistent with the beta distribution to a level of 1.8σ (92.0% confidence) for the 3:1 and 3.2σ (99.9% confidence) for the 5:3. The fitted parameters for the beta distribution sub-samples are shown in Table 3.1, with errors listed from the 68.2% interval, along with the derived parameter of peak area.

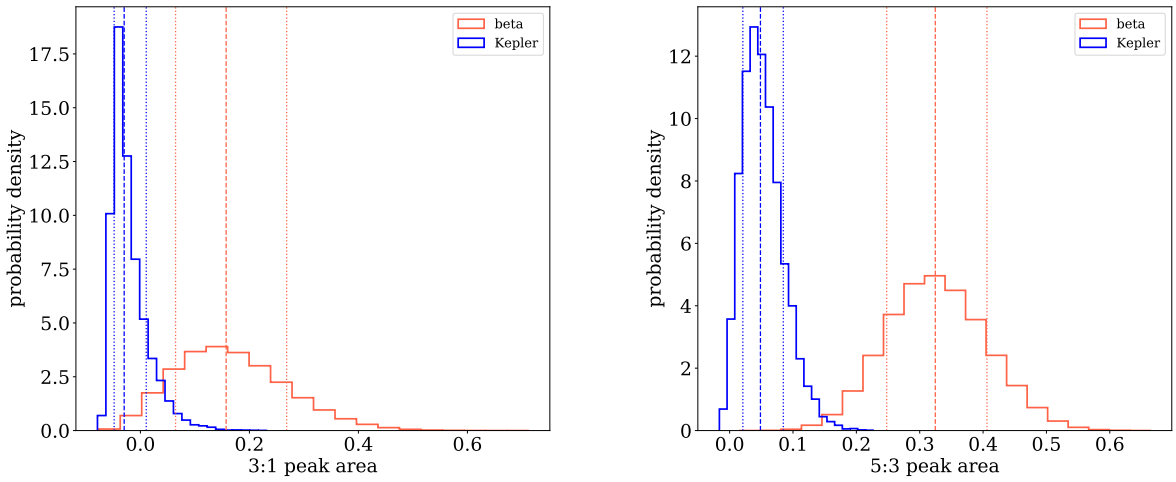

Figure 3.6: Comparison of the posteriors of the fractional peak area of the (left) 3:1 and (right) 5:3 mean-motion resonances. The Kepler sample is in blue and the simulated combined beta distribution from Kipping [2013] sample in red. The median values are shown with a dashed line and the 68.2% percentile intervals with dotted lines. The Kepler sample is not consistent with the beta distribution, which was derived from radial velocity planets.

We do a similar comparison for sub-samples of sets of planet pairs with eccentricity consistent with a Rayleigh distribution of various scales, from $\sigma = 0.005$ to 1.000 in steps of 0.005. Some scales were poorly sampled by our generated systems and were not analyzed or included in the results. Figure 3.7 shows the results for two of the eccentricity scales for each resonance, including the cumulative distribution for each of the ten random sub-samples as well as the model resulting from the median of the combined MCMC posteriors. At low eccentricities, the distribution has very little peak, as expected. This shows up as almost entirely continuum in our model, which describes the distribution well. At the higher eccentricity, the peak starts to become clear. Our model captures this changing behavior of

the distribution, allowing us to quantify the fractional peak area for comparison with the model fitted from the Kepler data.

The combined results for all the fitted scales are summarized in Figure 3.8, using a representation of the posteriors of the peak area (error bars are the 68.2% interval) at various scales and the Kepler data for comparison.

We find that, at 95% confidence, the upper limit for the Rayleigh scale consistent with the Kepler data is 0.245 for the 3:1 and 0.095 for the 5:3 resonance. The fitted parameters for a select number of the Rayleigh distribution sub-samples are shown in Table 3.1, with errors listed from the 68.2% interval, along with the derived parameter of peak area. These selected scales are 1-, 2-, 3-, 4-, and 5-σ discrepant with Kepler, and are also shown in Figure 3.8 as dotted vertical lines.

3.4 Analytics

To better understand the physical underpinnings of our results from numerical simulations, we investigate an analytical approximation for the effects of a second-order mean-motion resonance on the observed period ratio distribution. We use the framework of the integrable model developed by Hadden [2019], hereafter H19. This model is applicable for MMRs of any order interior to 2:1, and so we focus our application here on the 5:3 resonance. While this analytical model is not suitable for the 3:1 resonance, we expect the actual dynamics to be similar, as seen as well in our simulations.

There are two relevant pieces of information that we obtain from the model: the resonance width (in period ratio space) and the libration timescale. We use the integrable one-degree-of-freedom Hamiltonian $\mathcal{H}(J, \theta; J^*)$ as given by Equation 19 of H19; see that paper for full details on the derivation and application.

In brief, we first calculate the conserved quantity J^* for a given system (from H19 Equations 9, 20, and the relation $J^* = J - kP$) and then find the unstable fixed point at $\theta = 0$

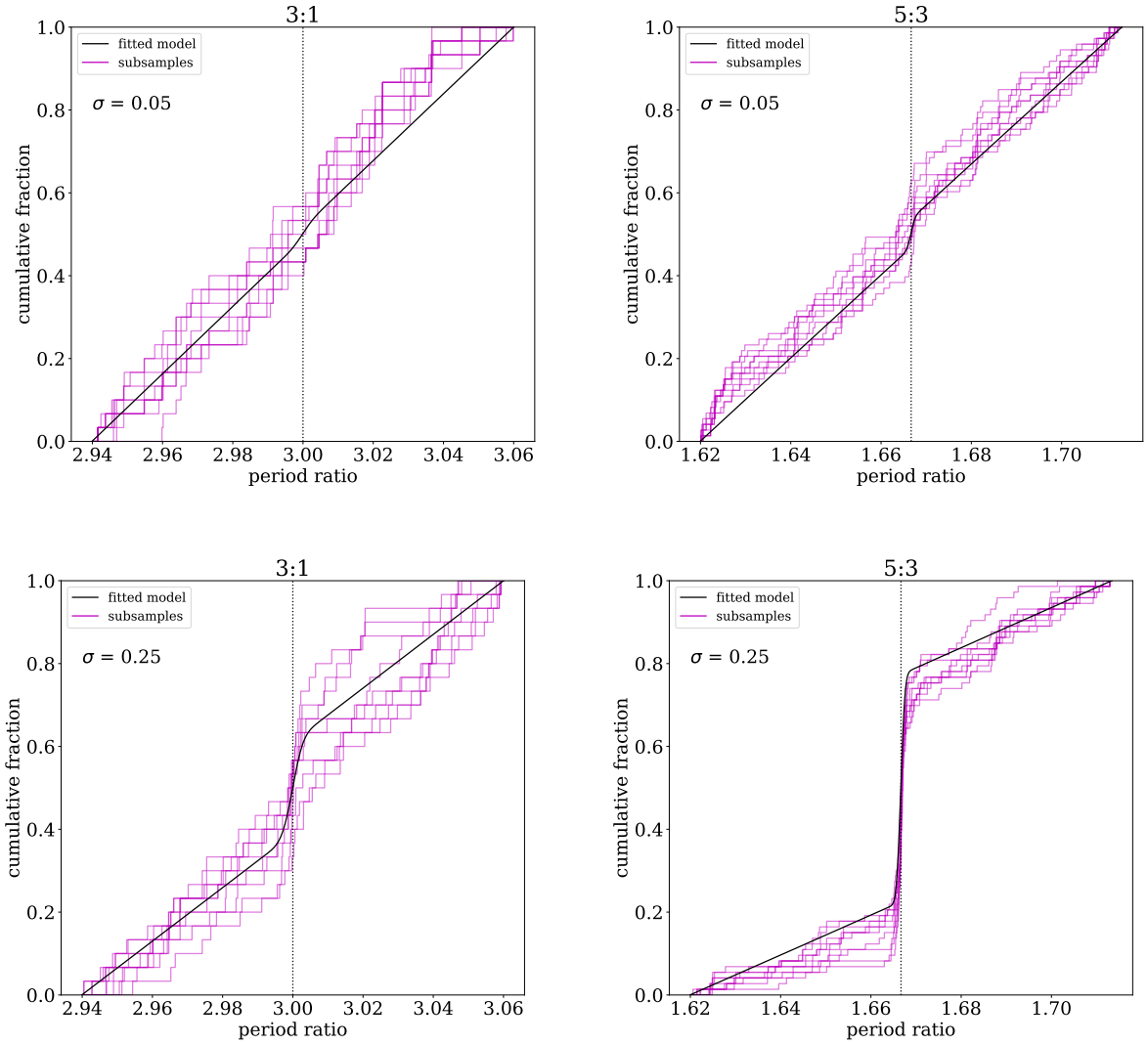

Figure 3.7: The sub-samples (magenta) and corresponding median model (black) for two Rayleigh example eccentricity scales. The low-eccentricity $\sigma = 0.05$ for the (top left) 3:1 and (top right) 5:3 resonances and the moderate-eccentricity $\sigma = 0.25$ for the (bottom left) 3:1 and (bottom right) 5:3 resonances. At low eccentricities, the distribution shows very little peak, while the peak appears more clearly as the eccentricity increases. Our model captures the behavior of the peak at various eccentricity scales.

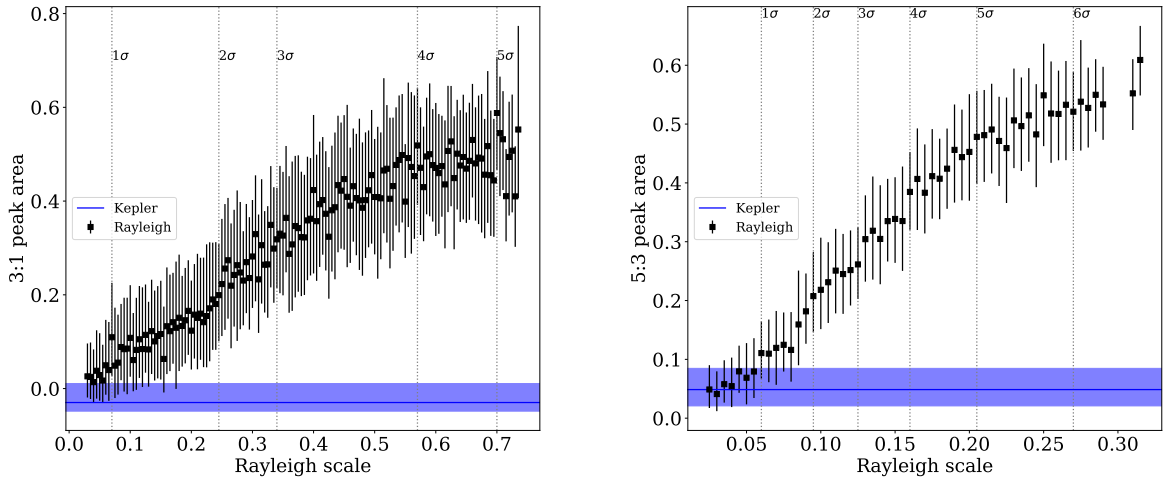

Figure 3.8: Comparison of the estimated fractional peak area of the (left) 3:1 and (right) 5:3 mean-motion resonances for a variety of eccentricity scales. The Kepler sample is in blue and the simulated combined Rayleigh distribution samples in black. The median values are plotted with the 1-sigma values as error bars. The Kepler sample is not consistent with the higher-eccentricity distributions, but consistent with all those below a certain level, allowing for an upper limit constraint on the Kepler samples' eccentricity distributions.

by finding the value of the conjugate momentum J that maximizes $\mathcal{H}$ and therefore determines the energy of the separatrix (E_{sep}). The maximum width is calculated by solving $\mathcal{H}(J, \pi/2; J^*) = E_{sep}$ for J. The two J values can be converted back to orbital elements using provided relations (H19 Equation 21), giving a minimum and maximum period ratio for the resonance. To find the period of libration, we use an approximation that linearizes the equations of motion in the vicinity of the equilibrium, using the Andoyer module of `celmech`. This approximation is only accurate for small-amplitude librations, and a more detailed analytical model would develop this further.

To investigate the period ratio distribution, we use a simple model with the resonance width and the period of libration. First, we calculate the resonance width for a given system configuration of masses, periods, and eccentricities.

If the period ratio of a planet pair is within the resonance width, the libration over time is represented by a sinusoid with the calculated libration period, initial phase as given by $k\theta_0$ (see H19 for details), and centered at $5/3$. The amplitude of the sinusoid is drawn randomly from a linear probability distribution between minimum at zero amplitude and maximum at an amplitude of half the resonance width. For period ratios outside the resonance width, the period ratio is assumed to be constant. This is a simplification, as the period ratios would likely change over time, but they would not follow the resonant model and so these changes are negligible to our result.

Finally, we take a time period to average over and "observe" the period ratio based on our libration model over that period n times where $n = \text{int}(t_{avg}/P_2)$.

We use this analytical model in two complementary ways. First, we apply the model to a Kepler-like population of planet pairs for comparison with our N-body results. Second, we apply the model to a single fiducial planet pair and investigate the effect of changing individual parameters of the system.

The systems for the analytical population model are generated according to the same

process as described in Section 3.2.1. These pairs are uniform in their initial period ratio between $5/3 \pm 7/150$, and each planet's eccentricity is randomly assigned using a Rayleigh distribution. We use three scales, a low-eccentricity $\sigma = 0.05$, medium-eccentricity $\sigma = 0.15$, and high-eccentricity $\sigma = 0.50$.

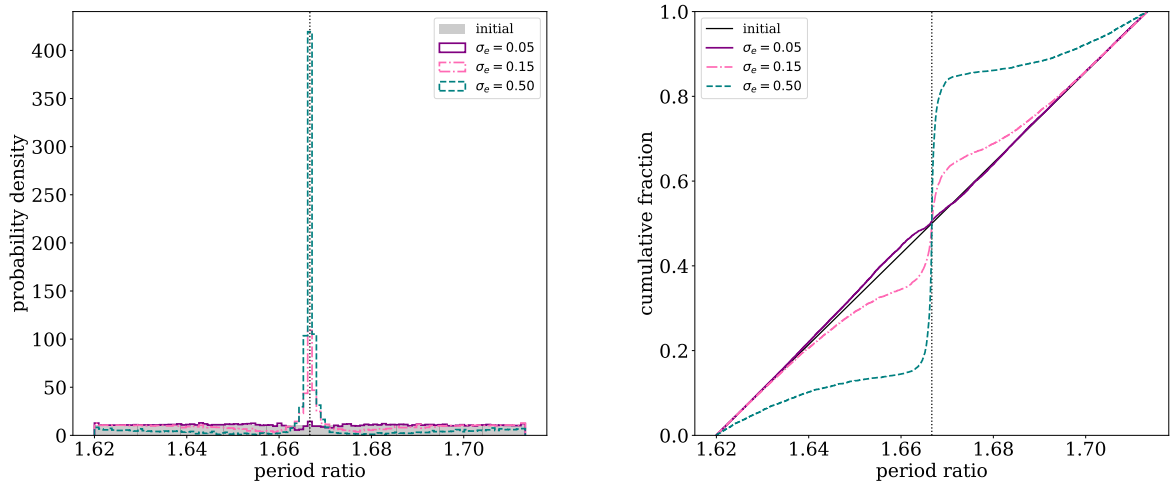

Figure 3.9: The analytically-predicted (left) probability density and (right) cumulative distribution of time-averaged period ratios near the 5:3 mean-motion resonance for three populations of Kepler-like planet pairs. Each population has a different Rayleigh scale for the planets' individual eccentricities. The nominal resonance value is marked with a dotted line. As seen in the simulated data, there is a strong, very narrow peak associated with increased eccentricity.

Figure 3.9 shows the resulting probability distributions and cumulative distribution functions for the three populations. As expected, a very narrow peak forms at the exact resonance location, the height of which increases with increased eccentricity. Because the initial period ratio is exactly uniform, the addition of planet pairs to this peak must result in a lower density of planet pairs outside the peak. These troughs are seen in the distributions. However, because the resonant and eccentric pairs end up at a very narrow location but can start from a wide range of initial period ratios that varies based on the properties of each system, the troughs are very spread out compared to the peak.

Parameter	Fiducial Value	Variable Range
$M_\star$ ($M_\odot$)	1	0.2 - 2
m_1 ($M_\oplus$)	10	0.5 - 20
m_2 ($M_\oplus$)	10	0.5 - 20
e_1	0.1	0 - 0.9
e_2	0.2	0 - 0.9
ϖ_1	0	$-\pi$ - π
ϖ_2	0.5	$-\pi$ - π
P_1 (d)	10	1 - 100
t_{avg} (yr)	3.5	0.5 - 10

Table 3.2: Variable parameters used for analytical investigation. When varied, each parameter is varied between the minimum and maximum values in 20 linear steps. P_2 is determined for each system based on the period ratio.

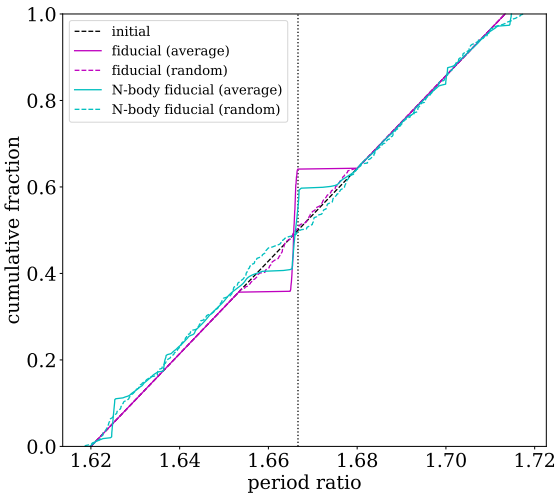

Figure 3.10: The analytically-predicted cumulative distribution function in period ratio for the fiducial system. The time-averaged period ratio is shown in solid magenta and a random period ratio from within the time period is shown in dashed magenta. The same distributions are shown for a comparable N-body simulation in cyan (solid is averaged and dashed is random). The black dashed line shows the initial flat period ratio distribution. The resonance location at $^5/_3$ is indicated with a vertical dotted line. There is reasonable agreement between the numerical and analytical distributions, and in both cases, the peak at resonance only appears when the period ratios are averaged.

To examine the effect of various parameters on the period ratio distribution, we establish a fiducial system and then vary parameters one at a time. The fiducial system properties are given in Table 3.2. The properties were chosen to be consistent with Kepler-like systems but without any special consideration. Then we investigate the period ratio libration for a grid of 500 period ratios (by changing the period of the outer planet) between our limits of interest, $5/3 \pm 7/150$. The resulting cumulative distribution function in period ratio is shown in Figure 3.10, both for the average period ratio and a period ratio chosen randomly within the time period. As expected, a very clear and narrow peak forms when the period ratios are averaged over time. We also ran an N-body simulation with the same parameters for comparison. While the distributions are not exact, the agreement is good for this simplified model. It is also interesting to note in the N-body distribution what seem to be similar (though much weaker) signals at the 13:8, 18:11, and 17:10 resonances.

In this analytical model, we do not include a continuum such as is present in our model in Equation 3.2. Instead, this analytical model examines only how the peak super-imposed on the continuum is affected by the changing system parameters. This, and the fact that all of the systems in this analytical model have the same properties aside from the period ratio, is the difference in the shape of the cumulative distribution functions in Figures 3.4 and 3.10. The height and width of the peak is our interest, and thus what we investigate via this analytical model.

The results of varying the nine parameters are shown in Figure 3.11. Only the averaged period ratios are shown here for clarity, with the color indicating the parameter's value as indicated by the color bar to the right of each plot. For each parameter, the fiducial value is plotted as a white dot on the color bar for reference.

First we see that varying the masses of the planets (3.11a and 3.11b) has a noticeable but small effect. The effect does not depend on which planet's mass changes, as the resonance is sensitive to the planets' combined mass. The amplitude of the peak does not change much,

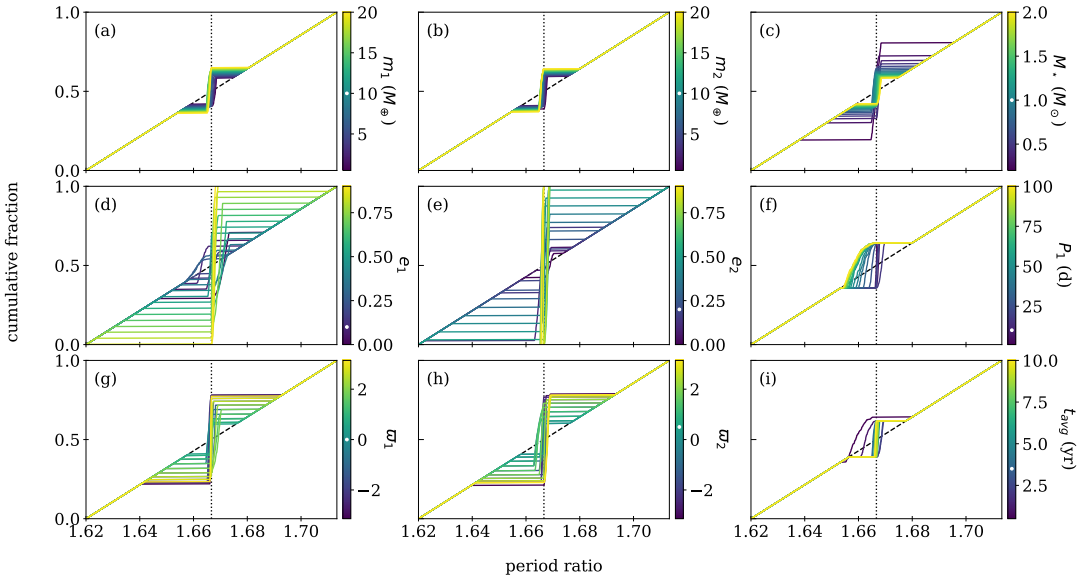

Figure 3.11: The analytically-predicted, time-averaged cumulative distribution functions in period ratio for various systems. The parameter being varied is indicated by the color bar to the right of each plot, where the fiducial value is plotted in white for reference. The resonance location at $5/3$ is indicated with a vertical dotted line. All the parameters affect the height and width of the peak, the most notable being the eccentricity of either planet, shown in panels (d) and (e).

but the width does change slightly and the center of the peak shifts. This is due to a change in the libration period—if the libration period increases past t_{avg}, the averaged value will no longer lie at the center as a cycle has not completed. Changing the mass of the star (3.11c) has a generally similar effect, though there is a stronger effect when reaching much larger mass ratios (i.e., a smaller stellar mass).

As expected, we see a very strong dependence of the peak on eccentricity (3.11d and 3.11e). As eccentricity is increased, the amplitude of the peak at resonance becomes much larger. In this case, the effect is notably stronger when e_2 is increased. The orientation of the eccentricities (3.11g and 3.11h) also has an effect, although less than from the magnitude. In our fiducial system, the eccentricities are 0.5 rad ($\sim 30^\circ$) out of alignment. As either of the ϖ changes towards $\pm\pi$ we see an increase in the amplitude of the peak, suggesting a stronger signal for anti-aligned eccentric planet pairs.

Changing P_1 (3.11f) has no apparent effect on the amplitude or width of the peak, as is expected. However, the location of the center of the peak changes significantly. This is because the libration period depends on the planets' periods, and so for longer period planet pairs, the libration cycle has not yet completed during this t_{avg}. We can similarly see this effect from changing t_{avg} (3.11i). As t_{avg} decreases, fewer of the systems have completed their libration and so the center shifts away from the resonant location. In this case, the center of the peak shifts leftward for incomplete libration cycles. This depends on the initial phase of the libration. For different initial phases, the peak can also shift rightward, and so the direction of the peak shift should not be seen as significant.

We note a few remarks about these analytical results. First, we use a very simplified model for the libration. Several N-body comparisons were done to ensure this model was reasonable to use as an approximation, but it does not give exact behavior. Second, we use the simplified Hamiltonian from H19 that is based on a leading-order approximation in eccentricity. This introduces additional inaccuracies, especially for our high-eccentricity

systems. Third, there are no stability cuts or considerations, and it is probable that not all of these systems are viable. Fourth, this analytical model assumes a planar configuration and no inclination effects.

Given these points, we do not provide this analytical investigation for a quantitative comparison. However, we expect the qualitative trends to be accurate and find the overall behavior to be in line with our expectations, confirming the resonant behavior as seen in our numerically simulated results.

3.5 Discussion

It is particularly striking how narrow the resonance peak is. This arises from the time-averaging of the orbital parameters and is a clear feature of the second-order resonance. The narrowness of the peak is, for example, what allows us to ignore the effects of any associated troughs in our analysis.

Our sets of generated systems are intended to create sets of planet pairs with a large array of eccentricities limited only by stability. We are agnostic to formation mechanisms, i.e., whether such systems are physically realistic. This allows us to marginalize over other properties to isolate the effects of eccentricity on the period ratio distribution. Other potential effects are discussed below.

3.5.1 Comparison with Previous Results

The first results pertaining to the eccentricity of exoplanet populations were obtained via radial velocity measurements. These systems were typically composed of giant planets and generally excited in eccentricity. Wright et al. [2009] found a mean eccentricity of 0.22 for multi-planet systems, their data containing many more giant systems than in the Kepler observations. Similarly, Kipping [2013] quantifies the eccentricity distribution of radial velocity planets with a beta distribution that gives a mean eccentricity of $\sim$0.22.

As more transiting planet data became available via Kepler, and different techniques were developed for constraining the eccentricity of these planets, a different picture began to emerge. Fabrycky et al. [2014] measured $\sigma \lesssim 0.1$ for a Rayleigh distribution of the eccentricity of super-Earths. Studies done on subsets of the Kepler sample with well-characterized stellar properties found $\sigma = 0.049 \pm 0.013$ [Van Eylen and Albrecht, 2015], $\sigma = 0.03^{+0.02}_{-0.03}$ [Xie et al., 2016], $\sigma = 0.061^{+0.010}_{-0.012}$ [Van Eylen et al., 2019], and $\sigma \sim 0.04$ [Mills et al., 2019]. Hadden and Lithwick [2017] measured individual systems (their Figure 5) and quoted a typical scale of $\sigma = 0.018^{+0.005}_{-0.004}$ from their prior work [Hadden and Lithwick, 2014].

These results indicated much lower eccentricities are typical for small planets. Kane et al. [2012] found that for giant planets the Kepler observations were in agreement with previous radial velocity results, but that planets smaller than Neptune became "rapidly and significantly more circular."

Our constraints on the planets near the 3:1 and 5:3 are consistent with the results obtained previously for small, multi-planet systems observed by Kepler. Our 5:3 constraint, which would predict a mean eccentricity of no more than 0.12 at 95% confidence (for a Rayleigh distribution, $\langle E \rangle = \sigma\sqrt{\pi/2}$), is not consistent with the eccentricities of giant planets such as those analyzed by Wright et al. [2009]. We find a 1.8σ (3:1) and 3.2σ (5:3) disagreement with the beta distribution of Kipping [2013] (see Figure 3.6).

He et al. [2020] find a strong multiplicity dependence for the eccentricity distribution, with the median eccentricity decreasing as n increases. This multiplicity dependence has also been found by Bach-Møller and Jørgensen [2021]. Additional evidence for a difference between single-planet and multi-planet eccentricities was found in Xie et al. [2016], Mills et al. [2019], and Van Eylen et al. [2019]. This dichotomy may be due to unobserved outer companions [Poon and Nelson, 2020]. As our method depends on measuring a period ratio, which must have two planets, we probe the observed $n \geq 2$ Kepler sample.

He et al. [2019] and He et al. [2020] use forward modeling to constrain properties of

the intrinsic population of Kepler planets. While in this work we are constraining the eccentricities of the observed population, rather than the intrinsic population, we find the comparison of interest. He et al. [2019] find low eccentricities, with characteristic Rayleigh scales $\sigma \simeq 0.01 - 0.02$. He et al. [2020] uses an angular momentum deficit approach for the modeling and finds a median eccentricity of 0.138 for two-planet systems, decreasing down 0.029 for five-planet systems and to 0.009 for ten-planet systems (see their Table 5). These results are consistent with ours, despite the differing populations being described.

Interestingly, He et al. [2020] find that a log-normal distribution is a better fit for the eccentricity distribution, rather than a Rayleigh distribution which is more typically assumed (e.g. He et al. 2019, Fabrycky et al. 2014). Tremaine [2015] and Shabram et al. [2016] also recommended a non-Rayleigh distribution, while Van Eylen et al. [2019] consider several models and do not advocate one over another. We leave the investigation of additional eccentricity distributions to future work.

Our results, then, are consistent with other studies and further evidence that the eccentricity distribution of small (i.e. not-giant) planets in multi-planet systems have a different underlying eccentricity distribution than single-planet or giant-planet systems.

3.5.2 Tides

Tides might act to remove some of the planet pairs from resonance or decrease their eccentricity over time [Novak et al., 2003, Delisle et al., 2014]. Here we consider the impact of tides on these relatively close-in planets.

We calculate the circularization timescale for our planet pairs using Equation 9 of Rasio et al. [1996]. The resulting timescales, scaled by Q, are shown in Figure 3.12. For terrestrial planets, typical Q values range from 10 to 500 [Goldreich and Soter, 1966]. We would thus expect approximately half of our sample would have undergone one tidal circularization timescale in 100 Myr.

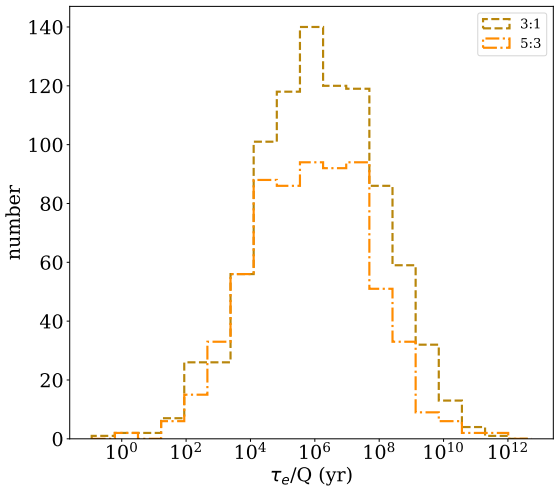

Figure 3.12: The circularization timescale of the inner planet of our generated populations, scaled by Q. Based on a typical Q value of ∼100 for terrestrial planets, we expect that perhaps half of our sample may have undergone one tidal circularization timescale in 100 Myr, indicating that maintaining these planets at such high eccentricities may be difficult.

However, this does not affect our results, which are focused solely on the effect of eccentricity in shaping the period ratio distribution and not in the feasibility of such an eccentricity distribution. This tidal timescale is a consideration for other limits on the stable eccentricity of a similar population.

Furthermore, we can split our sample sets into two equal parts based on the scaled circularization timescale to see if systems with faster circularization timescales have different properties in this context that might be affecting our results. Instead, we find that the resulting averaged period ratio and eccentricity distributions are not statistically different. The p-values from a 2-sample Kolmogorov–Smirnov test for the split samples of the 3:1 set are 0.70 for the averaged period ratio distribution and 0.17 for the averaged combined eccentricity distribution. For the 5:3 set, the corresponding p-values are 0.13 and 0.34, respectively. Thus, we expect tides to be an interesting but negligible consideration for our results.

3.5.3 Eccentricity at Formation

In our approach to creating our sets of planet pairs, we did not use a physical motivation for the eccentricities of the planets. Indeed, we purposely attempted to cover a large eccentricity space to allow for sub-sampling by eccentricity. We did, however, use a stability analysis to cut unstable planet pairs from our sample (see Section 3.2.1). This stability cut produced some shaping of the eccentricity distribution (i.e. Figure 3.2), in particular preferentially removing high-eccentricity pairs.

The stability-shaped eccentricity distribution is still much too eccentric to match the Kepler data, however. Because stability alone cannot explain the low observed eccentricities, this implies some other process must prevent high-eccentricity pairs, likely related to formation mechanisms.

The eccentricity distribution predicted by formation models varies depending on many parameters, particularly related to the properties of the protoplanetary disk [Fortier et al., 2013]. Effects that serve to excite eccentricity include reduced solid surface density [Van Eylen et al., 2019], shallower solid surface density profiles [Moriarty and Ballard, 2016], the presence of additional companions [Huang et al., 2017, Anderson and Lai, 2017], and others. Conversely, there are effects that can dampen eccentricity, such as the presence of planetesimals to provide dynamical friction during formation or gas in the disk [Mulders et al., 2019]. Recent findings by Yee et al. [2021] indicate that the observed eccentricities (of those measured by Hadden and Lithwick [2017]) are lower than predicted stability limits or from giant impact formation theory. Fitting the exact formation conditions consistent with the Kepler planets is the beyond the scope of this chapter.

3.5.4 Mass Dependence

Mass and eccentricity both have strong effects on the behavior of planets in mean-motion resonance. This can be seen, for example, in Figure 3.11. By using a distribution of masses

and mass ratios in our set of simulated planet pairs that approximates that seen in the Kepler data, we intend to marginalize over the mass effect to isolate the effect from eccentricity. To illustrate how the mass and eccentricity effects interact, we split our set of planet pairs into 2 groups in mass ratio and 2 groups in eccentricity. The split was chosen at the median values in each case; $e_1 + e_2 = 0.58$ and $\log\frac{m_1+m_2}{M_\star} = -4.42$ for the 3:1, $e_1 + e_2 = 0.28$ and $\log\frac{m_1+m_2}{M_\star} = -4.44$ for the 5:3.

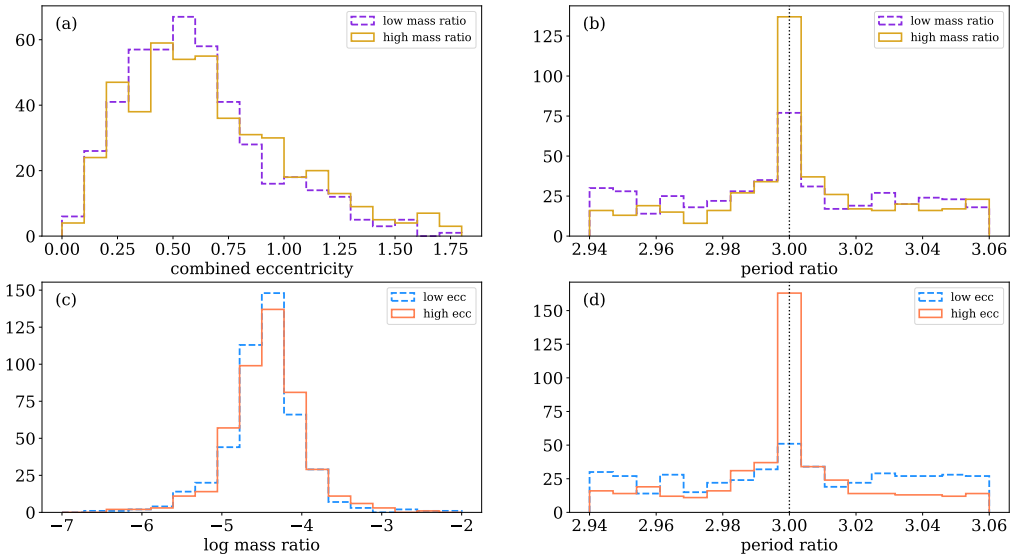

Figure 3.13: For our generated planet pairs near the 3:1 resonance, we split the population into two halves. First by the log of the mass ratio ($\log\frac{m_1+m_2}{M_\star}$), shown in the top panels as the combined eccentricity (a) and period ratio (b) distributions for these two halves of the population. In the bottom panels, we split the population into two halves by the combined eccentricity and show the log mass ratio (c) and period ratio (d) distributions for these two halves. While both mass and eccentricity affect the period ratio distribution, the time-averaged peak at resonance is still present even in the low-mass sample, but it disappears in the low-eccentricity sample, indicating the eccentricity is more strongly contributing to the effect.

Figures 3.13 and 3.14 show the distributions for these split sets of planet pairs. The eccentricity distribution is largely unaffected by the mass ratio cut (3.13a/3.14a), and the same is true for the mass ratio distribution and the eccentricity cut (3.13c/3.14c). However,

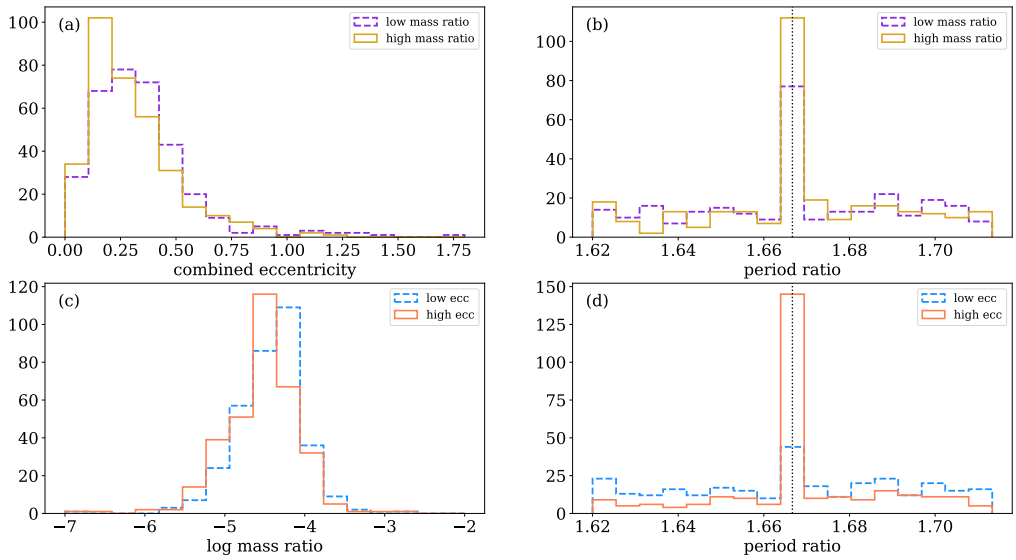

Figure 3.14: The same as Figure 3.13 but for the 5:3 resonance.

strong differences are seen in the distributions of the period ratios. When looking across all eccentricities, the higher mass ratio half of the simulated systems has a more notable peak at the exact commensurability location, but the peak is still clear for the lower mass ratio planet pairs (3.13b/3.14b). Conversely, when looking across all mass ratios, the higher eccentricity half of the data has almost the entirety of the effect at the commensurate period ratio, and the peak almost vanishes for the lower eccentricity half of the data (3.13d/3.14d).

Thus, while mass and eccentricity both have strong effects on the resonant behavior, the eccentricity effect is much stronger. Given this difference in strength and the marginalization over the apparent mass ratio distribution of Kepler planets, our results robustly isolate the eccentricity effect near the 3:1 and 5:3 resonances.

3.5.5 Resonance Probability

Using our fitted model for the Kepler period ratio distribution, we can calculate a resonance probability for a given period ratio by comparing the height of the full model at that period

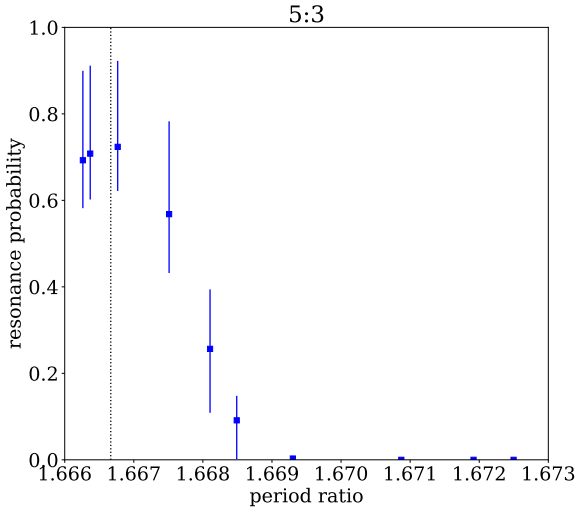

Figure 3.15: The probability of the Kepler planet pairs being part of an excess peak associated with 5:3 mean-motion resonance and not part of the background continuum of period ratios. All pairs with a non-zero median probability are plotted; see Table 3.3 for planet names and values.

ratio to the height the model predicts for the continuum at that period ratio.

When applied to the Kepler 3:1 sample, the resonance probability for all the planet pairs is zero. This is due to the fact that our fitted model predicts no peak at the resonance.

For the Kepler 5:3 sample, there are 10 KOI pairs with non-zero resonance probability. These are listed in Table 3.3 with their calculated resonant probability. The resonance probabilities are plotted in Figure 3.15. In Section 3.5.6 we investigate one of these KOI pairs, K02261, in more detail.

3.5.6 Investigating the Case of K02261 (Kepler-1164) via Timing Analysis

There are two KOIs in this system: K02261.01 and K02261.02. The former is confirmed (Kepler-1164 b, Morton et al. 2016); the latter is a candidate. The K02261 system is also known as Kepler-1164.

To investigate this system, we use the transit numbers, times, and variations from Rowe et al. [2015]. There are 315 transits of K02261.01 and 157 transits of K02261.02 covering a time period of approximately 1455 days. The pair's average period ratio over this time is 1.666(4).

KOIs		Kepler Names		Resonance Probability
K01574.01	K01574.02	Kepler-87 b	Kepler-87 c	$0.7^{+0.1}_{-0.2}$
K02261.01	K02261.02	Kepler-1164 b	-	$0.7^{+0.1}_{-0.2}$
K04034.01	K04034.02	Kepler-1543 b	-	$0.7^{+0.1}_{-0.2}$
K02163.01	K02163.02	Kepler-365 b	Kepler-365 c	$0.6^{+0.1}_{-0.2}$
K02086.01	K02086.03	Kepler-60 b	Kepler-60 d	0.3 ± 0.1
K04136.01	K04136.02	-	-	0.1 ± 0.1
K02169.01	K02169.02	Kepler-1130 A b	-	$0.003^{+0.007}_{-0.002}$
K02693.02	K02693.03	Kepler-398 c	Kepler-398 d	$10^{+121}_{-9} \times 10^{-8}$
K00582.01	K00582.03	Kepler-191 d	Kepler-191 b	$7^{+381}_{-7} \times 10^{-12}$
K01151.01	K01151.04	Kepler-271 b	-	$2^{+198}_{-2} \times 10^{-14}$

Table 3.3: KOIs near the 5:3 with non-zero resonance probability. The associated Kepler name is listed where applicable.

Transit data cannot give an instantaneous value of the osculating period ratio as measured exactly from an N-body simulation. Instead, we approximate the period ratio at any given point in time using the last two observed transits of each planet prior to that point. The average period for each planet is approximated as the difference in transit times divided by the difference in transit numbers, and these periods are used to calculate an approximate period ratio for that point in time.

The variation of period ratio over time for K02261 according to this method is shown in Figure 3.16. Errors are incorporated numerically by repeating the calculation 1000 times, drawing transit times randomly from a Gaussian described by the transit time and TTV uncertainty for each transit from Rowe et al. [2015]. We use 600 evenly spaced times from the observing period to calculate the period ratio.

Due to the scatter and uncertainty of the observational data, it is possible but not evident that the period ratio of the planet pair may be oscillating around the exact commensurability over time. This is the case even when binning the data or attempting to phase fold on various periods. We use N-body models of the planet pair to investigate further.

First, we need to have a defined set of system parameters in order to produce an N-body

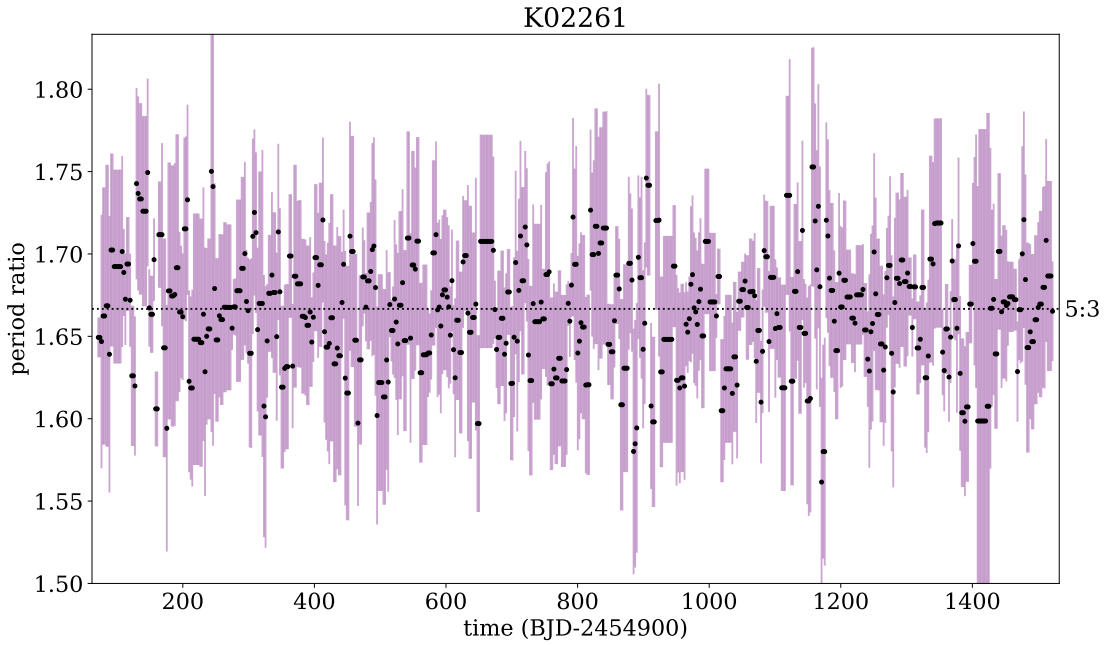

Figure 3.16: The period ratio over time for K02261 estimated from transit time data from Rowe et al. [2015]. Black points are calculated from the given transit times, and errors are the standard deviation of 1000 transit time realizations drawn using the uncertainty on the TTVs. The uncertainty from observations is too large to reveal any structure in the behavior of the period ratio over time.

model. Given the uncertainty of the data, we do not aim to constrain a fit but merely find sample systems that are consistent with the observational TTV data.

From the least squares optimization function in `SciPy` [Virtanen et al., 2020], we obtain a fit and covariance matrix using the observed transit times. We use these to generate 10^5 samples from a multivariate normal distribution, enforcing a requirement that the samples must be physical: that is, not allowing negative masses or eccentricities greater than 1. We use the analytical stability criterion from Hadden and Lithwick [2018] to ensure these samples are stable, with $Z < Z_{crit}$, where Z is the complex relative eccentricity (see their Equations 15 and 19).

From these stable, physical samples that are consistent with the observational data, we can select examples to illustrate the possible behavior of K02261. We select a subset of 10 random samples that show libration in the resonant arguments of the 5:3 resonance and a subset of 10 random samples that do not. From these two example models, we repeat the period ratio over time calculation that was done for the observed transit times in Rowe et al. [2015]. This model uses the same transit numbers as Rowe et al. [2015], and so any observational gaps in the data will be re-created and associated systematic uncertainty in this method of approximating the period ratio from transits is maintained. There is no uncertainty associated with the transit times themselves, however, being calculated exactly from the N-body simulation. For comparison, we also directly take the osculating period ratios from the N-body simulation at the same points in time.

From these twenty sample systems, we can compare the osculating period ratios estimated from the transit times and taken exactly from the simulation. We compare these two period ratio measurements in Figure 3.17 and find that the estimation from the transit times is highly correlated with the exact period ratios over time, with a Pearson correlation coefficient of 0.834 for the entire set of twenty. Looking at the same relation in the sample systems categorized as resonant, the Pearson correlation coefficient is 0.925, and for those categorized

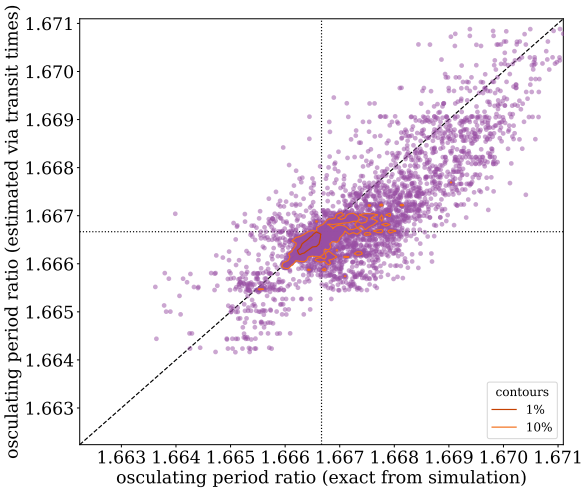

Figure 3.17: Comparison of the measured period ratio over time using exact osculating periods from an N-body simulation and the estimated osculating period ratio using the previous two transits at a given point in time to estimate the planet periods. The Pearson correlation coefficient is 0.834, indicating a highly linear correlation. Exact correlation is shown by the black line for reference. The comparison is done for twenty realizations of the K02261 that are consistent with the observed data, ten which show signs of libration in the resonant argument and ten that do not. Contours of the top 1% and 10% of the point density are shown to aid in interpreting the densest regions. The high correlation indicates that this estimation approach is a useful measurement of the period ratio changing over time directly from the transit times.

as non-resonant, the Pearson correlation coefficient is 0.777. These high correlations indicate that this estimation approach is a useful measurement of the period ratio changing over time, without requiring an assumption about the resonant state.

Next, we use these samples to examine how the period ratio changes over time. During the Kepler observation period, there is little structure to the period ratio change. This is likely due to the small expected masses of the planets, both of which are consistent with zero from our stable, physical samples resulting from the least squares fit. However, if we extend the time period another ten Kepler observation periods, structure begins to emerge, as shown in Figure 3.18. The period ratio varies periodically, although not always sinusoidally, and while there are many types of variation within these 20 samples, some difference between the resonant and non-resonant samples is visible. In particular, the mean of the period ratio over the entire time is shown with a horizontal line for each sample, and the resonant samples clearly cluster closer to the 5:3 commensurability while the non-resonant samples tend to vary around different period ratios.

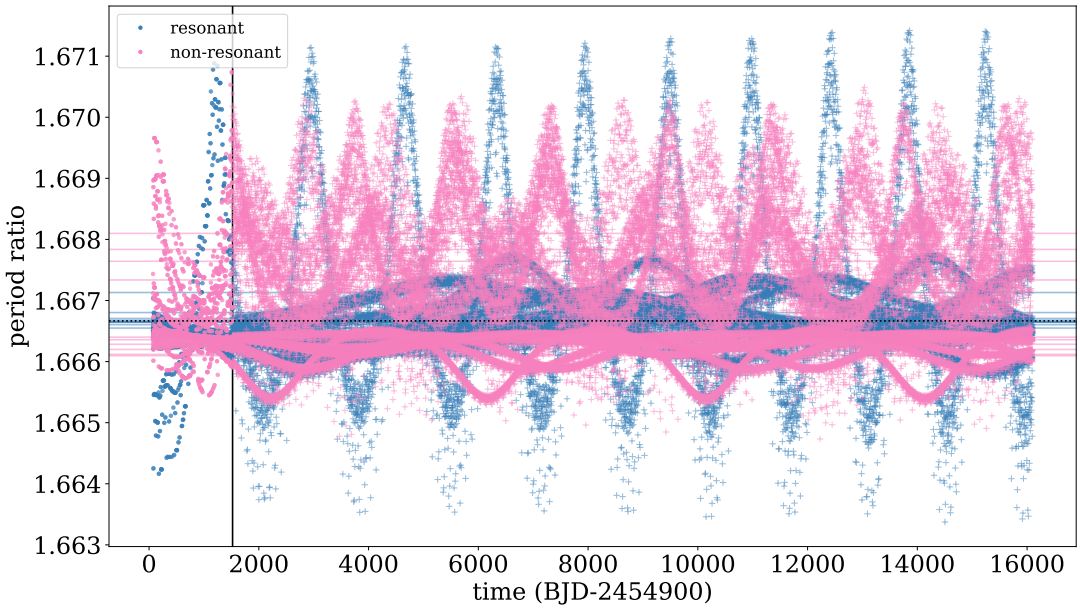

Figure 3.18: The period ratio over time for 20 sample systems of K02261 that are consistent with the observed TTVs. We use the libration or non-libration in the resonant arguments of the 5:3 resonance to categorize the samples as resonant or non-resonant and extrapolate beyond the Kepler observational period (the time before the solid vertical line) to visualize the periodic behavior in this system. The horizontal lines show the average period ratio over the entire time for each system. The behavior of each individual system varies, but the resonant systems cluster much closer to the exact resonance over time, as expected.

However, when we compare these models to the observational data, it is clear the errors from measuring the transit times dominate over any of these effects—contrast the range in the y-axis in Figures 3.16 and 3.18. From this, we infer that the observational data from Kepler for specific systems near the 5:3 resonance do not contradict our conclusions in this chapter, but that more precise transit times observations are needed to place any substantive constraints on these individual systems.

3.6 Conclusion

In this work, we demonstrated that highly-eccentric planets produce a very narrow peak near the second-order resonance locations of the 5:3 and 3:1 MMRs when averaged over sufficient time (i.e., longer than the typical libration period), primarily via numerical simulations but also supported by an analytical framework from Hadden [2019]. While we focused on second-order resonances in this work, as they are the widest and strongest resonances of this shape and therefore the likeliest to have a detectable signal, we note that this type of narrow, time-averaged peak shaping is expected to be present for higher-order resonances as well.

We fit a model to the 5:3 and 3:1 peaks in the Kepler period ratio distribution, finding a small peak at the 5:3 and no evidence of a peak at the 3:1.

The lack of these peaks in the planet pairs observed by Kepler therefore places an upper limit on the eccentricity distribution of these planets. We place that upper limit at $\sigma = 0.245$ (3:1) and $\sigma = 0.095$ (5:3) at 95% confidence for a Rayleigh distribution with scale σ for each planet.

Using our model of the 5:3 Kepler data, we can calculate a resonance probability for the planet pairs located near the resonance. For the K02261, a potentially resonant planet pair identified by this calculation, we investigate the observed transit times from Rowe et al. [2015] and conclude that it is possible to estimate the change in period ratio over time based on the transit times. However, in this case the observational errors in the TTVs are too large

to place any constraints on the individual system.

Given that not all of the highly eccentric planets in our numerical simulations are ruled out by stability, we infer that some other mechanism, likely from formation processes, drives the observed low eccentricities of the planet pairs observed by Kepler.

Our method is an independent approach to constraining the eccentricities of the population observed by Kepler, and we find results consistent with other methods: the small planets typical of Kepler observations tend to have low eccentricities, lower than those typically observed of giant planets.

3.7 Appendix

3.7.1 KOIs

The KOIs used in the analysis of the Kepler population in this chapter are listed in Table 3.4.

3.7.2 Population Comparisons

In this section, we illustrate various properties of the synthetic population of planet pairs that we generated as described in Section 3.2.1. When applicable, the corresponding properties of the Kepler sample are shown as well to highlight the general similarity in parameter coverage. Data for the Kepler sample, including errors, were taken from the NASA Exoplanet Archive for all candidate and confirmed KOIs on October 28, 2020. This similarity is important to ensure that we are marginalizing over other contributing factors to isolate the eccentricity effect on the period ratio distribution near second-order MMRs.

Figure 3.19 shows the cumulative distribution of the logarithm of the planet-to-star mass ratios for the generated planet pairs and Kepler planet pairs. The planet masses for the Kepler planets were forecast from their radii using the `Forecaster` package. Observational uncertainty and the probabilistic nature of the `Forecaster` mass-radius relation were incor-

Table 3.4: KOIs in the vicinity of the 3:1 and 5:3 resonances. KOI data were taken from the NASA Exoplanet Archive for all candidate and confirmed KOIs on October 28, 2020. Observational errors are not listed for the periods (and therefore period ratios) as they are generally of an order of one part per million and may not be representative of the accuracy of the listed periods (i.e. Lissauer et al. 2020).

3:1

KOIs		Period Ratio	Periods (d)	
K01929.01	K01929.02	2.944	9.693	3.293
K00490.03	K00490.04	2.944	7.406	21.804
K00834.03	K00834.04	2.944	6.156	2.091
K01364.01	K01364.02	2.953	20.834	7.056
K01301.01	K01301.02	2.954	12.699	37.514
K00152.02	K00152.04	2.958	27.402	81.064
K02199.01	K02199.02	2.959	9.033	3.053
K00566.03	K00566.02	2.971	42.069	14.157
K00245.01	K00245.03	2.977	39.792	13.367
K00497.01	K00497.02	2.981	13.193	4.425
K00582.01	K00582.02	2.984	5.945	17.738
K03029.01	K03029.02	2.990	18.976	6.347
K00117.02	K00117.01	3.009	4.901	14.749
K01835.02	K01835.03	3.010	2.248	6.767
K00664.02	K00664.03	3.013	7.782	23.443
K02092.02	K02092.03	3.015	25.564	77.086
K02218.01	K02218.02	3.022	5.535	16.726
K00952.02	K00952.04	3.022	8.752	2.896
K00542.01	K00542.02	3.031	41.885	13.817
K00435.01	K00435.05	3.032	20.550	62.303
K01832.02	K01832.03	3.034	12.762	38.715
K06097.01	K06097.03	3.034	93.057	282.343
K02038.01	K02038.04	3.036	8.305	25.215
K01713.02	K01713.01	3.047	2.240	6.828
K00232.01	K00232.04	3.048	12.466	37.996
K01589.02	K01589.04	3.050	12.883	4.225
K04500.02	K04500.03	3.050	44.985	14.751
K01563.01	K01563.04	3.051	5.487	16.739
K00597.03	K00597.01	3.051	52.815	17.308
K00082.01	K00082.05	3.054	16.146	5.287

5:3

KOIs		Period Ratio	Periods (d)	
K00413.01	K00413.02	1.6202	15.2290	24.6746
K02352.01	K02352.03	1.6220	13.3916	8.2563
K00117.02	K00117.04	1.6237	4.9014	7.9583
K01589.03	K01589.05	1.6239	27.4346	44.5520
K02029.01	K02029.02	1.6243	16.3327	10.0555
K00912.01	K00912.02	1.6269	10.8485	6.6683
K00566.01	K00566.03	1.6271	25.8550	42.0686
K02243.01	K02243.02	1.6311	5.1856	8.4581
K01940.01	K01940.02	1.6320	10.9947	6.7368
K00719.02	K00719.03	1.6323	28.1224	45.9030
K02704.01	K02704.02	1.6324	4.8712	2.9842
K03083.01	K03083.02	1.6340	10.1832	6.2321
K01920.01	K01920.02	1.6345	16.5710	10.1385
K00945.02	K00945.03	1.6404	40.7156	66.7893
K02612.01	K02612.02	1.6419	4.6123	7.5730
K00733.02	K00733.04	1.6427	11.3493	18.6435
K01165.01	K01165.02	1.6433	7.0539	4.2926
K01598.01	K01598.02	1.6445	56.4758	92.8747
K06209.01	K06209.02	1.6449	12.7144	7.7297
K04435.01	K04435.02	1.6452	10.8614	17.8694
K02263.03	K02263.02	1.6452	15.5944	9.4785
K02236.01	K02236.02	1.6483	19.9866	12.1258
K00505.01	K00505.04	1.6491	13.7671	8.3482
K00070.04	K00070.02	1.6500	6.0986	3.6961
K00707.01	K00707.04	1.6527	21.7757	13.1756
K00271.01	K00271.02	1.6545	48.6304	29.3934
K02433.02	K02433.06	1.6565	10.0438	6.0633
K06145.01	K06145.02	1.6600	19.6723	32.6570
K04034.01	K04034.02	1.6663	6.9670	11.6089
K02261.01	K02261.02	1.6664	3.9760	6.6255
K01574.01	K01574.02	1.6668	114.7366	191.2391
K02163.01	K02163.02	1.6675	10.6649	17.7838
K02086.01	K02086.03	1.6681	7.1329	11.8985
K04136.01	K04136.02	1.6685	2.4175	4.0336
K02169.01	K02169.02	1.6693	5.4530	3.2666
K02693.02	K02693.03	1.6709	11.4194	6.8344
K00582.01	K00582.03	1.6719	5.9450	9.9396
K01151.01	K01151.04	1.672	10.435	17.453
K00993.01	K00993.02	1.673	21.854	13.061
K02704.01	K02704.03	1.674	4.871	8.153
K02693.01	K02693.03	1.675	4.081	6.834
K00314.01	K00314.02	1.675	13.781	23.089
K00972.01	K00972.02	1.677	13.119	7.822
K00571.02	K00571.04	1.679	13.343	22.408
K04383.01	K04383.02	1.680	4.342	2.584
K00490.01	K00490.03	1.686	4.393	7.406
K00351.02	K00351.07	1.686	210.601	124.923
K00547.03	K00547.02	1.686	12.386	7.347
K00664.01	K00664.02	1.688	13.137	7.782
K03470.01	K03470.02	1.689	15.062	25.434
K04846.02	K04846.01	1.689	32.527	19.255
K03398.01	K03398.03	1.692	7.319	4.327
K00352.01	K00352.02	1.692	27.082	16.007
K01060.01	K01060.03	1.693	12.110	20.497
K01221.01	K01221.02	1.694	30.160	51.077
K04500.01	K04500.03	1.695	8.702	14.751
K02842.02	K02842.03	1.696	5.149	3.036
K00283.01	K00283.03	1.696	16.092	9.488
K01364.02	K01364.03	1.698	7.056	11.979
K00658.01	K00658.02	1.698	3.163	5.371
K03068.01	K03068.02	1.698	3.917	6.652
K00082.01	K00082.03	1.700	16.146	27.454
K00408.01	K00408.02	1.702	7.382	12.561
K01413.01	K01413.02	1.702	12.645	21.526
K00220.01	K00220.02	1.703	2.422	4.125
K03158.02	K03158.04	1.703	4.546	7.743
K00248.02	K00248.04	1.704	10.913	18.596
K01306.02	K01306.03	1.705	3.468	5.914
K02926.01	K02926.03	1.706	12.285	20.957
K01194.01	K01194.02	1.707	8.708	14.862
K02018.01	K02018.02	1.708	27.496	16.099
K00446.01	K00446.02	1.709	16.709	28.552
K01563.01	K01563.03	1.712	5.487	3.205

porated numerically by drawing 10 radius and stellar mass samples for each planet.

Figure 3.20 shows the distribution of the inner planet's period for the generated planet pairs and Kepler multi-planet systems. This period generally sets the dynamical timescale of the systems, including tidal circularization and the period ratio libration periods.

Figure 3.21 shows the distribution of the period ratio for the generated planet pairs before and after the stability run. More systems went unstable near to but not right at the exact commensurabilities, leading to some peaking even in the instantaneous (osculating) period ratios. This effect is intensified when time-averaged (see Figure 3.1).

Figure 3.22 shows the distribution of the mutual inclination for the generated planet pairs before and after the stability run. There is little difference from stability sculpting, and we do not anticipate mutual inclination to play a significant role in this resonance behavior. The mutual inclination does affect the ability to detect both planets via transit; however, as we are modeling the observed population and not the intrinsic population, this effect is not examined in this work.

Figure 3.23 shows the distribution of the magnitude of the difference in the longitudes of the pericenter ($|\varpi_1 - \varpi_2|$, such that 0 is aligned and π is anti-aligned) for the generated planet pairs, and Figure 3.24 the same for the arguments of the pericenter ($|\omega_1 - \omega_2|$). There is little indication of stability sculpting in these distributions, except perhaps a slight preference for aligned arguments of the pericenter in stable pairs near the 5:3 resonance. The effect of the alignment on the dynamical behavior on non-secular timescales is expected to be small.

The distribution of the combined eccentricities for the generated planet pairs can be found in text in Figure 3.2.

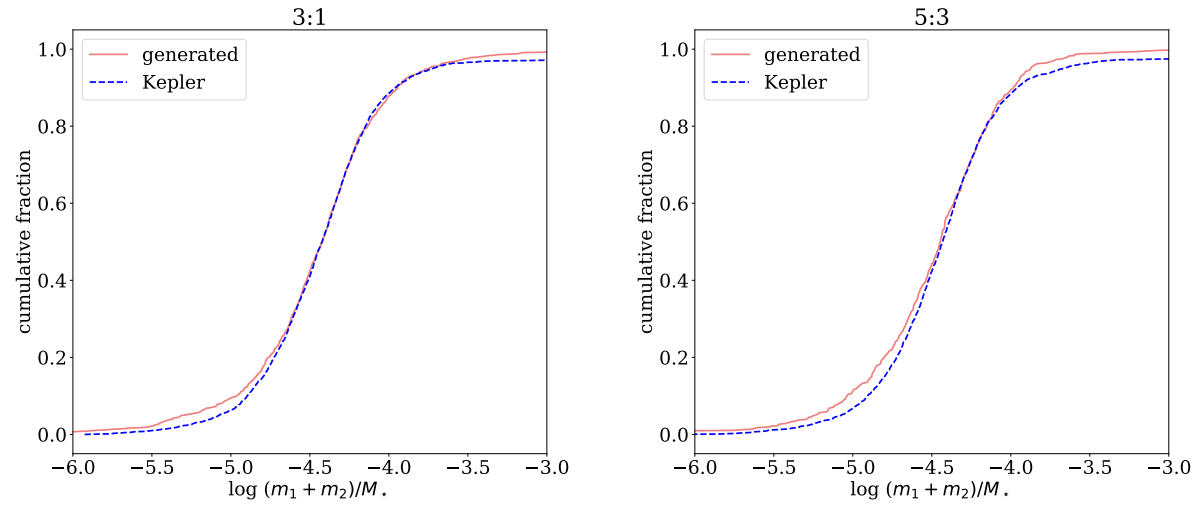

Figure 3.19: Cumulative fraction of the logarithm of the mass ratio of the planets to the star for the generated population of planet pairs (solid coral) and for planet pairs in the Kepler sample (dashed blue) for the (left) 3:1 and (right) 5:3 resonances.

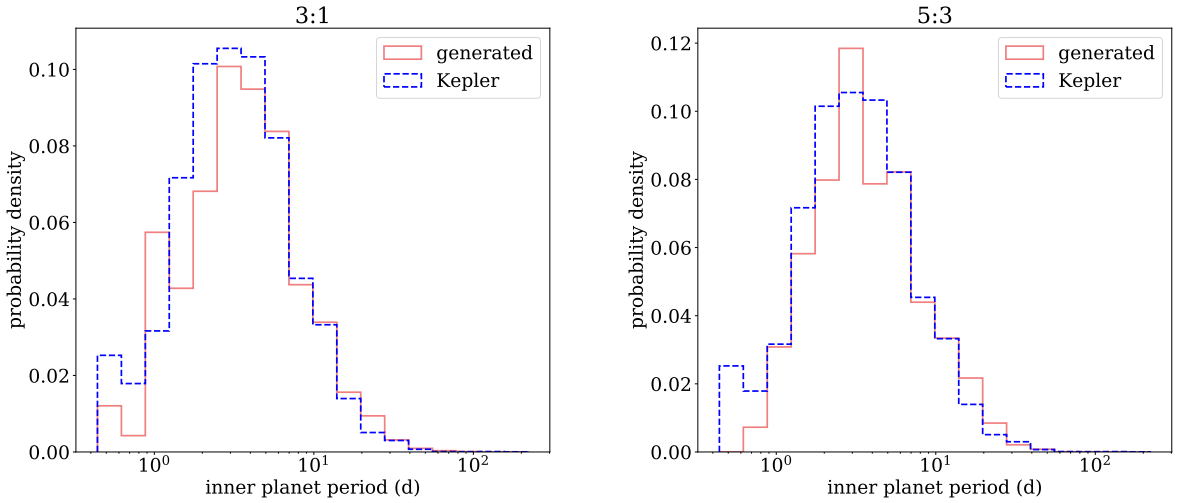

Figure 3.20: Distribution of the inner planet's period for the generated population of planet pairs (solid coral) and for planet pairs in the Kepler sample (dashed blue) for the (left) 3:1 and (right) 5:3 resonances.

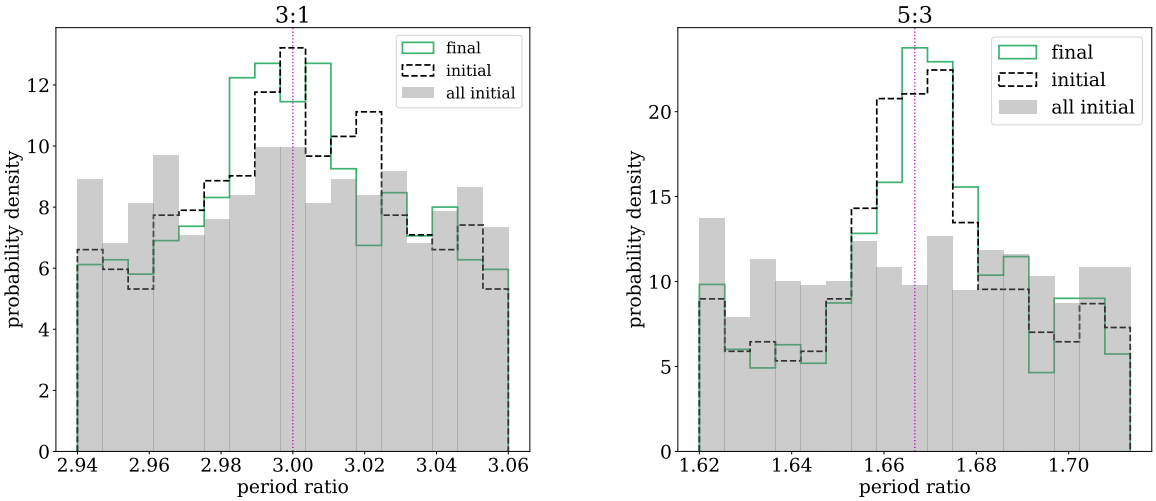

Figure 3.21: Distribution of the instantaneous period ratio of the final selected planet pairs at the beginning (dashed black) and end (solid green) of the stability run. The gray background shows the initial period ratios in this range for all planet pairs, including those that went unstable and were excluded from the final selection. Distributions are shown for the (left) 3:1 and (right) 5:3 resonances, and the exact commensurabilities are shown with a dotted pink line.

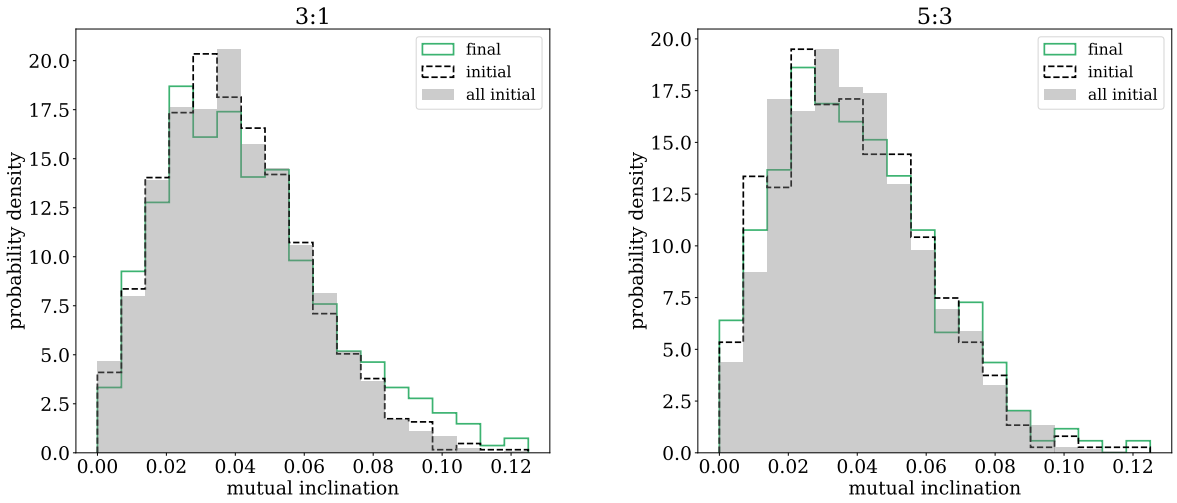

Figure 3.22: Distribution of the instantaneous mutual inclination of the final selected planet pairs at the beginning (dashed black) and end (solid green) of the stability run. The gray background shows the initial mutual inclinations for all planet pairs, including those that went unstable and were excluded from the final selection. Distributions are shown for the (left) 3:1 and (right) 5:3 resonances.

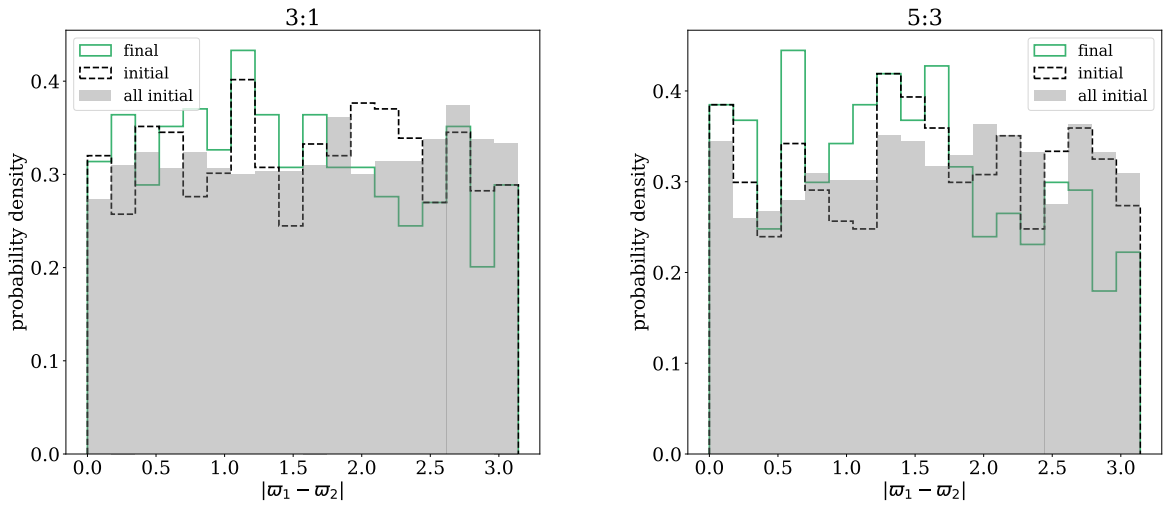

Figure 3.23: Distribution of the instantaneous magnitude of the difference in the longitudes of the pericenter (such that 0 is aligned and π is anti-aligned) of the final selected planet pairs at the beginning (dashed black) and end (solid green) of the stability run. The gray background shows the initial magnitude of the difference in the longitudes of the pericenter for all planet pairs, including those that went unstable and were excluded from the final selection. Distributions are shown for the (left) 3:1 and (right) 5:3 resonances. Their agreement shows the phasing of the orbits in the input systems and the randomized phasing share the same distributions.

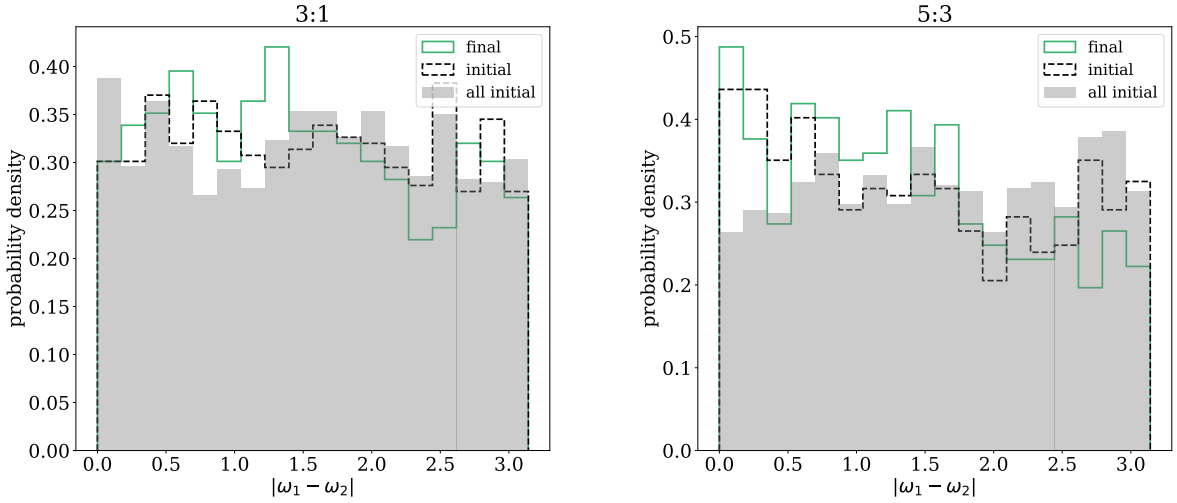

Figure 3.24: Distribution of the instantaneous magnitude of the difference in the arguments of the pericenter (such that 0 is aligned and π is anti-aligned) of the final selected planet pairs at the beginning (dashed black) and end (solid green) of the stability run. The gray background shows the initial magnitude of the difference in the arguments of the pericenter for all planet pairs, including those that went unstable and were excluded from the final selection. Distributions are shown for the (left) 3:1 and (right) 5:3 resonances.

CHAPTER 4

RELATIVE HABITABILITY OF EXOPLANET SYSTEMS WITH TWO GIANT PLANETS

The architecture of a planetary system can influence the habitability of a planet via orbital effects, especially as it impacts its eccentricity and stability. Some of these effects are readily apparent, particularly when they occur on short timescales that are easily numerically calculable. However, the appearance and evolution of life can take place on gigayear timescales, long enough that secular effects become important. These effects are difficult to investigate, as a direct integration requires significant computational time. In this chapter, I apply a semi-analytic framework in conjunction with N-body integrations and predictive techniques to determine the relative habitability for an Earth-like planet in a system with two giant companions over a multidimensional parameter space.

I find trends with mass, eccentricity, location, spacing, inclination, and alignment of the giant planets, including configurations where the system is more habitable due to the giant planets. As long as the system remains stable, a moderate eccentricity excitation of the terrestrial planet can be beneficial by increasing the outer boundary of the habitable zone through higher mean irradiance. Because eccentricity excitation from giant companions is not uniform throughout the system, the gain in the outer portion of the habitable zone is not necessarily offset by a loss from the inner portion. In my simulations, the median ($\pm 1\sigma$) habitable planet has an eccentricity of $0.11^{+0.16}_{-0.08}$, though it started circular. Low-mass, widely separated, and moderately eccentric perturbing giants can accomplish this, an "ultra-habitable" configuration of companions.

This chapter has been submitted to *Monthly Notices of the Royal Astronomical Society* and is expected to appear as Bailey and Fabrycky [2022], pending approval of minor revisions. The work described in this paper was performed by me under the guidance and supervision of my advisor (last author).

4.1 Introduction

Much work has been devoted to uncovering which aspects of the solar system are necessary to the phenomenon of life—particularly intelligent life—appearing on Earth. Extrapolating to a wider variety of planetary systems, such as those common in exoplanet architectures, can help us understand the ubiquity of the conditions for life in the galaxy. The interplay of factors that render a given planet habitable is exceedingly complex. This is a cross-disciplinary field of study with many potential knobs to turn. In this chapter, we approach the question from a planetary dynamics angle and examine effects of the architecture of a system on the habitability of an Earth twin—that is, a planet with the same planetary properties and host star as Earth, but with varying orbital properties and companions.

Previous work has examined the possibility of an Earth surviving in the architectures of known exoplanet systems [Agnew et al., 2018, Kokaia et al., 2020] and considered future target selection [Gascón et al., 2020]. Here, we consider the problem from a more theoretical perspective. What properties of giant planets might be key in determining the likely habitability of a system?

Much of the previous work has focused on instabilities due to mean-motion resonances (MMRs), as these have a strong capacity to disrupt or stabilize a system architecture. MMR-driven instabilities usually develop on short timescales [Smith and Lissauer, 2009, Obertas et al., 2017], with some exceptions [Wisdom, 1982, Barnes et al., 2015], but given the long timescales associated with the development of life, and particularly intelligent life, the stability of the system on secular timescales becomes important as well. Secular effects from giant planets have been shown to be important in the formation of planetary systems [Haghighipour and Winter, 2016]. Giant planets can also interact with binary companions, whether stellar or planetary, to create secular resonances relevant to the habitable zone [Bazsó et al., 2017, Denham et al., 2019].

We aim to examine which system architectures are dynamically conducive to a habitable

Earth twin on both short and long timescales. Given that Earth-like planets are sensitive to the architectures of their giant companions [Horner et al., 2020], we expect that having giant planets in a system will alter the relative habitability. Indeed, in our own solar system we see that the particulars of the configuration of the gas giant planets, Jupiter and Saturn, has implications for the habitability of our Earth [Pilat-Lohinger, 2015]. Agnew et al. [2019] conducted a study in a similar vein, using test particle simulations to predict the stability of habitable Earths with a giant planet—here we will consider the mass of the Earth and two giant planets. Having multiple giant planets allows for a more complex interplay of secular dynamics, which can lead to habitable zone effects even from cold giant planets.

The chapter is organized as follows: in Section 4.2 we outline the process we use to determine the relative habitability of a given architecture of two giant planets; in Section 4.3 we present and discuss our results of a one-dimensional analysis of two fiducial systems; in Section 4.4 we present and discuss our results of a multi-dimensional analysis across eight architecture parameters; the chapter concludes with Section 4.5.

4.2 Methods

4.2.1 Architecture Selection

Given the large variety of observed planetary system architectures (e.g. Lissauer et al. 2011, Fabrycky et al. 2014, Winn and Fabrycky 2015, Zhu and Dong 2021), the potential set of architectures to evaluate is almost limitless. For the sake of completing an initial examination in this work, we will restrict ourselves to considering strictly an Earth-like planet and two giant planet companions around a Sun-like star. The range of parameter space covered is summarized in Table 4.1. For giant companions, we consider a mass range from 0.1 to 10 M_{Jup}, covering sub-Saturns to super-Jupiters.

Our Earth analogs are placed uniformly between 0.6 and 1.9 AU to provide informa-

parameter	unit	min	max	scale	number
m_1	M_{Jup}	0.1	10	linear	4
m_2	M_{Jup}	0.1	10	linear	4
a_1	AU	10^{-1}	10	logarithmic*	8
α		$10^{-0.7}$	$10^{-0.12}$	logarithmic	8
$a_\oplus$	AU	0.6	1.9	linear	80
e_1		0	$10^{-0.04}$	logarithmic†	6
e_2		0	$10^{-0.04}$	logarithmic†	6
$\Delta\varpi$	rad	0	π	linear	2
inclination‡	rad	0	$\pi/9$	linear	2

*There is a break in the logarithmic scale at $a_1 = 10^{0.1}$, with three evenly spaced below (inclusive) and five evenly spaced above.
†The lowest eccentricity, $e = 10^{-2}$, was replaced with $e = 0$.
‡There are two inclination cases, one with $i_1 = i_2 = i_\oplus = 0$ and one with nonzero inclinations assigned to the giant planets ($i_1 = 14.1°$, $i_2 = 1.4°$).

Table 4.1: Range of parameters varied in our set of simulations.

tion about the entire extent of the habitable zone (see Section 4.2.4 for details about our habitability model). To cover giant planet configurations that are interior, exterior, or surrounding the Earth, we place the inner giant planet (planet 1) on a range between 0.1 and 10 AU and set the location of the outer giant planet (planet 2) based on a given semi-major axis ratio, $\alpha = {}^{a_1}/_{a_2}$.

Planets that are sufficiently close to one another will experience large enough perturbations to render a system unstable. The spacing at which this happens depends on many factors, but several previous studies have established a linear relationship between the logarithm of the time for a system to become unstable and the initial planetary separation in mutual Hill radii [Chambers et al., 1996, Smith and Lissauer, 2009, Morrison and Kratter, 2016, Obertas et al., 2017]. We use recent results from Lissauer and Gavino [2021] to set a limit for our giant planets of $\beta = 7.15$ in mutual Hill radii spacing. We apply this limit to the least massive configuration ($m_1 = m_2 = 0.1\ M_{Jup}$) to set the highest α in our parameter space at $10^{-0.12}$ (~ 0.76). For the most massive configuration ($m_1 = m_2 = 10\ M_{Jup}$), our lowest α of $10^{-0.7}$ (~ 0.20) is above the $\beta = 7.15$ limit.

In eccentricity, we cover a range from circular to high for both giant planets, with a maximum $e = 10^{-.04} \sim 0.91$. Given that we expect more stable systems at low eccentricity, we use a logarithmic scale to provide more resolution at low eccentricity, although we replace the lowest eccentricity ($e = 10^{-2}$) with the circular case. We consider two different eccentricity alignments, the perfectly aligned case ($\Delta\varpi = 0$) and the antialigned case ($\Delta\varpi = \pi$).

Finally, we consider two different inclination cases. The first is the coplanar case, where all three planets have zero inclination. The second is a case including mutual inclinations by assigning each giant planet the same inclination ($i_1 = 14.1°$ and $i_2 = 1.4°$; these values were chosen randomly) for each simulation in the non-coplanar case (the longitudes of the ascending nodes, Ω, are always set to 0).

For each configuration of the giant planets, four sets of mean anomalies are randomly generated uniformly between 0 and 2π and an Earth is placed at 1 AU. The stability for each of these four systems is estimated using the `SPOCK` machine-learning model [Tamayo et al., 2020]. The set of mean anomalies with the highest predicted stability is then used for each of the systems with changing Earth location generated for that giant planet configuration. This method is used to reduce the likelihood of choosing a particularly unstable initial condition for the systems.

To maintain the computational load in a reasonable timeframe, we use four variations of each of the giant planet parameters m_1 and m_2, six variations of e_1 and e_2, and eight variations of a_1 and α. We use 80 steps in the Earth's semi-major axis, as we calculated this to be the minimum number of steps to resolve the widths of secular resonances that fall in the habitable zone. A numerical test from a small sample of configurations using 160 steps saw no significant variation in results, confirming that we are not resolution-limited at this number. With the two $\Delta\varpi$ cases and the two inclination cases, this brings our total number of configurations evaluated to 1.179648×10^7, with 147,456 different giant planet configurations evaluated for relative habitability.

Fiducial Systems

In addition to this complete multi-dimensional set of architectures, we also conduct a one-dimensional analysis of two fiducial systems varying one parameter at a time. This allows us to increase the resolution of the parameters by a factor of ten. The parameters of the first fiducial system are set at $a_1 = 4$ AU, $\alpha = 0.32$, $m_1 = m_2 = 1\ M_{Jup}$, $e_1 = e_2 = 0.05$, $i_1 = i_2 = i_\oplus = 0$, and $\Delta\varpi = \pi$. The parameters of the second fiducial system are the same except that $a_1 = 0.15$ AU, making the second fiducial system one in which the giant planets are interior to the Earth analogs. In this one-dimensional analysis, we also vary the inclination of each planet in 50 steps from 0 to π and the eccentricity alignment of the giant planets in 20 steps from 0 to π. The mean anomalies are randomly chosen for the fiducial system and remain fixed for all simulations.

4.2.2 Process

For each 3-planet system, we utilize the following procedure for determining the stability outcome of that configuration. If at any step the configuration is deemed unstable, the outcome is set to zero and the remaining steps are skipped.

This is an overview; the details of each part of the process are discussed further in the following sections.

1. Check if the giant planets alone are expected to be stable based on the 2-planet analytical stability criterion of Hadden and Lithwick [2018].

2. *If minimum period ratio* > 1.4*:* Calculate the minimum orbital separations of all planets over 10^9 orbits using Laplace-Lagrange theory. If any are less than zero, the system is considered unstable.

3. Calculate stability prediction from `SPOCK`'s machine-learning model. If zero, the system is considered unstable.

4. Calculate the spectral fraction of the system as described by Volk and Malhotra [2020]. This calculation requires integrating the system for 5×10^6 orbits of the inner planet. If the system goes unstable during the integration (as determined by orbit crossing, colliding with the star, or an unbound planet), the system is considered unstable. If the maximum AMD spectral fraction is above the stability threshold of 0.05, the system is considered unstable.

5. If the system has not been ruled unstable, the stability outcome is set to the stability prediction value from `SPOCK`.

We also calculate the maximum eccentricity of the Earth for each configuration, taken from the 5×10^6-orbit integration done during the spectral fraction calculation. The outcome values, outcome codes (which indicate which step, if any, flagged the system as unstable), and maximum Earth eccentricities are the outputs saved for each configuration.

Using both the stability outcome and a habitable zone model that takes into account eccentricity, we determine the probable habitability of each three-planet configuration. We then integrate this habitability probability over the range of Earth semi-major axes for each giant planet configuration and compare to the integrated area for an unperturbed system. This calculation gives our final results: a relative habitability for each giant planet configuration.

Throughout this work, we do not include error estimates on our relative habitability results. There are many sources of potential error, including: each of the instability predictions; the outcome of a given N-body simulation; the effect of the planets' mean anomalies; the resolution of our Earth semi-major axes; the resolution in time of an N-body simulation and the maximum eccentricity calculation; our choice of habitability model and the associated calculations. Without a method of quantifying these systematic uncertainties, we choose instead to omit assigning an error, and we primarily focus on relative trends more than exact numbers in our results.

4.2.3 Stability Outcomes

Instabilities from Mean-Motion Resonances

Instabilities in multi-planet systems are often driven by the overlap of MMRs [Wisdom, 1980, Mardling, 2008, Deck et al., 2013]. For two-planet systems, Hadden and Lithwick [2018] found an analytical solution that predicts the onset of instability, accounting for resonances of all orders. We use their Equation 16 to calculate the relative eccentricity, Z, of the two giant planets and their Equation 19 to calculate the approximate critical Z for the onset of chaos, Z_{crit}. If $Z \geq Z_{crit}$, the system is considered unstable.

This criterion neglects the Earth analog. Given that the mass ratio between the Earth and the other planets is at most 1.57×10^{-2}, we do not expect the addition of the Earth analog to significantly alter the chaos map of the system. Additionally, throughout all our stability analysis, we consider any planet going unstable to be an unstable system. It is possible that the Earth analog could survive instability between the giant planets (i.e. Kokaia et al. 2020), but the resulting post-instability configuration of the system would not be the same as the configuration we were considering. Thus our giant planet configurations should be seen as a final state of the system—that which might be observable—rather than an initial state.

For three-planet systems, both 2-body and 3-body MMRs interact in a complex manner that makes analytical predictions of instability difficult. Tamayo et al. [2020] use machine-learning techniques to develop a model that can predict long-term instability (up to 10^9 orbits) from a numerical N-body integration of only 10^4 orbits. This model is implemented in the Stability of Planetary Orbital Configurations Klassifier (`SPOCK`) package[1]. Because the model is trained with an emphasis on MMRs, it is primarily useful for identifying systems that are unstable due to MMRs.

The stability prediction from `SPOCK` takes the form of a probability between 0 (completely

1. https://github.com/dtamayo/spock

unstable) and 1 (completely stable). For any system that is not considered unstable from another mechanism, we use the calculated stability prediction as the system's outcome.

Secular Instabilities

It is possible for a system to be stable to MMR-related instabilities but still develop long-term instabilities on secular timescales. These instabilities may arise due to secular chaos and overlapping secular resonances; for example, the marginal stability of Mercury within the solar system [Laskar, 2008, Lithwick and Wu, 2011].

Evaluating the secular stability of a system is a nontrivial problem. Direct numerical integrations take an enormous amount of computing power, and analytical predictions are complicated by the required high-order dependencies to capture complicated secular behavior for non-circular, non-coplanar systems [e.g., Libert and Henrard 2008, Migaszewski and Goździewski 2008, Bailey and Fabrycky 2020]. We take two approaches to evaluating secular stability.

The first is applying the Laplace-Lagrange approximation to the system to calculate the eccentricities of all three planets over 10^9 orbits [Murray and Dermott, 1999, Ch. 7]. This approximation suffers from losses in accuracy with increasing e, i, and/or α. Thus we only use this in systems where the smallest period ratio is greater than 1.4. We chose this value based on testing of fifty systems comparing maximum eccentricities between Laplace-Lagrange theory and N-body results. Further, we use this analytical treatment to test for extremes and not to determine exact orbital parameters for the system (i.e., we do not consider the Laplace-Lagrange solution when setting the maximum Earth eccentricity during the habitability analysis).

We find the three points in time when each of the planets has its maximum eccentricity. Because the Earth is much less massive than the giant planets, its calculated eccentricity is less accurate. For example, if the Earth lies in a secular resonance, its eccentricity can be

excited to > 1 according to Laplace-Lagrange theory, which breaks down when approaching secular resonance. Therefore we include the Earth as a massive planet in this approximation, but when analyzing these three points we set the Earth eccentricity to zero rather than using its calculated eccentricity. For all three points in time, we calculate the orbital separations (the distance between a planet's apocenter and the next planet's pericenter) between the planets. If any separation is negative, we consider that system to be unstable due to predicted orbit crossing.

The second method we use for determining secular stability is the spectral fraction method. Volk and Malhotra [2020] developed the technique of using a system's spectral fraction over a 5×10^6-orbit integration to predict stability on a timescale of 5×10^9 orbits.

Spectral fraction is calculated as the fraction of frequencies in a fast Fourier transform of a time series of orbital elements that have a power of $\geq$5% of the peak frequency's power. Volk and Malhotra [2020] found that the angular momentum deficit (AMD) spectral fraction is the most predictive of instability, where AMD for a given planet is calculated as

$$\text{AMD} = \frac{mM_\star}{m + M_\star}\sqrt{G(m + M_\star)a}\,(1 - \sqrt{1 - e^2}\cos i), \tag{4.1}$$

with G being the universal gravitational constant; $M_\star$ the mass of the star; and m, a, e, and i the mass, semi-major axis, eccentricity, and inclination of the planet. For systems not strongly influenced by MMRs, a high spectral fraction (above $\sim$0.01-0.02) is correlated with a low chance of long-term stability. Given that we remove the MMR-unstable systems in an earlier portion of our analysis, we can use the spectral fraction to remove systems likely to be long-term unstable due to secular effects.

We use the `REBOUND` package [Rein and Liu, 2012] with the WHFast integrator [Rein and Tamayo, 2015] (50 steps per innermost orbit) to perform the integrations for each system. The AMD for each planet is calculated over 3000 steps, and a real one-dimensional discrete Fourier transform is used to calculate the AMD power spectra.

Spectral Fraction Testing We tested the performance of the AMD spectral fraction in predicting long-term instability by creating 100 random systems consisting of an Earth and two Jupiters around a Sun-like star.

The inner Jupiter's period was randomly chosen uniformly between 3000 and 5000 days, and the period ratio with the outer Jupiter was randomly chosen in log space between 1.77 and 10, avoiding first and second-order MMRs.

Using Laplace-Lagrange secular theory, we found the predicted locations of the secular resonances of this Jupiter pair. The Earth was then placed in between the locations predicted for the inclination-node secular resonance and one of the eccentricity-pericenter secular resonances. This method was used to create configurations that might be in regions affected by secular resonance overlap. Additionally, given our interest in the dynamical habitability, it was enforced that the Earth must fall into the habitable zone, using the limits of Kopparapu et al. [2013] between 0.97 and 1.7 AU.

Mild initial eccentricities and inclinations were assigned to all three planets using Rayleigh distributions with scales of 0.049 for e [Van Eylen and Albrecht, 2015] and 0.032 rad for i [Fabrycky et al., 2014].

Lastly, we required that `SPOCK` must predict stability of at least 0.70. Our intended use of the spectral fraction calculation is to determine instability among systems not already predicted to be unstable.

With this set of 100 Earth-Jupiter-Jupiter systems, we calculated the AMD spectral fraction of the Earth as described above. We also integrated each of these systems for 5×10^9 orbits of the Earth using the WHFast integrator in `REBOUND`, using 50 steps per orbit.

No system had explicit orbit crossing or unbound planets over 5×10^9 orbits. However, the Earth's eccentricity was excited in the vast majority of systems, including 49 in which the Earth had a pericenter passage of less than 1 stellar radius, i.e., it would have collided

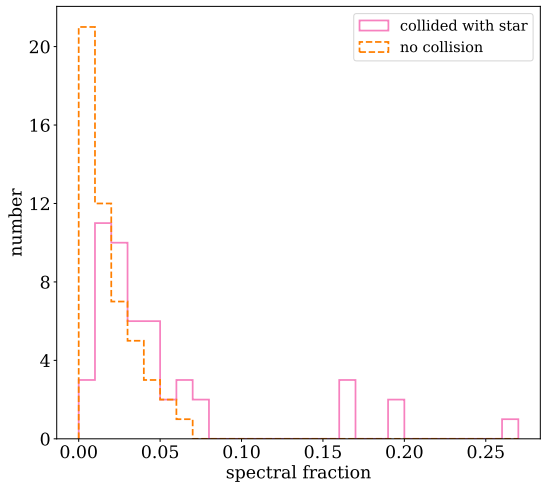

Figure 4.1: The distribution of AMD spectral fractions for the Earth in an Earth-Jupiter-Jupiter system for cases where the Earth collided with the central star and systems where it did not. A high spectral fraction is predictive of instability, but a low spectral fraction is not predictive of stability.

with the star. All of the systems with a spectral fraction greater than 0.07 resulted in a collision. The median spectral fraction for collision systems was 0.031, while the median spectral fraction for non-collision systems was 0.014. The distribution of spectral fractions is shown in Figure 4.1.

From this test, we conclude that, for systems such as we are interested in, the spectral fraction method is a good indicator of instability but not of stability. That is, a high spectral fraction meant the system was unstable, but the reverse was not true. Therefore we do not predict stability from spectral fraction, but we do use it to determine that a system is unstable. We use 0.05 as our threshold, slightly higher than that of Volk and Malhotra [2020].

4.2.4 Habitability Model

Habitability is an enormously complex topic with many complicating factors, many of which aren't even yet known. In order to quantify the habitability of a given system in this work, we use a probabilistic habitability model. The model we adopt is relatively simple, but this process could be adapted to work with models of varying complexity to incorporate many

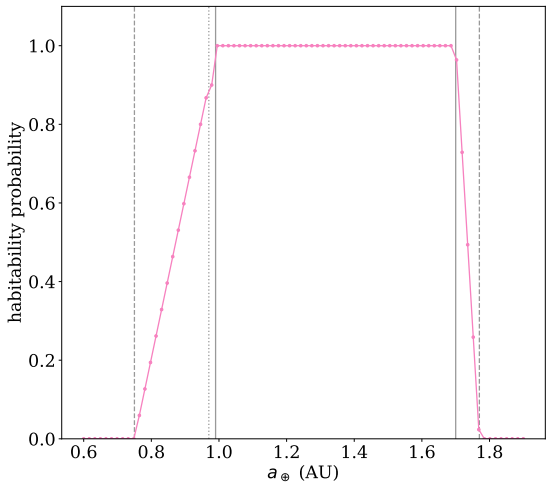

Figure 4.2: Our probabilistic model for habitability of an unperturbed Earth analog orbiting a Sun-like star. The vertical lines show the limits of the habitable zone from Kopparapu et al. [2013] (0.75 AU - recent Venus; 0.97 AU - runaway greenhouse; 0.99 AU - moist greenhouse; 1.70 AU - maximum greenhouse; 1.77 AU - early Mars). The points show the resolution in the Earth's semi-major axis used in our analyses.

more aspects of habitability.

The habitable zone (HZ) is a concept referring to the region around a star in which a planet can sustain liquid water on its surface. The location of the HZ is affected by planetary factors such as the planet's size, atmosphere, water content, etc. and by stellar factors such as spectral type and temperature. Numerous studies have examined the extent of the HZ in various systems; see Kopparapu et al. [2020] for a review.

The basis for our model is the limits of the HZ from Kopparapu et al. [2013] for circular ($e = 0$) planets. Between their conservative limits of 0.99 AU and 1.7 AU (based on the moist greenhouse limit for the inner HZ boundary and the maximum greenhouse for the outer HZ boundary), we set the probability of habitability to one. Between 0.99 AU and the runaway greenhouse limit, 0.97 AU, we set the probability of habitability to 0.9. Inwards of their optimistic limit of 0.77 AU for the inner HZ, based on the early Venus limit, and outwards of their optimistic limit of 1.77 AU, based on the early Mars limit, we set the probability of habitability to zero. Between the conservative and optimistic limits (between 0.97 AU and 0.77 AU on the inner edge and between 1.7 AU and 1.77 AU on the outer edge), the habitability probability decreases linearly. See Figure 4.2 for an illustration of this model. We take this to be our "unperturbed" system that we will use for comparison with our perturbed

systems. We note that we are comparing only perturbations from the giant planets; it is possible that an Earth-only system has eccentricity excitation from another mechanism (disk interactions, quadrupole moment of the star, etc.), which are neglected in our "unperturbed" reference system.

In addition to the semi-major axis of the Earth, we also wish to consider the impact of the Earth analog's eccentricity, which could become excited by the architecture of the system once the giant planets are added. The effect of eccentricity on the location of the HZ is a complex problem that has been the subject of many studies [e.g., Williams and Pollard 2002, Dressing et al. 2010, Kane et al. 2012, Linsenmeier et al. 2015, Bolmont et al. 2016, Way and Georgakarakos 2017, Méndez and Rivera-Valentín 2017, Kane and Torres 2017, Palubski et al. 2020]. A common approach is to use the mean flux approximation, which uses the average stellar flux received by a planet on an eccentric orbit to compare with the equivalent location of a circular orbit. However, Bolmont et al. [2016] use detailed climate models to show this approximation becomes unreliable at high eccentricities.

Eccentric HZ limits based on climate models, both 1-D and 3-D, are more accurate than analytical approximations but, due to extensive computation time and the profusion of variable parameter combinations, are difficult to use for generalized limits. Climate models have shown that increasing eccentricity can move the outer HZ limit further out [Williams and Pollard, 2002, Dressing et al., 2010], though the effect on the inner HZ limit is less well-studied. Further complication arises from the fact that seasonality is strongly affected by both eccentricity and obliquity [Linsenmeier et al., 2015], but we are neglecting the obliquity in this analysis.

For our model, we use the mean flux analytical approximation for eccentricities below 0.6. Because the mean flux scales with $(1-e^2)^{-1/2}$ [Williams and Pollard, 2002] for a given semi-major axis, and flux also scales with the inverse square of the semi-major axis, we can calculate an equivalent circular semi-major axis that receives the same mean flux as the

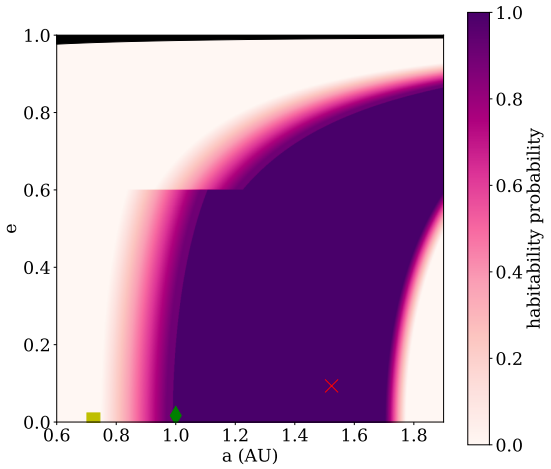

Figure 4.3: Our probabilistic model for habitability of an eccentric Earth analog orbiting a Sun-like star. The upper black region is disallowed due to collision with the star; present-day Venus (yellow square), Earth (green diamond), and Mars (red X) are shown for reference. Probabilities are calculated based on the circular HZ limits of Kopparapu et al. [2013] and the eccentricity scaling of the mean flux approximation for $e < 0.6$ and an estimated scaling based on Palubski et al. [2020] for $e \geq 0.6$.

planet with semi-major axis a and eccentricity e:

$$a_{\langle F \rangle} \;=\; a(1-e^2)^{1/4} \tag{4.2}$$

For higher eccentricities, where the mean flux approximation has been shown to be invalid, we look to Palubski et al. [2020]. They use a 1-D energy balance model to evaluate the eccentric habitable zone for Earth-like planets. Their Figure 7 shows how the habitable zone varies for different eccentricities and instellation. Their results shows a steeper relation than the $(1-e^2)^{1/4}$ scaling from the mean flux approximation. We fit by eye a scaling exponent of $(1-e^2)^{1/2.1}$ and use this scaling for planets with eccentricities greater than 0.6.

Figure 4.3 shows the habitability probability calculated by our model in $e-a$ space. Note the discontinuity at $e = 0.6$ due to our dual-method approach. The semi-major axis range shown is truncated based on where we place our Earth analogs; the outer boundary of the HZ continues to move outwards for increasing eccentricity, but the area of parameter space grows smaller and the likelihood of stability at these high eccentricities is low.

To determine the habitability probability for a given Earth analog, we calculate its equivalent circular semi-major axis based on its eccentricity via this model and then calculate the

habitability probability as described above for circular planets.

4.2.5 Example Relative Habitability Calculation

The output that we achieve from our combination of stability and habitability models is a single number that quantifies the relative habitability for a given configuration of two giant planets. In this section, we will illustrate how these models are used to provide our calculated output for one particular giant configuration.

This giant planet configuration is taken from the architectures based on the first fiducial system with $a_1 = 4$ AU, $\alpha = 0.32$, $m_1 = 1\ M_{Jup}$, $e_1 = e_2 = 0.05$, $i_1 = i_2 = i_\oplus = 0$, and $\Delta\varpi = \pi$, and here we take the mass of the outer giant planet (m_2) to be 10 M_{Jup}.

First, we get stability outcomes for each of the 80 Earth semi-major axes. The stability outcomes are shown in Figure 4.4 (top). The non-zero stability outcomes all come from the the `SPOCK` prediction. There are many reasons to get a stability outcome of zero (unstable), and the shaded background color in Figure 4.4 (top) indicates which step of the process (as described in Section 4.2.2) resulted in the unstable determination. This information is used only for our understanding, as the stability outcomes are treated the same regardless of their origin. In this example, we see instability during the 5×10^6-orbit numerical integration and instability predicted from a high spectral fraction.

Second, we calculate the habitability probability for an Earth analog at each given semi-major axis and eccentricity. We use the maximum eccentricity reached during the 5×10^6-orbit numerical integration for this; for any configuration that did not reach this step due to instability, the eccentricity remains at zero—this has no effect on the final output as the stability outcome is zero for those configurations. The variation in eccentricity over time may have additional habitability implications [Way and Georgakarakos, 2017], which we neglect here. Because our Earths may sometimes reside outside the outer boundary of the HZ, when developing our model we used the "cold start" results from Palubski et al. [2020], which

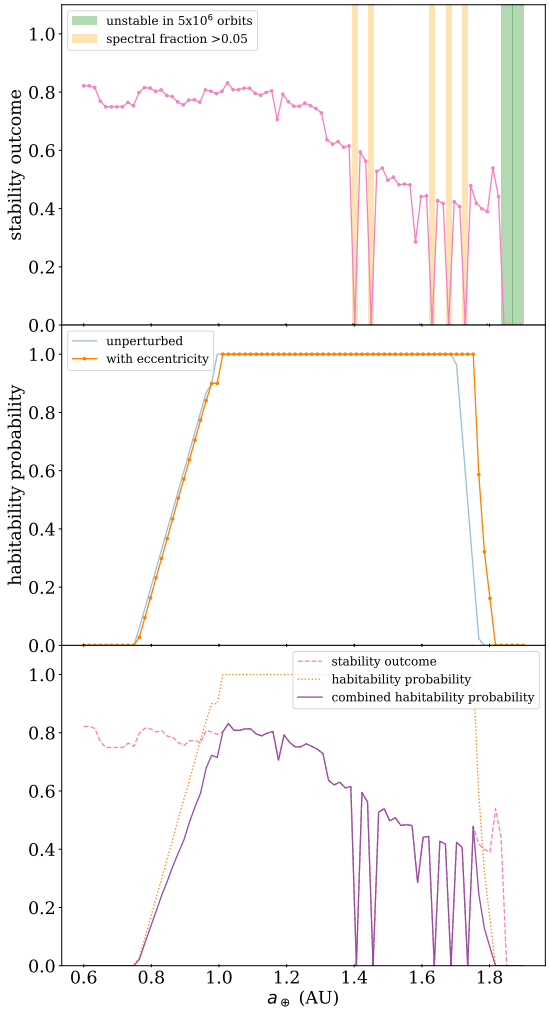

Figure 4.4: Illustration of the calculation of relative habitability for a single giant planet configuration. (top) The stability outcome for each of the 80 Earth locations. (middle) The habitability probability for each Earth given its location and eccentricity. The unperturbed habitability from Figure 4.2 is shown for reference. (bottom) The combined relative habitability curve obtained by multiplying the stability outcome and habitability probability. Integrating the area under the combined relative habitability curve and comparing with the area under the unperturbed habitability curve (Figure 4.2) gives the relative habitability for a given giant planet configuration (0.6152 for this example).

consider planets initially frozen.

The habitability probability for this example is shown in Figure 4.4 (middle). The overall shape is almost the same as the unperturbed habitability in Figure 4.2; this is common for most of our results as the eccentricity effect tends to be quite small. In this case, however, there is an increased habitability probability in the outer edge of the HZ that arises from the Earth getting an excited eccentricity that makes it more habitable in our model.

We combine our stability outcome and habitability probability into a combined habitability probability by multiplying them together for each Earth semi-major axis. The resulting curve in this case is shown in Figure 4.4 (bottom). At most points, either the stability outcome or the habitability probability dominates but, especially near the edges of the HZ, they both contribute to the result.

Finally, we integrate the area underneath this combined habitability probability curve. This is done numerically using an unsmoothed univariate spline as implemented in `SciPy` [Virtanen et al., 2020]. Here, the resulting area is 0.5304. We divide this area by the area underneath the unperturbed habitability curve (0.8649) to obtain the relative habitability for this giant planet configuration, given a uniform distribution of Earth-like planets: 0.6152.

4.3 One-Dimensional Analysis

4.3.1 Giants Exterior to HZ

Results

The first fiducial system we consider has a semi-major axis of 4 AU for the inner giant, placing the giants exterior to the HZ (except when a_1 is the parameter varied). See Table 4.1 and Section 4.2.1 for details.

The resulting relative habitability curves for each parameter are shown in Figure 4.5. Parameters that have the same range (m_1/m_2, e_1/e_2, and $i_1/i_2/i_\oplus$) are shown on the same

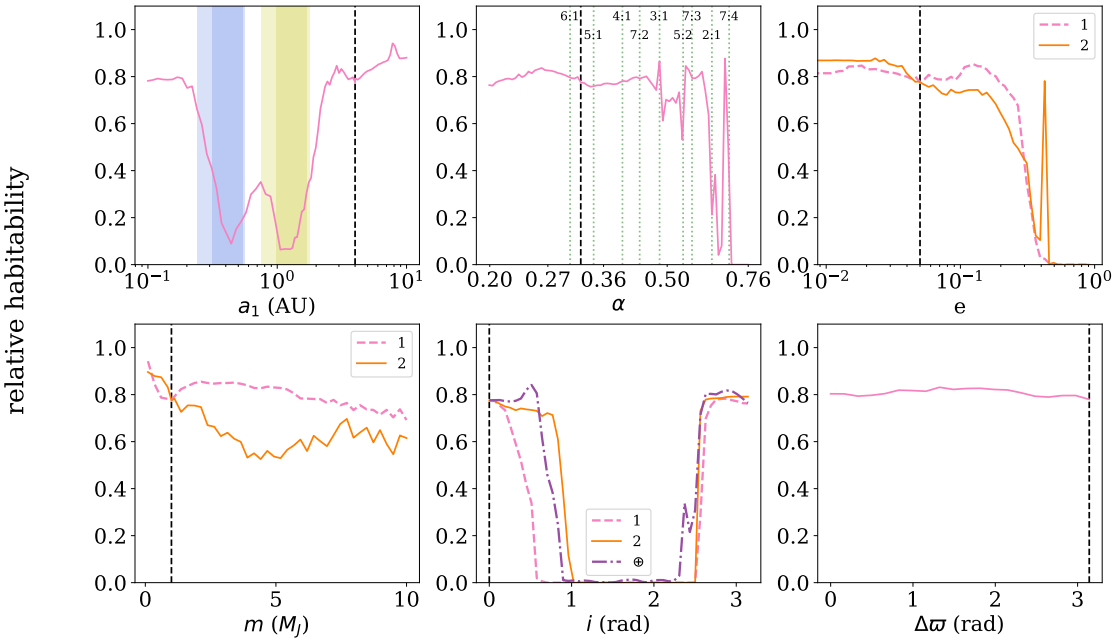

Figure 4.5: Relative habitability calculated for varied parameters by changing a single parameter of a fiducial system with exterior giant planets. The values of the fiducial system are indicated in each plot by a dashed vertical line. In the top left plot (a_1), the shaded background indicates when one of the giant planets is located within the habitable zone (yellow for the inner giant and blue for the outer giant; darker for the conservative limits and lighter for the optimistic limits). In the top center plot (α), several low-order mean-motion resonances have been indicated by dotted green lines and labeled with the associated resonance.

axes for compactness, but all the parameters were varied independently. The values of the fiducial system are indicated on each plot.

Discussion

There are several prominent features in Figure 4.5.

First, let's consider the impact of changing the a_1 parameter. Note that because α is fixed, this also changes the location of planet 2 (a_2) as well. Unsurprisingly, the relative habitability decreases significantly when the giant planets are located in or near the HZ. There is a local maxima at $a_1 = 0.745$ ($a_2 = 2.328$). This is due to the small region of stability between the two giant planets falling in the middle of the HZ. We note there appear to be small peaks at ∼3 and 7.8 AU, but we find no clear reason that seems to explain these; it is possible they may not be significant.

As α increases, the giant planets get closer together by moving planet 2 inward. At $\alpha = 0.7$ and higher, the giant planets are so close together that they are unstable by the analytical criterion of Hadden and Lithwick [2018]. Most of the other features correspond with period ratios near commensurability, giving rise to instabilities based on MMR. For example, the first-order 2:1 MMR corresponds with an α of 0.63 (by Kepler's Third Law, $\alpha \sim ({}^{P_2}/_{P_1})^{-2/3}$), where there is a deep and broad dip in the relative habitability. Smaller dips occur near higher-order MMRs, such as the 5:2 resonance ($\alpha \sim 0.54$) and the 3:1 resonance ($\alpha \sim 0.48$).

At high eccentricities, we expect instabilities to develop as orbits cross. Nominal orbit crossing between the giant planets occurs at $e_2 = 0.664$ and between planet 1 and the outer HZ at $e_1 = 0.558$. In actuality, we see the relative habitability fall off due to instability at an eccentricity of approximately 0.3 for either giant planet. Interestingly, there is a strong spike in relative habitability at $e_2 = 0.424$. This is due to a resonance in the precession of the eccentricity vectors of the giant planets. The resonance stabilizes the system by preventing

the Earth's eccentricity from being excited, which is what is causing the instability leading to low relative habitability on either side of the resonance.

As the mass of either giant planet changes, we don't see drastic peaks or dips in the relative habitability. However, there is a trend towards reduced relative habitability as the mass increases, and the trend is stronger when it is planet 2 with more mass. This seems to be a combination of two effects: there are consistently slightly more Earth locations that result in instability when a given mass is assigned to m_2 than m_1, and those instabilities tend to fall in the middle of the HZ. This trend is likely associated with the secular resonances within the systems. In Laplace-Lagrange theory, the resonance location for a test particle varies with the mass ratio of the two massive planets (m_1/m_2), and at mass ratios of less than about 0.5, the secular resonance locations for one of the eccentricity-pericenter resonances and the inclination-node resonance start to fall in the HZ for the fiducial configuration. The two resonance locations also become closer to one another as the mass ratio decreases, increasing the potential for overlapping resonances and secular chaos.

The same general trend is seen for all three planets when their inclination is changed. For relatively coplanar systems, prograde or retrograde, the relative habitability is largely unaffected. When one of the planets is strongly misaligned, the systems tend to be unstable. Because the Earth is interior to the giant planets, its instability arises from high eccentricities driven by Kozai-Lidov cycles once its inclination is high enough relative to the outer planets [Kozai, 1962, Lidov, 1962, Lithwick and Naoz, 2011]. For misaligned prograde orbits, the relative habitability is more sensitive to the inclincation of planet 1 and drops off before the critical inclination for Kozai-Lidov is reached. Even mild amounts of mutual inclination can lead to chaotic eccentricities [Boué et al., 2012] that can destabilize systems.

Lastly, we see almost no effect from changing the alignment of the giant planets' pericenters. This is not unexpected, as the fiducial system has very low amounts of eccentricity. This parameter would likely have more effect for systems of higher eccentricity; for example,

one can imagine the spike in e_2 might change in size or location for a different alignment of the planets.

4.3.2 Giants Interior to HZ

Results

The second fiducial system we consider has a semi-major axis of 0.15 AU for the inner giant, placing both of the giants interior to the HZ (except when a_1 is the parameter varied). See Table 4.1 and Section 4.2.1 for details.

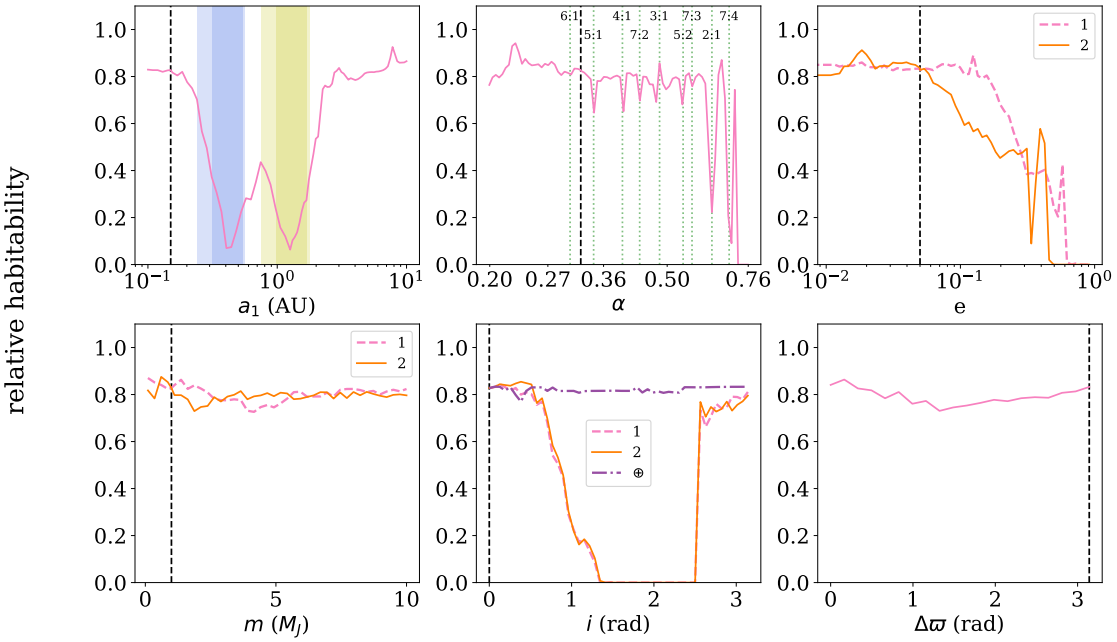

Figure 4.6: Relative habitability calculated for varied parameters by changing a single parameter of a fiducial system with interior giant planets. The values of the fiducial system are indicated in each plot by a dashed vertical line. In the top left plot (a_1), the shaded background indicates when one of the giant planets is located within the habitable zone (yellow for the inner giant and blue for the outer giant; darker for the conservative limits and lighter for the optimistic limits). In the top center plot (α), several low-order mean-motion resonances have been indicated by dotted green lines and labeled with the associated resonance.

The resulting relative habitability curves for each parameter are shown in Figure 4.6. Parameters that have the same range (m_1/m_2, e_1/e_2, and $i_1/i_2/i_\oplus$) are shown on the same axes for compactness, but all the parameters were varied independently. The values of the fiducial system are indicated on each plot.

Discussion

The relative habitability curves for the parameters of the interior fiducial system (Figure 4.6) are similar to those of the exterior fiducial system, though some key differences exist.

First, the results for the a_1 parameter are almost identical, as expected, because these systems are the same in each case (as the second fiducial system is the same as the first with a different a_1). However, these were integrated and calculated independently, which provides a good check on the repeatability of our results.

For the α parameter, the overall behavior is quite similar to the previous results, falling off at high α, but we see more narrow peaks emerge. These peaks also correspond with MMRs, those of even higher orders; for example, the 7:3 resonance ($\alpha \sim 0.57$), the 5:1 resonance ($\alpha \sim 0.34$), and even the 7:2 resonance ($\alpha \sim 0.44$). Interestingly, there seems to be some protection at the exact 3:1 resonance. The stronger effect from the higher-order MMRs is likely because the overall system is more compact and more easily destabilized.

For the eccentricities of the giant planets, again the trends are similar to the exterior case. The relative habitability begins to fall off at around the same e_1, but here the slope of the decline is less steep and some relative habitability remains out to much higher e_1. This can be understood as planet 1 is no longer the planet neighboring the HZ, so at high e_1 there are fewer opportunities to destabilize the system. For planet 2, in this case the relative habitability begins to decrease at a lower e_2; again, this is due to the ordering of the planets, as planet 2 is now the planet adjacent to the HZ ($a_2 = 0.4687$ AU). The same feature at $e_2 \sim 0.4$ appears, although with slightly less amplitude.

The trends of relative habitability with the mass of either giant planet are different here than in the exterior case. Here, it does not matter which planet's mass is changed, and there is very little decrease of relative habitability with increasing mass. Again we can look to Laplace-Lagrange secular theory to make sense of this. While the locations of the inclination-node and first eccentricity-pericenter secular resonances still enter the HZ for low mass ratios, they stay only in the inner edge of the HZ where the relative habitability is already low, and the secular resonance locations are not as close together, giving less opportunity for overlap. The second eccentricity-pericenter secular resonance does fall in the middle of the HZ, but it does so for all mass ratios and is well-separated from the other two secular resonances.

We see a very notable difference with the effect of inclination in this case. There is virtually no effect from changing to inclination of the Earth. This is because the Earth, which has a tiny mass relative to the giants, is now the outer planet and, while it may be subject to inclination oscillations from the Kozai-Lidov effect, the eccentricity is not expected to be excited to extremes [Naoz et al., 2017]. Nor is the effect of the Earth's inclination significant enough to destabilize the inner giant planets, regardless of its mutual inclination. However, we see that at high inclinations of either giant planet, there is no relative habitability. This is because of Kozai-Lidov effects on the inner planet when there is a large misalignment with the middle planet (the outer giant). We note that the effect is virtually identical no matter which planet's inclination is changed, unlike in the previous case, where the relative habitability was more sensitive to planet 1's inclination. Lastly, we similarly see very little effect from the relative alignments of the giant planets' pericenters. There is a small decrease near perpendicular alignments, which is likely because the giant planets are closer together in this case and so even at the same mild eccentricities there are slightly stronger dynamical effects.

4.4 Multi-Dimensional Analysis

4.4.1 Results

The compiled results for all 147,456 giant planet configurations are included in Table 4.2 (see Appendix 4.6.1 for the stability outcome results prior to the habitability model being applied). Only a subset of the results are shown here, but the entire table is available to download[2].

m_1 (M_{Jup})	m_2 (M_{Jup})	a_1 (AU)	α	e_1	e_2	Δi (rad)	$\Delta\varpi$ (rad)	relative habitability
0.1	0.1	1.90546071796325	0.19952623149689	0.02466039337234	0.91201083935591	-0.22165681500328	3.14159265358979	0.00000000000000
0.1	0.1	6.60693448007596	0.19952623149689	0.14996848355024	0.06081350012787	0.00000000000000	3.14159265358979	0.92961440310821
0.1	0.1	6.60693448007596	0.42798502294486	0.00000000000000	0.00000000000000	-0.22165681500328	0.00000000000000	0.93437618202497
0.1	0.1	10.00000000000000	0.29222292648815	0.14996848355024	0.91201083935591	0.00000000000000	0.00000000000000	0.00000000000000
0.1	0.1	10.00000000000000	0.29222292648815	0.36982817978027	0.00000000000000	0.00000000000000	0.00000000000000	1.10954892015974
0.1	6.7	1.25892541179417	0.29222292648815	0.14996848355024	0.14996848355024	0.00000000000000	3.14159265358979	0.00000000000000
0.1	6.7	1.90546071796325	0.29222292648815	0.91201083935591	0.14996848355024	0.00000000000000	3.14159265358979	0.00000000000000
0.1	6.7	1.90546071796325	0.42798502294486	0.02466039337234	0.00000000000000	0.00000000000000	3.14159265358979	0.41636386063234
0.1	6.7	2.88403150312661	0.29222292648815	0.06081350012787	0.00000000000000	0.00000000000000	0.00000000000000	0.72403698437208
3.4	0.1	4.36515832240166	0.62682001739704	0.06081350012787	0.14996848355024	0.00000000000000	0.00000000000000	0.64238994491122
3.4	3.4	0.10000000000000	0.19952623149689	0.14996848355024	0.02466039337234	-0.22165681500328	3.14159265358979	0.75596936971053
3.4	6.7	1.25892541179417	0.24146664216652	0.91201083935591	0.91201083935591	0.00000000000000	3.14159265358979	0.00000000000000
3.4	10	1.90546071796325	0.62682001739704	0.02466039337234	0.06081350012787	-0.22165681500328	0.00000000000000	0.00000000000000
6.7	3.4	0.35481338923358	0.29222292648815	0.06081350012787	0.02466039337234	0.00000000000000	0.00000000000000	0.00488707023169
6.7	3.4	4.36515832240166	0.29222292648815	0.06081350012787	0.06081350012787	-0.22165681500328	3.14159265358979	0.67268960164690
6.7	3.4	6.60693448007596	0.35364818096244	0.06081350012787	0.91201083935591	0.00000000000000	3.14159265358979	0.00000000000000
6.7	6.7	1.25892541179417	0.62682001739704	0.14996848355024	0.00000000000000	0.00000000000000	3.14159265358979	0.00000000000000
6.7	6.7	1.90546071796325	0.24146664216652	0.91201083935591	0.36982817978027	-0.22165681500328	0.00000000000000	0.00000000000000
6.7	6.7	2.88403150312661	0.42798502294486	0.06081350012787	0.91201083935591	-0.22165681500328	3.14159265358979	0.00000000000000
10	10	2.88403150312661	0.35364818096244	0.00000000000000	0.02466039337234	-0.22165681500328	0.00000000000000	0.45969948922164

Note: The full version of Table 4.2 is available for download at http://dx.doi.org/10.5281/zenodo.6324216 [Bailey, 2022].
A random subset of rows are shown here for guidance regarding its form and content.

Table 4.2: Relative habitability results for a multidimensional set of giant planet parameters.

Visualization of a high-dimensional function like these results is unfortunately limited by the few spatial dimensions we have at our disposal. To summarize these results, we show the distribution of results across each parameter in Figure 4.7. We show the coplanar results on the left side of each violin plot and the inclined results on the right side, with different colors for the aligned and antialigned results. These results are flattened into one dimension; that is, each distribution includes all of the results for a given value of the designated parameter.

We note that the difference between the four combinations of inclination and pericenter alignment is very small. There appears to be some small increase in relative habitability

2. http://dx.doi.org/10.5281/zenodo.6324216

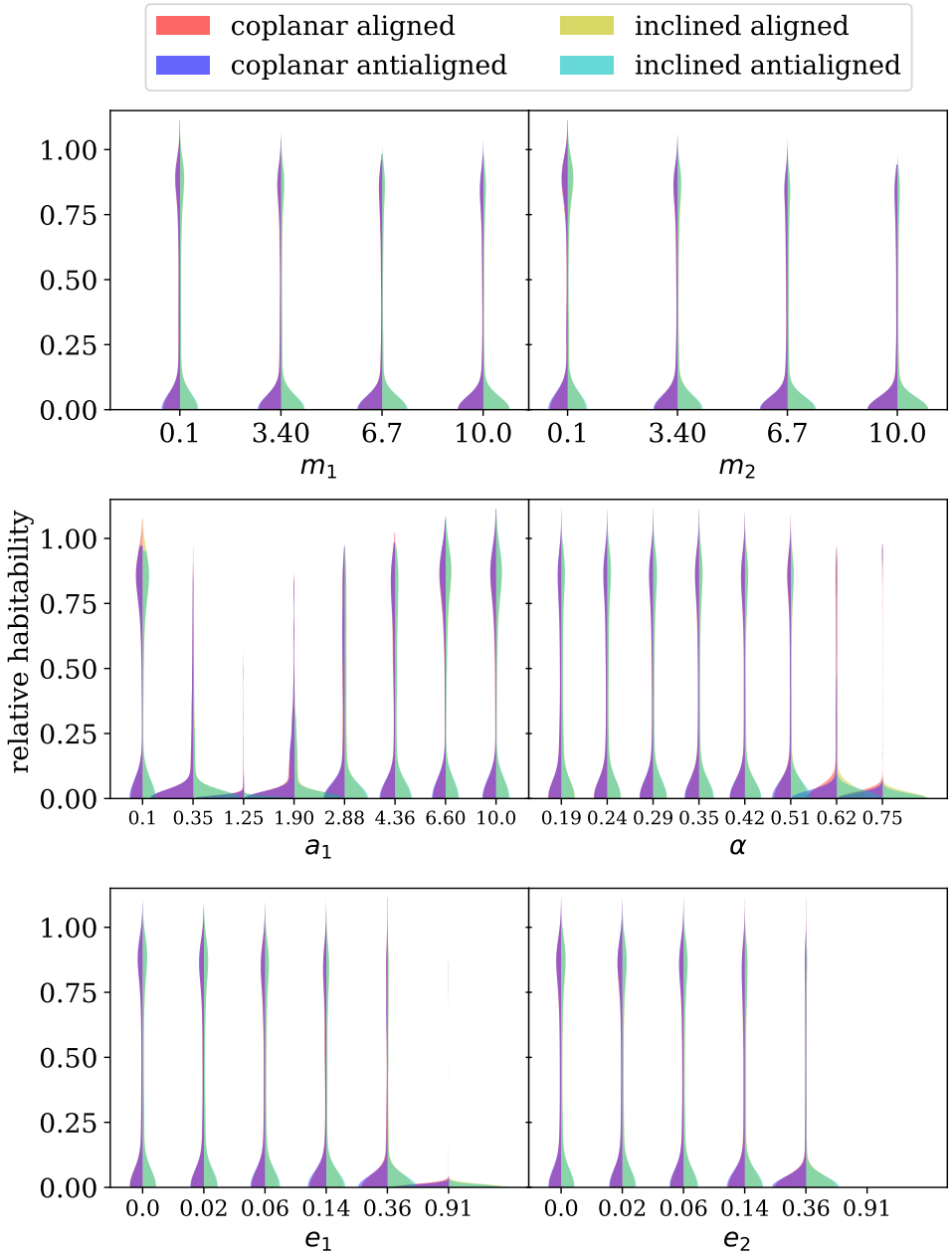

Figure 4.7: The distribution of relative habitability for each parameter. The coplanar results are on the left side of each violin plot and the inclined results on the right, with colors differentiating the aligned (red/yellow) and antialigned (blue/cyan) cases. Where the distributions overlap, the color appears purple or green. There is little visible difference between the four combinations at this level, though some small coloring variations are noted at low a_1 and high α.

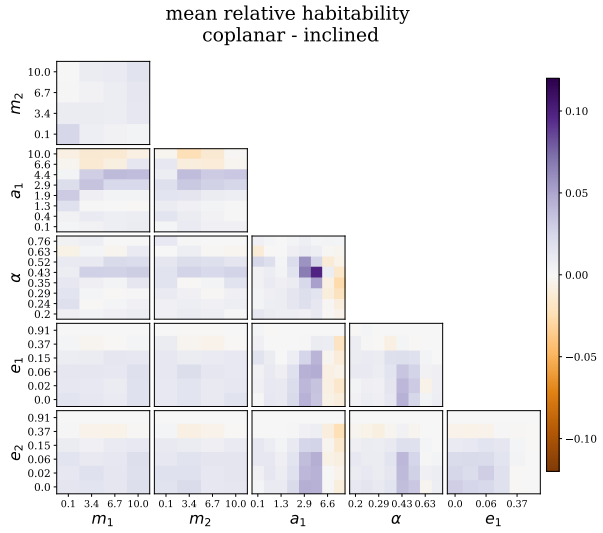

Figure 4.8: The difference in the mean relative habitability for inclined systems and coplanar systems. Purple indicates more relative habitability for the coplanar systems, while orange indicates more relative habitability for the inclined systems. The differences are mostly quite small; however, features stick out at high a_1 and at $\alpha = 0.43$.

for aligned systems over antialigned systems at very low a_1 and high α. To investigate these small differences, we use a 2D differential analysis. In Figures 4.8 and 4.9, we plot the difference in the mean relative habitability for the 2D distributions for different combinations of parameters. By using the mean, we are now flattening the relative habitability distribution into a single value, but we are reducing the flattening in parameter space by one dimension.

We've chosen to show here the comparison between the coplanar and inclined case for all systems and between the aligned and antialigned systems for all systems, as the alignment does not seem to have strong effect on the general inclination results nor vice versa.

Another interesting result we can take from our data is a distribution of all the maximum Earth eccentricities that are associated with systems with nonzero habitability probability. The histogram of these eccentricities is shown in Figure 4.10.

4.4.2 Discussion

General Trends in One Dimension

At the level of flattening in Figure 4.7, much detail is lost, but some trends can be observed. First, it is clear that the most common outcome is no relative habitability. In fact, almost

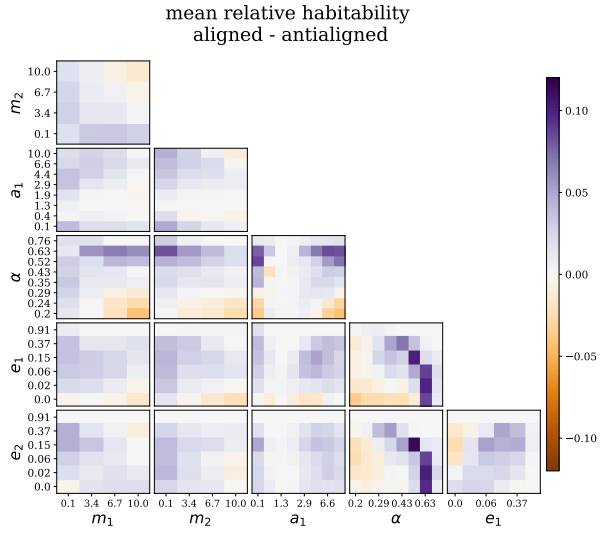

Figure 4.9: The difference in the mean relative habitability for aligned systems and antialigned systems. Purple indicates more relative habitability for the aligned systems, while orange indicates more relative habitability for the antialigned systems. The differences are mostly quite small; however, trends with α and $m_{1,2}$ and features at $e_{1,2} = 0.15$ stick out.

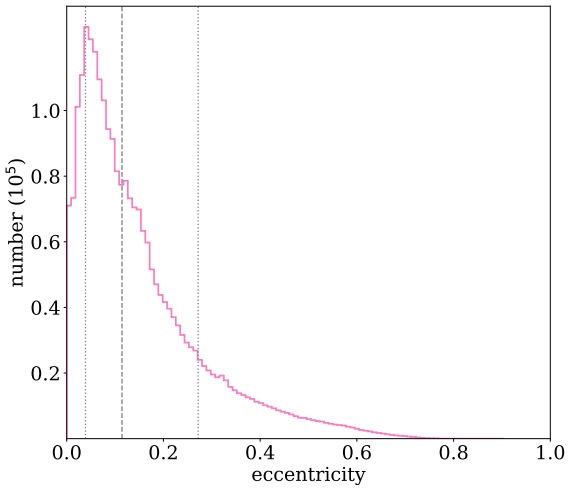

Figure 4.10: A histogram of the maximum Earth eccentricities for Earths with nonzero habitability probability. The median (0.114) and 15.9/84.1 percentiles (0.039/0.272) are indicated with vertical lines. The distribution contains two features: an excess of low-eccentricity planets and a long tail of moderately eccentric planets.

60% of the giant planet configurations have a relative habitability of zero. This is, in itself, not a noteworthy outcome, as the grid of parameter space was not chosen to necessarily be conducive to stable outcomes in every combination.

We note a trend of decreasing amounts of high relative habitability as the mass of the giant planets increase, with the greatest amount of relatively habitable systems occurring for the lowest m_2. For the locations of the giant planets, unsurprisingly when planet 1 is located in the HZ, relative habitability is extremely low. Also unsurprising is the reduction in relative habitability when the giant planets are close to one another at high α.

The trend in eccentricity is a decreasing amount systems with high relative habitability as eccentricity increases; however, this trend is less strong than the trend in mass of the giant planets. Instead, it decreases gently and then falls off a "cliff," past which there is almost no relative habitability. Indeed, for the case of $e_2 = 0.91$, there is not a single system with nonzero relative habitability. This is expected, as that high of an eccentricity causes orbit crossing even for the most widely separated giant planets.

Coplanar Versus Inclined Trends in Two Dimensions

The effect of mild inclinations rather than coplanar systems is quite small, with the difference in mean relative habitability always less than 0.12 and typically much less. We do note a few features in Figure 4.8.

In general, there is a slight preference for coplanar systems. However, this reverses for high a_1, where the inclined systems have higher mean relative habitability. This trend is strongest at middling masses, higher eccentricities, or middling α. The increase in relative habitability is because a small amount of inclination can excite mild eccentricities in the Earths, and increasing the eccentricities of the Earth can extend the outer edge of the HZ and increase the relative habitability. When the giant planets are further out, this effect falls in the range of Earth semi-major axes that have the potential for a large increase in relative

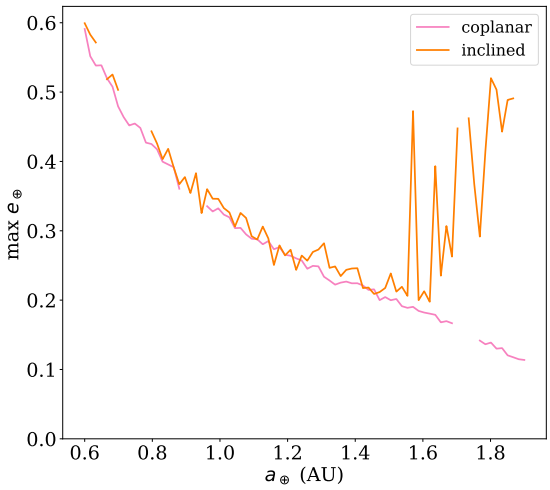

Figure 4.11: The maximum eccentricity of the Earths for two giant planet configurations. Systems with a stability outcome of zero are not plotted. Except for the inclination, the giant planet properties are the same in both configurations: $m_1 = m_2 = 10\ M_{Jup}$, $a_1 = 10$ AU, $\alpha = 0.354$, $e_1 = e_2 = 0.370$, $\Delta\varpi = 0$. The coplanar configuration has a relative habitability of 0.716; the inclined configuration has a relative habitability of 0.844. The mildly excited eccentricities in the outer regions of the HZ creates a notable trend at high a_1 on Figure 4.8.

habitability as eccentricity increases. Also, because the planets are more widely separated, the systems are more likely to be stable even with excited eccentricities. An example of this phenomenon is illustrated in Figure 4.11.

Additionally, we note a strong preference (0.098 difference) for coplanar systems at $\alpha = 0.43$ and $a_1 = 4.4$ AU. This difference is due to a large section of the center of the HZ that becomes unstable due to eccentricity excitation in the inclined systems but not in the coplanar systems. See Figure 4.12 for an illustration of this phenomenon. We note that the location of this excitation does not correspond with predicted secular resonances from Laplace-Lagrange theory (which are at 0.35 AU and 0.83 AU for eccentricity-pericenter and 0.95 AU for inclination-node) nor with any major mean-motion resonances lower than 5th order (6:1 between planet 1 and the Earth falls at 1.32 AU). It is possible that a higher-order secular resonance is at play; for example, the $[-1, 1]$ resonance where a test particle has $-f + g_1$ frequency would fall at 1.06 AU. However, the exact details of this feature are beyond the scope of this work.

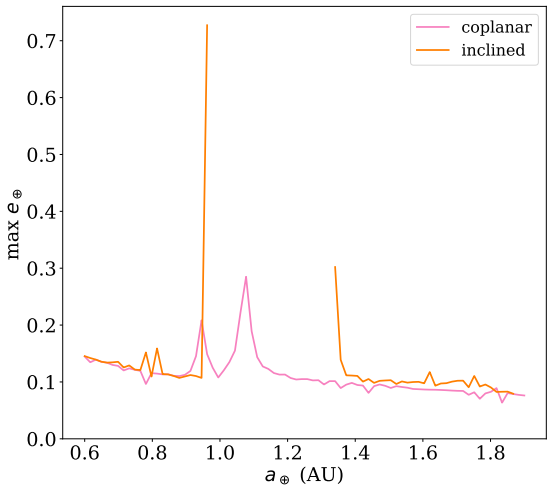

Figure 4.12: The maximum eccentricity of the Earths for two giant planet configurations. Systems with a stability outcome of zero are not plotted. Except for the inclination, the giant planet properties are the same in both configurations: $m_1 = 10\ M_{Jup}$, $m_2 = 3.4\ M_{Jup}$, $a_1 = 4.37$ AU, $\alpha = 0.428$, $e_1 = 0.025$, $e_2 = 0.061$, $\Delta\varpi = \pi$. The coplanar configuration has a relative habitability of 0.837; the inclined configuration has a relative habitability of 0.418. The destabilizing effect of the inclination creates a notable feature at this α/a_1 combination on Figure 4.8.

Aligned Versus Antialigned Trends in Two Dimensions

Similarly, the effect of the pericenter alignment is also quite small, though we note some features in Figure 4.9. There is a clear trend with α, where small α (more separated) shows a preference for antialigned systems while high α (more compact) shows a preference for aligned systems. This trend is clearer for higher masses of the giant planets. The likely explanation is simply that alignment of the pericenter can allow more tightly nested orbits.

There is also a small shift towards antialigned systems when the combined mass of the giant planets gets high. An example of this is illustrated in Figure 4.13, which shows the stability outcome and max Earth eccentricity for aligned and antialigned versions of a giant planet configuration. The instability zone for the aligned configuration extends further into the HZ. For similar systems with less combined mass in the giant planets, the opposite trend holds. Interestingly, the giant planets in the example in Figure 4.13 could be considered observable by direct imaging techniques [Traub and Oppenheimer, 2010], indicating that we can potentially make habitability inferences for such systems.

We note two strong areas of preference for coplanar systems when e_1 or e_2 is 0.15 and $\alpha = 0.52$. There seem to be several factors contributing to this trend. For example, in one

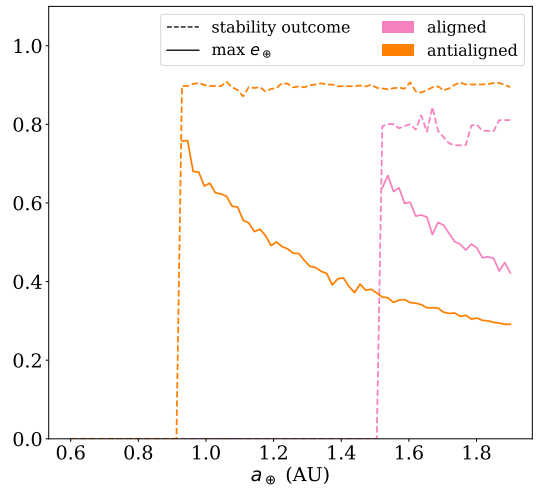

Figure 4.13: The stability outcome and maximum eccentricity of the Earths for two giant planet configurations. Eccentricities for systems with a stability outcome of zero are not plotted. Except for the alignment, the giant planet properties are the same in both configurations: $m_1 = m_2 = 10\ M_{Jup}$, $a_1 = 10$ AU, $\alpha = 0.241$, $e_1 = e_2 = 0.025$, $\Delta i = 0$. The aligned configuration has a relative habitability of 0.297; the antialigned configuration has a relative habitability of 0.752. This is opposite the trend for similar configurations with lower giant planet masses, giving rise to the shift in the m_1/m_2 panel in Figure 4.9.

configuration with $m_1 = 6.7\ M_{Jup}$, $m_2 = 0.1\ M_{Jup}$, $a_1 = 0.1$ AU, $\alpha = 0.518$, $e_1 = 0.061$, $e_2 = 0.150$, and $\Delta i = 0.222$, there are no unstable systems, but the aligned case simply has consistently higher stability outcomes predicted by `SPOCK`, leading to a relative habitability of 0.917 for the aligned system and 0.558 for the antialigned system. In another configuration with $m_1 = m_2 = 0.1\ M_{Jup}$, $a_1 = 4.365$ AU, $\alpha = 0.518$, $e_1 = 0.150$, $e_2 = 0.025$, and $\Delta i = 0$, there appear to be eccentricity resonances that excite the eccentricity of the Earth in approximately equal magnitude in both cases, but the one at approximately 1.8 AU results in instability for the antialigned case but not the aligned case, leading to a relative habitability of 1.023 for the aligned configuration and 0.839 for the antialigned configuration.

Eccentricity Distribution of Potentially Habitable Earths

Considering the maximum eccentricity distribution of the possibly-habitable Earths (Figure 4.10), we note two components of the distribution. The first is a large excess of low-eccentricity planets and the second is a long tail of moderately excited eccentricities. The low-eccentricity planets likely benefit from increased stability and a location well within the HZ, while some of the moderately eccentric planets are likely located exterior to the circular

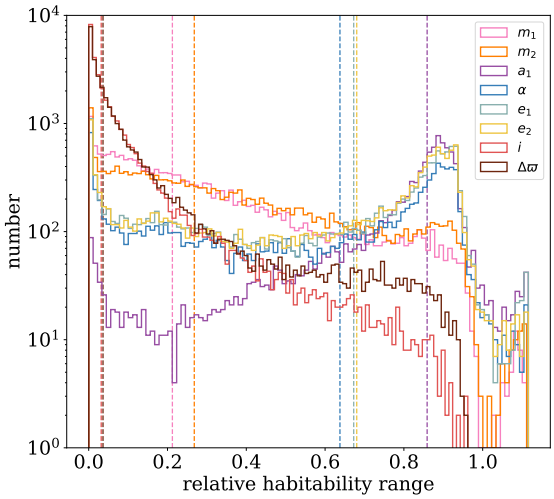

Figure 4.14: The distribution of nonzero relative habitability ranges for each parameter, calculated for every combination of the other parameters. The median values are indicated by a dashed vertical line.

HZ and receive a boost in potential habitability thanks to their excited eccentricities. However, too much eccentricity excitation can also lead to instability, so very high eccentricities are rarely encountered.

Parameter Sensitivity

One question we might hope to answer with this data: which of the varied parameters has the largest effect on the relative habitability of a system? The problem of analyzing a multidimensional function is a complex one, and here we apply a rather simple analysis to help us better understand the interplay between parameters.

For each parameter, we consider the function of relative habitability while each other parameter is held constant. From that one-dimensional function, we calculate the range of relative habitabilities (the maximum minus the minimum). This calculation is repeated for each possible combination of the other parameters. The distribution and median of these relative habitability ranges are shown in Figure 4.14 for each of the parameters. For visibility, we've considered only the nonzero ranges, but this does not qualitatively change the conclusion.

A higher range is associated with more change from that parameter, so we identify the parameters from most to least impactful based on their median values: a_1, e_2, e_1, α, m_2, m_1, $\Delta\varpi$, i.

The Most Habitable Configurations

There are a few systems that have relative habitabilities greater than one. This means that having giant planets in that configuration makes it *more* likely that an Earth analog could be habitable than a system with only the Earth analog. There are 253 such configurations. In Figure 4.15, the histograms for each parameter are shown. Each parameter started with a completely uniform distribution, but we see that there is a strong selection effect when looking at these ultra-habitable systems.

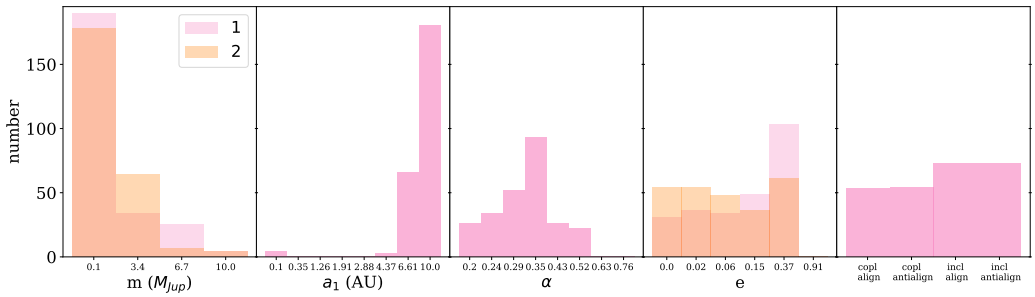

Figure 4.15: The distribution of systems with a relative habitability greater than one. The initial grid is uniform in each parameter; here, clear features are seen.

The mechanism that makes it possible for a configuration to have a relative habitability greater than one is eccentricity excitation of the Earth. Based on our habitability model, Earths that lie external to the circular HZ can become potentially habitable with excited eccentricity. If this effect is not offset by instability or the loss of the inner portion of the HZ (where excited eccentricity reduces the potential habitability), the configuration can have a relative habitability greater than one (i.e., considered more habitable than a system with an Earth as the only planet). Most of these effects were seen in our previous results, though

they become more distinct here.

First, it is clear that these systems tend to have lower masses in both giant planets. More massive planets likely induce additional instabilities that offset the gains in relative habitability from eccentricity excitation. Similarly, very compact (high α) configurations are not seen, and there is a clear preference for the middling $\alpha = 0.35$.

For the location of the giant planets, these ultra-habitable systems tend to be located further away from the HZ. This location preference is likely because more distant planets are less likely to destabilize the Earths while also being located to excite Earth eccentricities for planets located exterior to the HZ, where there is the most potential for increasing the habitability probability. This location preference also likely gives rise to the peak in the α distribution, as when $a_1 = 10$ AU, Laplace-Lagrange theory puts the secular resonance locations near the outer edge of the HZ for $\alpha = 0.35$ ($a_2 = 28.3$ AU). When $a_1 = 6.61$ AU, that shifts towards $\alpha = 0.43$ ($a_2 = 15.4$ AU), which also is represented in Figure 4.15.

For eccentricity, there are no highly eccentric systems, which is unsurprising as very few of these systems have any stable configurations at all. There is a marked difference in the eccentricity distributions between the two giant planets. For planet 2, the distribution is relatively uniform up to the stability cliff. For planet 1, there is a clear preference for moderate eccentricities. Again, this is likely the most efficient way to transfer eccentricity to the Earths (which all begin on circular orbits) without destabilizing the systems.

Lastly, there is almost no difference between the aligned or anti-aligned pericenters. There is a small but clear preference for inclined systems over coplanar ones; this preference makes sense given that even a small amount of inclination can lead to eccentricity excitation.

Although the details of these ultra-habitable parameters are influenced by our choice of habitability model, it seems likely that exterior giant companions can increase the size of the HZ around Sun-like stars, particularly when these giant companions are well-separated cold sub-Jupiters with moderate eccentricities and inclinations.

Giants in the Habitable Zone

One would expect that positioning a pair of giant planets right in the HZ would eliminate the possibility for habitable Earths. And while we do see a significant reduction of relative habitability for those configurations, it is not a complete gap. Our method precludes the possibility of Trojan Earths orbiting in a 1:1 resonance with the giant planets, as any orbit crossing is considered unstable, so though these types of planets may exist [Dvorak et al., 2004], they cannot explain the result here.

Let us consider the configurations where either giant planet falls between the most optimistic boundaries of the HZ, that is, between 0.75 AU and 1.77 AU. This is when $a_1 = 1.26$ AU, with any α, or when $a_1 = 0.35$ AU and $\alpha = 0.24$, 0.29, 0.35, or 0.43. Then we look at the configurations that have a relative habitability greater than 0.5, giving us a total of 292 configurations. In Figure 4.16, the histograms for each parameter are shown. Each parameter started with a completely uniform distribution (except for a_1/α as mentioned; their distributions are shown in black in Figure 4.16 for comparison), but we see clear trends when applying the relative habitability criterion.

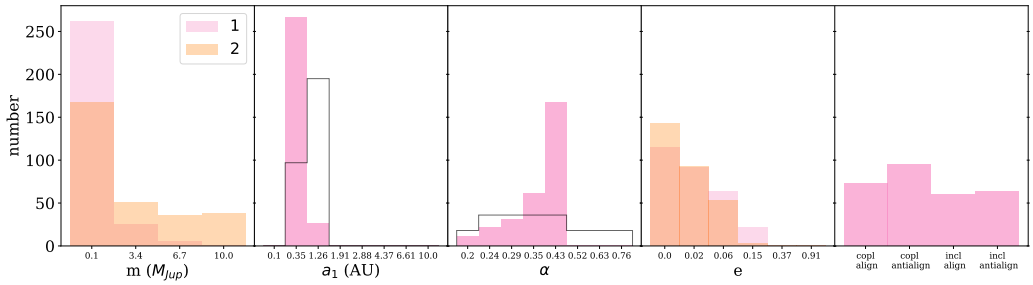

Figure 4.16: The distribution of systems with a relative habitability greater than 0.5 that overlap the circular HZ. The initial distribution of overlapping configurations (without applying the relative habitability criterion) is uniform in each parameter except for a_1/α, where they are shown in black for comparison. Clear features arise when considering the configurations with reasonable relative habitability.

We first note a strong preference for low m_1 but only a middling preference for low m_2. It is also far more likely that the relative habitability stays high when it is planet 2 that overlaps

the HZ rather than planet 1, despite the fact that these systems are outnumbered two to one in the sample of overlapping configurations. This is the case even for the overlapping a_2 closest to the overlapping a_1 (when $\alpha = 0.29$, $a_2 = 1.21$ AU). For example, the highest relative habitability is 0.86 when planet 2 is the overlapping planet (0.66 for $a_2 = 1.21$ AU) but only 0.55 when planet 1 is the overlapping planet. It is possible to have both planets overlapping the HZ when $a_1 = 1.26$ AU and $\alpha = 0.76$, but none of these systems have a relative habitability higher than 0.13.

There is a peak in the α distribution at $\alpha = 0.43$. When $a_1 = 0.35$ AU, that puts a_2 at 0.814 AU, just barely overlapping the inner edge of the HZ. As α decreases, planet 2 moves further into the HZ and decreases the number of configurations with high relative habitability.

Unsurprisingly, we see a strong preference for lower eccentricities, slightly more marked for e_2. Given that planet 2 is closer to the HZ and the compact nature of these systems, large amounts of eccentricity can quickly cause instability.

Lastly, we see a slight preference for the coplanar and antialigned configurations. Coplanarity preference is expected, as even a small amount of inclination can provide some additional instability, but the preference for anti-alignment is somewhat unexpected, as these compact systems would see stability benefits from an aligned orientation. However, given that most systems have very small eccentricities, the pericenter orientation becomes less important, so it is possible that this feature is insignificant. Assuming $\sqrt{(}N)$ error, the difference between aligned (133) and anti-aligned (159) is $\sim 1.5\sigma$ discrepant.

From these results, we can conclude that the HZ is wide enough to accommodate both a habitable Earth and a giant planet, though likely not two giant planets. These systems are more possible with smaller giant planets, particularly the inner giant planet, and with low eccentricities.

We do note here that this discussion does not include the likelihood of forming such a

system in the first place. Giant planets have a strong influence on the formation of terrestrial planets [Morbidelli et al., 2012, Childs et al., 2019]. Effects from the in situ formation of giants in or near the HZ or from their migration to that location could limit the possibility of forming or migrating Earths into the HZ [Raymond et al., 2006, Darriba et al., 2017]; inclusion of these effects are left for another study.

4.4.3 Future Work

This chapter puts forth a process for evaluating system architectures for habitability and creates a rich initial dataset for examining the impact of giant companions on the habitability of an Earth. There are many important steps that could be taken to iterate and improve upon what is presented here.

We've seen that dynamical interactions with giant planets can affect the eccentricity of an Earth analog and therefore its potential habitability. Similarly, the system architecture can affect the obliquity of Earth-like planets, which also strongly influences the climate [Linsenmeier et al., 2015, Kane and Torres, 2017].

We use a very simplified and discontinuous habitability model. More accurate habitability zone limits taking into account additional 1-D and 3-D climate model results could improve this model; multiple models could even be used to compare and contrast. The habitability model could even incorporate more statistical methods to better match our current knowledge of the HZ [Zsom, 2015, Méndez et al., 2021].

We consider only exactly Earth-like planets, ignoring possible effects of terrestrial planet mass, rotation rate, magnetic field, density, and composition, all of which have enormous implications for climate and habitability [Yang et al., 2014, Meadows and Barnes, 2018].

We consider only Sun-like stars. The HZ varies significantly around different stellar types, due to differences in temperature and spectrum [Kopparapu et al., 2013], and many dynamical effects scale with the planet-star mass ratio. Additionally, a large portion of stars

are found in binaries, which can effect habitability for both circumstellar and circumbinary planets [Cuntz, 2014, Georgakarakos et al., 2021]. Stars also change in luminosity over time, which can affect the location of the HZ [Baraffe et al., 2015].

We achieve only mild resolution in each parameter considered, likely missing narrow features in our multidimensional grid, as we see such features arise in our fiducial system. More computational time is required to achieve better resolution.

We neglect the dynamical histories of the systems and constraints from formation. It is likely that many systems with giant planets undergo instabilities [Jurić and Tremaine, 2008], which could affect both the formation of terrestrial planets and the stability of those planets, depending on the timescales of instability and formation. Furthermore, we consider any instability within the system to preclude habitability, which may not necessarily be the case [Kokaia et al., 2020]. Some of our giant planet configurations may not be compatible with the formation of terrestrial planets or may be difficult to explain in and of themselves (e.g. systems with $e_1 = 0.91$ and $e_2 = 0$). We also do not consider the possibility of overlapping but stable orbits, such as Pluto and Neptune have in the solar system, nor of co-orbital planets. Neither do we include tidal effects or circularization, which could be significant for some of our planets [Eggleton et al., 1998].

We also do not consider multiple terrestrial planets. Multiple terrestrial planets might lead to additional instability due to interactions with one another, or they may in fact stabilize one another, such as the Venus-Earth interaction in our solar system that displaces Venus's eccentricity from a secular resonance [Innanen et al., 1998].

4.5 Conclusion

Determining the habitability of an exoplanet requires taking into account the interplay of a large number of complex and interdisciplinary factors, many of which are not yet well understood. In this chapter, we investigated one aspect of habitability external to the planet itself:

the configuration of its giant companions. The system architecture relates to habitability via the destabilization of planets in the habitable zone as well as the excitation of those planets' eccentricities.

From our one-dimensional analysis of two fiducial systems (one exterior and one interior), we saw that the giant planets can have very large and sharp effects as they get close to one another or to the HZ and when their eccentricities are high. When the giants are exterior to the HZ, Kozai-Lidov cycles can destabilize Earths in the HZ for highly mutually inclined systems. Resonances can provide islands of protection at high eccentricities. More mild effects arise as the location of secular resonances shift throughout the system, such as a dependence on the mass ratio of the giant planets.

We undertook a truly multidimensional investigation of system architectures and determined that the presence of giant companions usually decreases the relative habitability of a system compared to the presence of an Earth-like planet alone. This is particularly true when the giant planets are very massive, close to the habitable zone, tightly spaced, and highly eccentric, though exceptions exist, such as the coexistence of giant and Earth-like planets within the HZ. However, the giant planets can sometimes *increase* the relative habitability of a system by providing mild eccentricity excitation that extends the outer edge of the HZ, usually when the giant companions are on wide, mildly eccentric, and inclined orbits.

From our results, we see that the location of the inner giant planet has the most effect on the relative habitability of a system, followed by several parameters of similar strength with the outer giant planet's eccentricity, the inner giant planet's eccentricity, and the semi-major axis ratio of the giant planets, while the mass of the outer giant planet and then the mass of the inner giant planet have the least effect of the main six parameters, aside from alignment and inclination which are not well-sampled.

There are many avenues to build upon the work presented here. Even so, we have created a rich dataset, and our results illuminate several of the many possible effects of the system

architecture on the habitability of exoplanets.

4.6 Appendix

4.6.1 Stability Outcome Results

We include here Table 4.3 with the complete results for each three-planet system (each giant planet configuration and its associated 80 Earth locations). We applied our habitability model (Section 4.2.4) to these results to determine our relative habitability results (Table 4.2); we include these intermediate results to allow for the potential application of different habitable models or for context in understanding the results in Table 4.2. The "outcome codes" in Table 4.3 refer to which step of the process outlined in Section 4.2.2 resulted in an outcome of zero:

- 2: 2 giant planets fail analytical stability criterion
- o: orbit crossing is predicted by Laplace-Lagrange theory
- z: zero stability predicted by `SPOCK`
- u: unstable during the 5×10^6-orbit integration
- h: high spectral fraction predicts instability

m_1 (M_{Jup})	m_2 (M_{Jup})	a_1 (AU)	α	e_1	e_2	Δi (rad)	$\Delta\varpi$ (rad)	$a_\oplus$ (AU)	Outcome Code	Outcome	Max $e_\oplus$
6.7	10	10.000000000000000	0.427985022944864	0.149968483550237	0.369828179780266	0.000000000000000	0.000000000000000	1.554430379746840	z	0.000000000000000	0.000000000000000
0.1	10	1.258925411794170	0.241466642166516	0.024660393372343	0.912010839355910	0.221656815003280	3.141592653589790	1.208860759493670	2	0.000000000000000	0.000000000000000
6.7	0.1	10.000000000000000	0.427985022944864	0.024660393372343	0.000000000000000	0.000000000000000	3.141592653589790	1.669620253164560		0.926216959953308	0.100342776605637
10	10	1.905460717963250	0.292222926488148	0.000000000000000	0.369828179780266	0.000000000000000	0.000000000000000	1.455696202531650	o	0.000000000000000	0.000000000000000
6.7	3.4	4.365158322401660	0.758577575029184	0.912010839355910	0.912010839355910	0.221656815003280	3.141592653589790	1.636708860759490	z	0.000000000000000	0.000000000000000
10	0.1	0.354813389233575	0.241466642166516	0.149968483550237	0.060813500127872	0.000000000000000	0.000000000000000	1.801265822784810	z	0.000000000000000	0.000000000000000
10	6.7	1.905460717963250	0.427985022944864	0.912010839355910	0.369828179780266	0.221656815003280	3.141592653589790	0.978481012658228	2	0.000000000000000	0.000000000000000
0.1	10	2.884031503126610	0.517947467923121	0.060813500127872	0.000000000000000	0.221656815003280	3.141592653589790	1.521518987341770		0.567690968513489	0.147312329046831
0.1	10	2.884031503126610	0.241466642166516	0.912010839355910	0.369828179780266	0.000000000000000	3.141592653589790	1.554430379746840	2	0.000000000000000	0.000000000000000
0.1	3.4	2.884031503126610	0.241466642166516	0.369828179780266	0.912010839355910	0.000000000000000	3.141592653589790	1.143037974683540	o	0.000000000000000	0.000000000000000
3.4	0.1	10.000000000000000	0.292222926488148	0.149968483550237	0.024660393372343	0.000000000000000	3.141592653589790	1.175949367088610		0.935216546058655	0.109784552928324
0.1	10	10.000000000000000	0.199526231496888	0.024660393372343	0.000000000000000	0.000000000000000	0.000000000000000	1.406329113924050		0.904384553432465	0.092353750797595
0.1	3.4	6.606934480075960	0.758577575029184	0.060813500127872	0.149968483550237	0.221656815003280	3.141592653589790	0.797468354430380	2	0.000000000000000	0.000000000000000
0.1	6.7	10.000000000000000	0.241466642166516	0.149968483550237	0.060813500127872	0.221656815003280	3.141592653589790	1.686075949367090		0.878525078296661	0.124453378884910
10	10	4.365158322401660	0.199526231496888	0.369828179780266	0.024660393372343	0.221656815003280	3.141592653589790	1.784810126582280	z	0.000000000000000	0.000000000000000
0.1	3.4	1.258925411794170	0.241466642166516	0.000000000000000	0.912010839355910	0.000000000000000	3.141592653589790	1.406329113924050	z	0.000000000000000	0.000000000000000
6.7	6.7	10.000000000000000	0.353648180962444	0.000000000000000	0.369828179780266	0.221656815003280	3.141592653589790	1.472151898734180	u	0.000000000000000	0.000000000000000
10	10	0.354813389233575	0.517947467923121	0.024660393372343	0.000000000000000	0.000000000000000	3.141592653589790	1.241772151898730	u	0.000000000000000	0.000000000000000
6.7	6.7	4.365158322401660	0.626820017397041	0.912010839355910	0.024660393372343	0.000000000000000	0.000000000000000	0.781012658227848	2	0.000000000000000	0.000000000000000
3.4	10	1.905460717963250	0.427985022944864	0.149968483550237	0.912010839355910	0.000000000000000	0.000000000000000	1.274683544303800	o	0.000000000000000	0.000000000000000

Note: The full version of Table 4.3 is available for download at http://dx.doi.org/10.5281/zenodo.6324216 [Bailey, 2022].
A random subset of rows are shown here for guidance regarding its form and content.

Table 4.3: Stability results for a multidimensional set of giant planet parameters and Earth locations. See the text for details on the outcome codes.

CHAPTER 5

IN CLOSING

In this thesis, I built upon the centuries of work in celestial mechanics to use numerical and analytical methods to investigate the dynamics of multiplanetary systems.

Analytical methods have the advantage of being faster as well as having clearer dependence on the physical parameters of the system, but all analytical methods are approximations and can suffer sometimes untenable amounts of error.

Numerical methods, while still not perfect in accuracy via both inherent computational limitations and simplifications based on the choice of what physics to include or not, can provide much more accurate information about multiplanet systems at the cost of computation time and resources. Until the existence of solar-system-sized laboratories, numerical methods are as close as we can get to running experiments on multiplanet systems. Like all experiments, the results can be sometimes surprising and unexpected. These make for exciting results, revealing some possible new understanding of the universe, but they can be sometimes difficult to explain without the explicit dependence of analytical solutions.

From this work, many future studies could sprout. Examining potential inclination-node secular resonances on a population level might perhaps unveil evidence for a substantial number of misaligned planets. As more data becomes available, the period ratio distribution might yield more insights and more limits on the properties of exoplanet populations, perhaps by studying even higher-order resonances. More refined habitability models with more parameter combinations could shed insight on the relative habitability of multiplanet systems and where we might hope to find highly-habitable Earth-like planets.

While the study of planetary dynamics has a long and illustrious history, the field of exoplanets is still a young one. There is much left to discover about the intricate dance of planets, a question that is particularly intriguing in regards to Earth and how and why life came to be on our planet—and how that might be replicated in other systems. We must

connect a disparate set of circumstances from the formation of star(s) and protoplanetary disk to early system interactions and long-term evolution and ultimately the post-main-sequence fate of planets; also, we must contend with a range of sizes from dust grains to brown dwarfs and everything in between. Further, given the limitations of causality as we know them, we must contend with our inability to observe exoplanet systems as intimately as our own and find ways to connect observable systems with our theoretical understanding.

No planetary system exists frozen in time nor free from the effects of gravity. We cannot have true understanding of exoplanets without understanding the dynamics and planet-planet interactions.

REFERENCES

Matthew T. Agnew, Sarah T. Maddison, and Jonathan Horner. Prospecting for exo-Earths in multiple planet systems with a gas giant. *MNRAS*, 481(4):4680–4697, December 2018. doi: 10.1093/mnras/sty2509.

Matthew T. Agnew, Sarah T. Maddison, Jonathan Horner, and Stephen R. Kane. Predicting multiple planet stability and habitable zone companions in the TESS era. *MNRAS*, 485 (4):4703–4725, June 2019. doi: 10.1093/mnras/stz345.

J. M. Almenara, R. F. Díaz, R. Mardling, S. C. C. Barros, C. Damiani, G. Bruno, X. Bonfils, and M. Deleuil. Absolute masses and radii determination in multiplanetary systems without stellar models. *MNRAS*, 453(3):2644–2652, Nov 2015. doi: 10.1093/mnras/stv1735.

Kassandra R. Anderson and Dong Lai. Moderately eccentric warm Jupiters from secular interactions with exterior companions. *MNRAS*, 472(3):3692–3705, December 2017. doi: 10.1093/mnras/stx2250.

Fabio Antonini, Adrian S. Hamers, and Yoram Lithwick. Dynamical Constraints on the Origin of Hot and Warm Jupiters with Close Friends. *AJ*, 152(6):174, December 2016. doi: 10.3847/0004-6256/152/6/174.

Stanley E. Babb. Accuracy of planetary theories, particularly for mars. *Isis*, 68(3):426–434, 1977. ISSN 00211753, 15456994. URL `http://www.jstor.org/stable/231318`.

Nanna Bach-Møller and Uffe G. Jørgensen. Orbital eccentricity-multiplicity correlation for planetary systems and comparison to the Solar system. *MNRAS*, 500(1):1313–1322, January 2021. doi: 10.1093/mnras/staa3321.

Nora Bailey. Datasets for dynamical habitability of an earthlike planet with two giant companions, June 2022. URL `http://dx.doi.org/10.5281/zenodo.6324216`.

Nora Bailey and Daniel Fabrycky. Nodal Precession in Closely Spaced Planet Pairs. *The Astronomical Journal*, 159(5):217, May 2020. doi: 10.3847/1538-3881/ab83f0.

Nora Bailey and Daniel Fabrycky. Relative Habitability of Exoplanet Systems with Two Giant Planets. *MNRAS*, 2022.

Nora Bailey, Gregory Gilbert, and Daniel Fabrycky. Period Ratio Sculpting near Second-order Mean-motion Resonances. *The Astronomical Journal*, 163(1):13, January 2022. doi: 10.3847/1538-3881/ac2f46.

Isabelle Baraffe, Derek Homeier, France Allard, and Gilles Chabrier. New evolutionary models for pre-main sequence and main sequence low-mass stars down to the hydrogen-burning limit. *A&A*, 577:A42, May 2015. doi: 10.1051/0004-6361/201425481.

Rory Barnes, Russell Deitrick, Richard Greenberg, Thomas R. Quinn, and Sean N. Raymond. Long-lived Chaotic Orbital Evolution of Exoplanets in Mean Motion Resonances with Mutual Inclinations. *ApJ*, 801(2):101, March 2015. doi: 10.1088/0004-637X/801/2/101.

Konstantin Batygin, Peter H. Bodenheimer, and Gregory P. Laughlin. In Situ Formation and Dynamical Evolution of Hot Jupiter Systems. *ApJ*, 829(2):114, October 2016. doi: 10.3847/0004-637X/829/2/114.

Ákos Bazsó, Elke Pilat-Lohinger, Siegfried Eggl, Barbara Funk, David Bancelin, and Gioia Rau. Dynamics and habitability in circumstellar planetary systems of known binary stars. *MNRAS*, 466(2):1555–1566, April 2017. doi: 10.1093/mnras/stw3095.

Travis A. Berger, Daniel Huber, Jennifer L. van Saders, Eric Gaidos, Jamie Tayar, and Adam L. Kraus. The Gaia-Kepler Stellar Properties Catalog. I. Homogeneous Fundamental Properties for 186,301 Kepler Stars. *AJ*, 159(6):280, June 2020. doi: 10.3847/1538-3881/159/6/280.

Emeline Bolmont, Anne-Sophie Libert, Jeremy Leconte, and Franck Selsis. Habitability of planets on eccentric orbits: Limits of the mean flux approximation. *A&A*, 591:A106, June 2016. doi: 10.1051/0004-6361/201628073.

William J. Borucki, David Koch, Gibor Basri, Natalie Batalha, Timothy Brown, Douglas Caldwell, John Caldwell, Jørgen Christensen-Dalsgaard, William D. Cochran, Edna DeVore, Edward W. Dunham, Andrea K. Dupree, Thomas N. Gautier, John C. Geary, Ronald Gilliland, Alan Gould, Steve B. Howell, Jon M. Jenkins, Yoji Kondo, David W. Latham, Geoffrey W. Marcy, Søren Meibom, Hans Kjeldsen, Jack J. Lissauer, David G. Monet, David Morrison, Dimitar Sasselov, Jill Tarter, Alan Boss, Don Brownlee, Toby Owen, Derek Buzasi, David Charbonneau, Laurance Doyle, Jonathan Fortney, Eric B. Ford, Matthew J. Holman, Sara Seager, Jason H. Steffen, William F. Welsh, Jason Rowe, Howard Anderson, Lars Buchhave, David Ciardi, Lucianne Walkowicz, William Sherry, Elliott Horch, Howard Isaacson, Mark E. Everett, Debra Fischer, Guillermo Torres, John Asher Johnson, Michael Endl, Phillip MacQueen, Stephen T. Bryson, Jessie Dotson, Michael Haas, Jeffrey Kolodziejczak, Jeffrey Van Cleve, Hema Chandrasekaran, Joseph D. Twicken, Elisa V. Quintana, Bruce D. Clarke, Christopher Allen, Jie Li, Haley Wu, Peter Tenenbaum, Ekaterina Verner, Frederick Bruhweiler, Jason Barnes, and Andrej Prsa. Kepler Planet-Detection Mission: Introduction and First Results. *Science*, 327 (5968):977, February 2010. doi: 10.1126/science.1185402.

G. Boué, J. Laskar, and F. Farago. A simple model of the chaotic eccentricity of Mercury. *A&A*, 548:A43, December 2012. doi: 10.1051/0004-6361/201219991.

Gwenaël Boué and Daniel C. Fabrycky. Compact Planetary Systems Perturbed by an Inclined Companion. I. Vectorial Representation of the Secular Model. *ApJ*, 789(2):110, July 2014. doi: 10.1088/0004-637X/789/2/110.

Dirk Brouwer. On the accumulation of errors in numerical integration. *AJ*, 46:149–153, October 1937. doi: 10.1086/105423.

G. Bruno, J. M. Almenara, S. C. C. Barros, A. Santerne, R. F. Diaz, M. Deleuil, C. Damiani, A. S. Bonomo, I. Boisse, F. Bouchy, G. Hébrard, and G. Montagnier. SOPHIE velocimetry of Kepler transit candidates. XIV. A joint photometric, spectroscopic, and dynamical analysis of the Kepler-117 system. *A&A*, 573:A124, Jan 2015. doi: 10.1051/0004-6361/201424591.

Christopher J. Burke. Impact of Orbital Eccentricity on the Detection of Transiting Extrasolar Planets. *ApJ*, 679(2):1566–1573, June 2008. doi: 10.1086/587798.

J. E. Chambers, G. W. Wetherill, and A. P. Boss. The Stability of Multi-Planet Systems. *Icarus*, 119(2):261–268, February 1996. doi: 10.1006/icar.1996.0019.

Sourav Chatterjee, Eric B. Ford, Soko Matsumura, and Frederic A. Rasio. Dynamical Outcomes of Planet-Planet Scattering. *ApJ*, 686(1):580–602, October 2008. doi: 10.1086/590227.

Jingjing Chen and David Kipping. Probabilistic Forecasting of the Masses and Radii of Other Worlds. *ApJ*, 834(1):17, January 2017. doi: 10.3847/1538-4357/834/1/17.

Anna C. Childs, Elisa Quintana, Thomas Barclay, and Jason H. Steffen. Giant planet effects on terrestrial planet formation and system architecture. *MNRAS*, 485(1):541–549, May 2019. doi: 10.1093/mnras/stz385.

William D. Cochran, Daniel C. Fabrycky, Guillermo Torres, François Fressin, Jean-Michel Désert, Darin Ragozzine, Dimitar Sasselov, Jonathan J. Fortney, Jason F. Rowe, and Erik J. Brugamyer. Kepler-18b, c, and d: A System of Three Planets Confirmed by Transit Timing Variations, Light Curve Validation, Warm-Spitzer Photometry, and Radial Velocity Measurements. *ApJS*, 197(1):7, Nov 2011. doi: 10.1088/0067-0049/197/1/7.

Miles Cranmer, Daniel Tamayo, Hanno Rein, Peter Battaglia, Samuel Hadden, Philip J. Armitage, Shirley Ho, and David N. Spergel. A Bayesian neural network predicts the dissolution of compact planetary systems. *arXiv e-prints*, art. arXiv:2101.04117, January 2021.

M. Cuntz. S-type and P-type Habitability in Stellar Binary Systems: A Comprehensive Approach. I. Method and Applications. *ApJ*, 780(1):14, January 2014. doi: 10.1088/0004-637X/780/1/14.

C. Damiani and A. F. Lanza. Prospecting transit duration variations in extrasolar planetary systems. *A&A*, 535:A116, Nov 2011. doi: 10.1051/0004-6361/201117207.

L. A. Darriba, G. C. de Elía, O. M. Guilera, and A. Brunini. Migrating Jupiter up to the habitable zone: Earth-like planet formation and water delivery. *A&A*, 607:A63, November 2017. doi: 10.1051/0004-6361/201630185.

Robert J. De Rosa, Rebekah Dawson, and Eric L. Nielsen. A significant mutual inclination between the planets within the π Mensae system. *A&A*, 640:A73, August 2020. doi: 10.1051/0004-6361/202038496.

Katherine M. Deck and Eric Agol. Measurement of Planet Masses with Transit Timing Variations Due to Synodic "Chopping" Effects. *ApJ*, 802(2):116, April 2015. doi: 10.1088/0004-637X/802/2/116.

Katherine M. Deck and Eric Agol. Transit Timing Variations for Planets near Eccentricity-type Mean Motion Resonances. *ApJ*, 821(2):96, April 2016. doi: 10.3847/0004-637X/821/2/96.

Katherine M. Deck, Matthew Payne, and Matthew J. Holman. First-order Resonance Overlap and the Stability of Close Two-planet Systems. *ApJ*, 774(2):129, September 2013. doi: 10.1088/0004-637X/774/2/129.

J. B. Delisle, J. Laskar, and A. C. M. Correia. Resonance breaking due to dissipation in planar planetary systems. *A&A*, 566:A137, June 2014. doi: 10.1051/0004-6361/201423676.

Paul Denham, Smadar Naoz, Bao-Minh Hoang, Alexander P. Stephan, and Will M. Farr. Hidden planetary friends: on the stability of two-planet systems in the presence of a distant, inclined companion. *MNRAS*, 482(3):4146–4154, January 2019. doi: 10.1093/mnras/sty2830.

Courtney D. Dressing, David S. Spiegel, Caleb A. Scharf, Kristen Menou, and Sean N. Raymond. Habitable Climates: The Influence of Eccentricity. *ApJ*, 721(2):1295–1307, October 2010. doi: 10.1088/0004-637X/721/2/1295.

R. Dvorak, E. Pilat-Lohinger, R. Schwarz, and F. Freistetter. Extrasolar Trojan planets close to habitable zones. *A&A*, 426:L37–L40, November 2004. doi: 10.1051/0004-6361:200400075.

H.J. Easterling. Homocentric spheres in de caelo. *Phronesis*, 6(1-2):138 – 153, 1961. doi: https://doi.org/10.1163/156852861X00161. URL `https://brill.com/view/journals/phro/6/1-2/article-p138_16.xml`.

Peter P. Eggleton, Ludmila G. Kiseleva, and Piet Hut. The Equilibrium Tide Model for Tidal Friction. *ApJ*, 499(2):853–870, May 1998. doi: 10.1086/305670.

A. Einstein. Die Grundlage der allgemeinen Relativitätstheorie. *Annalen der Physik*, 354:769–822, 1916. doi: 10.1002/andp.19163540702.

A. Einstein and R. W. Lawson. *Relativity: the special and general theory.* Holt, New York, 1921.

Néstor Espinoza. Efficient Joint Sampling of Impact Parameters and Transit Depths in Transiting Exoplanet Light Curves. *Research Notes of the American Astronomical Society*, 2(4):209, November 2018. doi: 10.3847/2515-5172/aaef38.

Daniel C. Fabrycky, Jack J. Lissauer, Darin Ragozzine, Jason F. Rowe, Jason H. Steffen, Eric Agol, Thomas Barclay, Natalie Batalha, William Borucki, David R. Ciardi, Eric B. Ford,

Thomas N. Gautier, John C. Geary, Matthew J. Holman, Jon M. Jenkins, Jie Li, Robert C. Morehead, Robert L. Morris, Avi Shporer, Jeffrey C. Smith, Martin Still, and Jeffrey Van Cleve. Architecture of Kepler's Multi-transiting Systems. II. New Investigations with Twice as Many Candidates. *ApJ*, 790(2):146, Aug 2014. doi: 10.1088/0004-637X/790/2/146.

Eric B. Ford, Samuel N. Quinn, and Dimitri Veras. Characterizing the Orbital Eccentricities of Transiting Extrasolar Planets with Photometric Observations. *ApJ*, 678(2):1407–1418, May 2008. doi: 10.1086/587046.

Daniel Foreman-Mackey, David W. Hogg, Dustin Lang, and Jonathan Goodman. emcee: The MCMC Hammer. *PASP*, 125(925):306, March 2013. doi: 10.1086/670067.

Daniel Foreman-Mackey, Eric Agol, Sivaram Ambikasaran, and Ruth Angus. Fast and Scalable Gaussian Process Modeling with Applications to Astronomical Time Series. *AJ*, 154(6):220, December 2017. doi: 10.3847/1538-3881/aa9332.

A. Fortier, Y. Alibert, F. Carron, W. Benz, and K. M. Dittkrist. Planet formation models: the interplay with the planetesimal disc. *A&A*, 549:A44, January 2013. doi: 10.1051/0004-6361/201220241.

Benjamin J. Fulton, Erik A. Petigura, Andrew W. Howard, Howard Isaacson, Geoffrey W. Marcy, Phillip A. Cargile, Leslie Hebb, Lauren M. Weiss, John Asher Johnson, Timothy D. Morton, Evan Sinukoff, Ian J. M. Crossfield, and Lea A. Hirsch. The California-Kepler Survey. III. A Gap in the Radius Distribution of Small Planets. *AJ*, 154(3):109, September 2017. doi: 10.3847/1538-3881/aa80eb.

J. G. Galle. Account of the discovery of Le Verrier's planet Neptune, at Berlin, Sept. 23, 1846. *MNRAS*, 7:153, November 1846. doi: 10.1093/mnras/7.9.153.

Carlos Gascón, Dmitry Savransky, and Miquel Sureda. Analytic Stability Maps of Unknown Exoplanet Companions for Imaging Prioritization. *AJ*, 160(2):84, August 2020. doi: 10.3847/1538-3881/ab9b21.

Nikolaos Georgakarakos, Siegfried Eggl, and Ian Dobbs-Dixon. Circumbinary habitable zones in the presence of a giant planet. *Frontiers in Astronomy and Space Sciences*, 8:44, April 2021. doi: 10.3389/fspas.2021.640830.

Gregory J. Gilbert and Daniel C. Fabrycky. An Information Theoretic Framework for Classifying Exoplanetary System Architectures. *AJ*, 159(6):281, June 2020. doi: 10.3847/1538-3881/ab8e3c.

Peter Goldreich and Steven Soter. Q in the Solar System. *Icarus*, 5(1):375–389, January 1966. doi: 10.1016/0019-1035(66)90051-0.

K. Goździewski, C. Migaszewski, F. Panichi, and E. Szuszkiewicz. The Laplace resonance in the Kepler-60 planetary system. *MNRAS*, 455(1):L104–L108, January 2016. doi: 10.1093/mnrasl/slv156.

Sam Hadden. An Integrable Model for the Dynamics of Planetary Mean-motion Resonances. *AJ*, 158(6):238, December 2019. doi: 10.3847/1538-3881/ab5287.

Sam Hadden and Yoram Lithwick. Densities and Eccentricities of 139 Kepler Planets from Transit Time Variations. *ApJ*, 787(1):80, May 2014. doi: 10.1088/0004-637X/787/1/80.

Sam Hadden and Yoram Lithwick. Kepler Planet Masses and Eccentricities from TTV Analysis. *AJ*, 154(1):5, July 2017. doi: 10.3847/1538-3881/aa71ef.

Sam Hadden and Yoram Lithwick. A Criterion for the Onset of Chaos in Systems of Two Eccentric Planets. *AJ*, 156(3):95, September 2018. doi: 10.3847/1538-3881/aad32c.

Nader Haghighipour and Othon C. Winter. Formation of terrestrial planets in disks with different surface density profiles. *Celestial Mechanics and Dynamical Astronomy*, 124(3): 235–268, March 2016. doi: 10.1007/s10569-015-9663-y.

Matthias Y. He, Eric B. Ford, and Darin Ragozzine. Architectures of exoplanetary systems - I. A clustered forward model for exoplanetary systems around Kepler's FGK stars. *MNRAS*, 490(4):4575–4605, December 2019. doi: 10.1093/mnras/stz2869.

Matthias Y. He, Eric B. Ford, Darin Ragozzine, and Daniel Carrera. Architectures of Exoplanetary Systems. III. Eccentricity and Mutual Inclination Distributions of AMD-stable Planetary Systems. *AJ*, 160(6):276, December 2020. doi: 10.3847/1538-3881/abba18.

David M. Hernandez, Sam Hadden, and Junichiro Makino. Are long-term N-body simulations reliable? *MNRAS*, 493(2):1913–1925, April 2020. doi: 10.1093/mnras/staa388.

J. S. Heyl and B. J. Gladman. Using long-term transit timing to detect terrestrial planets. *MNRAS*, 377:1511–1519, June 2007. doi: 10.1111/j.1365-2966.2007.11697.x.

Tomer Holczer, Tsevi Mazeh, Gil Nachmani, Daniel Jontof-Hutter, Eric B. Ford, Daniel Fabrycky, Darin Ragozzine, Mackenzie Kane, and Jason H. Steffen. Transit Timing Observations from Kepler. IX. Catalog of the Full Long-cadence Data Set. *ApJS*, 225(1):9, July 2016. doi: 10.3847/0067-0049/225/1/9.

Jonathan Horner, Pam Vervoort, Stephen R. Kane, Alma Y. Ceja, David Waltham, James Gilmore, and Sandra Kirtland Turner. Quantifying the Influence of Jupiter on the Earth's Orbital Cycles. *AJ*, 159(1):10, January 2020. doi: 10.3847/1538-3881/ab5365.

Chelsea X. Huang, Cristobal Petrovich, and Emily Deibert. Dynamically Hot Super-Earths from Outer Giant Planet Scattering. *AJ*, 153(5):210, May 2017. doi: 10.3847/1538-3881/aa67fb.

Naireen Hussain and Daniel Tamayo. Fundamental limits from chaos on instability time predictions in compact planetary systems. *MNRAS*, 491(4):5258–5267, February 2020. doi: 10.1093/mnras/stz3402.

Kimmo Innanen, Seppo Mikkola, and Paul Wiegert. The Earth-Moon System and the Dynamical Stability of the Inner Solar System. *AJ*, 116(4):2055–2057, October 1998. doi: 10.1086/300552.

Chao-Feng Jiang, Ji-Wei Xie, and Ji-Lin Zhou. On the Orbital Spacing Pattern of Kepler Multiple-planet Systems. *AJ*, 160(4):180, October 2020. doi: 10.3847/1538-3881/abb01b.

Hugh R. A. Jones, R. Paul Butler, C. G. Tinney, Geoffrey W. Marcy, Brad D. Carter, Alan J. Penny, Chris McCarthy, and Jeremy Bailey. High-eccentricity planets from the Anglo-Australian Planet Search. *MNRAS*, 369(1):249–256, June 2006. doi: 10.1111/j.1365-2966.2006.10298.x.

Mario Jurić and Scott Tremaine. Dynamical Origin of Extrasolar Planet Eccentricity Distribution. *ApJ*, 686(1):603–620, October 2008. doi: 10.1086/590047.

Stephen R. Kane and Stephanie M. Torres. Obliquity and Eccentricity Constraints for Terrestrial Exoplanets. *AJ*, 154(5):204, November 2017. doi: 10.3847/1538-3881/aa8fce.

Stephen R. Kane, David R. Ciardi, Dawn M. Gelino, and Kaspar von Braun. The exoplanet eccentricity distribution from Kepler planet candidates. *MNRAS*, 425(1):757–762, September 2012. doi: 10.1111/j.1365-2966.2012.21627.x.

Johannes Kepler. *Astronomia nova*. Pragae, London, 1609.

D. M. Kipping. Parametrizing the exoplanet eccentricity distribution with the beta distribution. *MNRAS*, 434:L51–L55, July 2013. doi: 10.1093/mnrasl/slt075.

Giorgi Kokaia, Melvyn B. Davies, and Alexander J. Mustill. Resilient habitability of nearby exoplanet systems. *MNRAS*, 492(1):352–368, February 2020. doi: 10.1093/mnras/stz3408.

R. K. Kopparapu, E. T. Wolf, and V. S. Meadows. Characterizing Exoplanet Habitability. In Victoria S. Meadows, Giada N. Arney, Britney E. Schmidt, and David J. Des Marais, editors, *Planetary Astrobiology*, page 449. The University of Arizona Press, 2020. doi: 10.2458/azu_uapress_9780816540068.

Ravi Kumar Kopparapu, Ramses Ramirez, James F. Kasting, Vincent Eymet, Tyler D. Robinson, Suvrath Mahadevan, Ryan C. Terrien, Shawn Domagal-Goldman, Victoria Meadows, and Rohit Deshpande. Habitable Zones around Main-sequence Stars: New Estimates. *ApJ*, 765(2):131, March 2013. doi: 10.1088/0004-637X/765/2/131.

Yoshihide Kozai. Secular perturbations of asteroids with high inclination and eccentricity. *AJ*, 67:591–598, November 1962. doi: 10.1086/108790.

J. Laskar. The chaotic motion of the solar system - A numerical estimate of the size of the chaotic zones. *Icarus*, 88:266–291, December 1990. doi: 10.1016/0019-1035(90)90084-M.

J. Laskar. Chaotic diffusion in the Solar System. *Icarus*, 196(1):1–15, July 2008. doi: 10.1016/j.icarus.2008.02.017.

J. Laskar and G. Boué. Explicit expansion of the three-body disturbing function for arbitrary eccentricities and inclinations. *A&A*, 522:A60, November 2010. doi: 10.1051/0004-6361/201014496.

Jacques Laskar. Large scale chaos and marginal stability in the solar system. *Celestial Mechanics and Dynamical Astronomy*, 64(1):115–162, Mar 1996. ISSN 1572-9478. doi: 10.1007/BF00051610. URL `https://doi.org/10.1007/BF00051610`.

U. J. Le Verrier. Recherches sur les mouvements d'Uranus par U. J. Le Verrier (Fortsetzung). *Astronomische Nachrichten*, 25:65, October 1846.

Anne-Sophie Libert and Jacques Henrard. Secular apsidal configuration of non-resonant exoplanetary systems. *Icarus*, 183(1):186–192, Jul 2006. doi: 10.1016/j.icarus.2006.02.007.

Anne-Sophie Libert and Jacques Henrard. Secular frequencies of 3-D exoplanetary systems. *Celestial Mechanics and Dynamical Astronomy*, 100(3):209–229, March 2008. doi: 10.1007/s10569-007-9113-6.

M. L. Lidov. The evolution of orbits of artificial satellites of planets under the action of gravitational perturbations of external bodies. *Planet. Space Sci.*, 9(10):719–759, October 1962. doi: 10.1016/0032-0633(62)90129-0.

D. N. C. Lin, P. Bodenheimer, and D. C. Richardson. Orbital migration of the planetary companion of 51 Pegasi to its present location. *Nature*, 380(6575):606–607, April 1996. doi: 10.1038/380606a0.

Manuel Linsenmeier, Salvatore Pascale, and Valerio Lucarini. Habitability of Earth-like planets with high obliquity and eccentric orbits: results from a general circulation model. In *EGU General Assembly Conference Abstracts*, EGU General Assembly Conference Abstracts, page 15068, May 2014.

Manuel Linsenmeier, Salvatore Pascale, and Valerio Lucarini. Climate of Earth-like planets with high obliquity and eccentric orbits: Implications for habitability conditions. *Planet. Space Sci.*, 105:43–59, January 2015. doi: 10.1016/j.pss.2014.11.003.

J. J. Lissauer, D. Jontof-Hutter, D. Fabrycky, D. Ragozzine, and J. Rowe. Perturbations, TTVs and the (Un)reliability of Ephemerides of Kepler Planets. In *AAS/Division for Planetary Sciences Meeting Abstracts*, volume 52 of *AAS/Division for Planetary Sciences Meeting Abstracts*, page 306.02, October 2020.

Jack J. Lissauer and Sacha Gavino. Orbital stability of compact three-planet systems, I: Dependence of system lifetimes on initial orbital separations and longitudes. *Icarus*, 364: 114470, August 2021. doi: 10.1016/j.icarus.2021.114470.

Jack J. Lissauer, Darin Ragozzine, Daniel C. Fabrycky, Jason H. Steffen, Eric B. Ford, Jon M. Jenkins, Avi Shporer, Matthew J. Holman, Jason F. Rowe, Elisa V. Quintana, Natalie M. Batalha, William J. Borucki, Stephen T. Bryson, Douglas A. Caldwell, Joshua A. Carter,

David Ciardi, Edward W. Dunham, Jonathan J. Fortney, III Gautier, Thomas N., Steve B. Howell, David G. Koch, David W. Latham, Geoffrey W. Marcy, Robert C. Morehead, and Dimitar Sasselov. Architecture and Dynamics of Kepler's Candidate Multiple Transiting Planet Systems. *ApJS*, 197(1):8, November 2011. doi: 10.1088/0067-0049/197/1/8.

Y. Lithwick and Y. Wu. Theory of Secular Chaos and Mercury's Orbit. *ApJ*, 739:31, September 2011. doi: 10.1088/0004-637X/739/1/31.

Yoram Lithwick and Smadar Naoz. The Eccentric Kozai Mechanism for a Test Particle. *ApJ*, 742(2):94, December 2011. doi: 10.1088/0004-637X/742/2/94.

Yoram Lithwick and Yanqin Wu. Secular chaos and its application to mercury, hot jupiters, and the organization of planetary systems. *Proceedings of the National Academy of Sciences*, 111(35):12610–12615, 2014. ISSN 0027-8424. doi: 10.1073/pnas.1308261110. URL `https://www.pnas.org/content/111/35/12610`.

Yoram Lithwick, Jiwei Xie, and Yanqin Wu. Extracting Planet Mass and Eccentricity from TTV Data. *ApJ*, 761(2):122, December 2012. doi: 10.1088/0004-637X/761/2/122.

R. A. Mardling. Resonance, Chaos and Stability in the General Three-Body Problem. In Enrico Vesperini, Mirek Giersz, and Alison Sills, editors, *Dynamical Evolution of Dense Stellar Systems*, volume 246, pages 199–208, May 2008. doi: 10.1017/S1743921308015615.

Michel Mayor and Didier Queloz. A Jupiter-mass companion to a solar-type star. *Nature*, 378(6555):355–359, November 1995. doi: 10.1038/378355a0.

Victoria S. Meadows and Rory K. Barnes. Factors Affecting Exoplanet Habitability. In *Handbook of Exoplanets*, page 57. Springer International Publishing, 2018. doi: 10.1007/978-3-319-55333-7_57.

Abel Méndez and Edgard G. Rivera-Valentín. The Equilibrium Temperature of Planets in Elliptical Orbits. *ApJL*, 837(1):L1, March 2017. doi: 10.3847/2041-8213/aa5f13.

Abel Méndez, Edgard G. Rivera-Valentín, Dirk Schulze-Makuch, Justin Filiberto, Ramses M. Ramírez, Tana E. Wood, Alfonso Dávila, Chris McKay, Kevin N. Ortiz Ceballos, Marcos Jusino-Maldonado, Nicole J. Torres-Santiago, Guillermo Nery, René Heller, Paul K. Byrne, Michael J. Malaska, Erica Nathan, Marta Filipa Simões, André Antunes, Jesús Martínez-Frías, Ludmila Carone, Noam R. Izenberg, Dimitra Atri, Humberto Itic Carvajal Chitty, Priscilla Nowajewski-Barra, Frances Rivera-Hernández, Corine Y. Brown, Kennda L. Lynch, David Catling, Jorge I. Zuluaga, Juan F. Salazar, Howard Chen, Grizelle González, Madhu Kashyap Jagadeesh, and Jacob Haqq-Misra. Habitability Models for Astrobiology. *Astrobiology*, 21(8):1017–1027, August 2021. doi: 10.1089/ast.2020.2342.

Cezary Migaszewski. On the migration of two planets in a disc and the formation of mean motion resonances. *MNRAS*, 453(2):1632–1643, October 2015. doi: 10.1093/mnras/stv1739.

Cezary Migaszewski and Krzysztof Goździewski. A secular theory of coplanar, non-resonant planetary system. *MNRAS*, 388(2):789–802, August 2008. doi: 10.1111/j.1365-2966.2008.13443.x.

S. Millholland and G. Laughlin. Obliquity-driven sculpting of exoplanetary systems. *Nature Astronomy*, March 2019. doi: 10.1038/s41550-019-0701-7.

Sean M. Mills and Daniel C. Fabrycky. Kepler-108: A Mutually Inclined Giant Planet System. *AJ*, 153(1):45, Jan 2017. doi: 10.3847/1538-3881/153/1/45.

Sean M. Mills, Andrew W. Howard, Erik A. Petigura, Benjamin J. Fulton, Howard Isaacson, and Lauren M. Weiss. The California-Kepler Survey. VIII. Eccentricities of Kepler Planets and Tentative Evidence of a High-metallicity Preference for Small Eccentric Planets. *AJ*, 157(5):198, May 2019. doi: 10.3847/1538-3881/ab1009.

Jordi Miralda-Escudé. Orbital Perturbations of Transiting Planets: A Possible Method to Measure Stellar Quadrupoles and to Detect Earth-Mass Planets. *ApJ*, 564(2):1019–1023, Jan 2002. doi: 10.1086/324279.

Althea V. Moorhead, Eric B. Ford, Robert C. Morehead, Jason Rowe, William J. Borucki, Natalie M. Batalha, Stephen T. Bryson, Douglas A. Caldwell, Daniel C. Fabrycky, III Gautier, Thomas N., David G. Koch, Matthew J. Holman, Jon M. Jenkins, Jie Li, Jack J. Lissauer, Philip Lucas, Geoffrey W. Marcy, Samuel N. Quinn, Elisa Quintana, Darin Ragozzine, Avi Shporer, Martin Still, and Guillermo Torres. The Distribution of Transit Durations for Kepler Planet Candidates and Implications for Their Orbital Eccentricities. *ApJS*, 197(1):1, November 2011. doi: 10.1088/0067-0049/197/1/1.

A. Morbidelli, J. I. Lunine, D. P. O'Brien, S. N. Raymond, and K. J. Walsh. Building Terrestrial Planets. *Annual Review of Earth and Planetary Sciences*, 40(1):251–275, May 2012. doi: 10.1146/annurev-earth-042711-105319.

John Moriarty and Sarah Ballard. The Kepler Dichotomy in Planetary Disks: Linking Kepler Observables to Simulations of Late-stage Planet Formation. *ApJ*, 832(1):34, November 2016. doi: 10.3847/0004-637X/832/1/34.

Sarah J. Morrison and Kaitlin M. Kratter. Orbital Stability of Multi-planet Systems: Behavior at High Masses. *ApJ*, 823(2):118, June 2016. doi: 10.3847/0004-637X/823/2/118.

Timothy D. Morton and John Asher Johnson. On the Low False Positive Probabilities of Kepler Planet Candidates. *ApJ*, 738(2):170, September 2011. doi: 10.1088/0004-637X/738/2/170.

Timothy D. Morton, Stephen T. Bryson, Jeffrey L. Coughlin, Jason F. Rowe, Ganesh Ravichandran, Erik A. Petigura, Michael R. Haas, and Natalie M. Batalha. False Positive Probabilities for all Kepler Objects of Interest: 1284 Newly Validated Planets and 428 Likely False Positives. *ApJ*, 822(2):86, May 2016. doi: 10.3847/0004-637X/822/2/86.

Gijs D. Mulders, Christoph Mordasini, Ilaria Pascucci, Fred J. Ciesla, Alexandre Emsenhuber, and Dániel Apai. The Exoplanet Population Observation Simulator. II. Population Synthesis in the Era of Kepler. *ApJ*, 887(2):157, December 2019. doi: 10.3847/1538-4357/ab5187.

C. D. Murray and S. F. Dermott. *Solar system dynamics*. Cambridge University Press, 1999.

Smadar Naoz, Gongjie Li, Macarena Zanardi, Gonzalo Carlos de Elía, and Romina P. Di Sisto. The Eccentric Kozai-Lidov Mechanism for Outer Test Particle. *AJ*, 154(1):18, July 2017. doi: 10.3847/1538-3881/aa6fb0.

Andrew R. Neil and Leslie A. Rogers. A Joint Mass-Radius-Period Distribution of Exoplanets. *ApJ*, 891(1):12, March 2020. doi: 10.3847/1538-4357/ab6a92.

David Nesvorný and David Vokrouhlický. Dynamics and Transit Variations of Resonant Exoplanets. *ApJ*, 823(2):72, June 2016. doi: 10.3847/0004-637X/823/2/72.

G. S. Novak, D. Lai, and D. N. C. Lin. The Interesting Dynamics of the 55 Cancri System. In Drake Deming and Sara Seager, editors, *Scientific Frontiers in Research on Extrasolar Planets*, volume 294 of *Astronomical Society of the Pacific Conference Series*, pages 177–180, January 2003.

Alysa Obertas, Christa Van Laerhoven, and Daniel Tamayo. The stability of tightly-packed, evenly-spaced systems of Earth-mass planets orbiting a Sun-like star. *Icarus*, 293:52–58, September 2017. doi: 10.1016/j.icarus.2017.04.010.

Aviv Ofir, Stefan Dreizler, Mathias Zechmeister, and Tim-Oliver Husser. An independent planet search in the Kepler dataset. II. An extremely low-density super-Earth mass planet around Kepler-87. *A&A*, 561:A103, January 2014. doi: 10.1051/0004-6361/201220935.

Igor Z. Palubski, Aomawa L. Shields, and Russell Deitrick. Habitability and Water Loss Limits on Eccentric Planets Orbiting Main-sequence Stars. *ApJ*, 890(1):30, February 2020. doi: 10.3847/1538-4357/ab66b2.

S. J. Peale. Orbital resonance in the solar system. *ARA&A*, 14:215–246, January 1976. doi: 10.1146/annurev.aa.14.090176.001243.

Cristobal Petrovich, Renu Malhotra, and Scott Tremaine. Planets near Mean-motion Resonances. *ApJ*, 770(1):24, June 2013. doi: 10.1088/0004-637X/770/1/24.

Elke Pilat-Lohinger. The role of dynamics on the habitability of an Earth-like planet. *International Journal of Astrobiology*, 14(2):145–152, April 2015. doi: 10.1017/S1473550414000469.

Henri Poincare. *Les methodes nouvelles de la mecanique celeste*. Gauthier-Villars et fils, 1892.

Sanson T. S. Poon and Richard P. Nelson. On the origin of the eccentricity dichotomy displayed by compact super-Earths: dynamical heating by cold giants. *MNRAS*, 498(4): 5166–5182, November 2020. doi: 10.1093/mnras/staa2755.

Andreas Quirrenbach. The Equilibrium Temperature of Planets on Eccentric Orbits: Time Scales and Averages. *arXiv e-prints*, art. arXiv:2203.11723, March 2022.

F. A. Rasio, C. A. Tout, S. H. Lubow, and M. Livio. Tidal Decay of Close Planetary Orbits. *ApJ*, 470:1187, October 1996. doi: 10.1086/177941.

Sean N. Raymond, Avi M. Mandell, and Steinn Sigurdsson. Exotic Earths: Forming Habitable Worlds with Giant Planet Migration. *Science*, 313(5792):1413–1416, September 2006. doi: 10.1126/science.1130461.

H. Rein and S.-F. Liu. REBOUND: an open-source multi-purpose N-body code for collisional dynamics. *A&A*, 537:A128, January 2012. doi: 10.1051/0004-6361/201118085.

H. Rein and D. S. Spiegel. IAS15: a fast, adaptive, high-order integrator for gravitational dynamics, accurate to machine precision over a billion orbits. *MNRAS*, 446:1424–1437, January 2015. doi: 10.1093/mnras/stu2164.

H. Rein and D. Tamayo. WHFAST: a fast and unbiased implementation of a symplectic Wisdom-Holman integrator for long-term gravitational simulations. *MNRAS*, 452:376–388, September 2015. doi: 10.1093/mnras/stv1257.

Hanno Rein, Garett Brown, and Daniel Tamayo. On the accuracy of symplectic integrators for secularly evolving planetary systems. *MNRAS*, 490(4):5122–5133, December 2019. doi: 10.1093/mnras/stz2942.

Jason F. Rowe, Jeffrey L. Coughlin, Victoria Antoci, Thomas Barclay, Natalie M. Batalha, William J. Borucki, Christopher J. Burke, Steven T. Bryson, Douglas A. Caldwell, Jennifer R. Campbell, Joseph H. Catanzarite, Jessie L. Christiansen, William Cochran, Ronald L. Gilliland, Forrest R. Girouard, Michael R. Haas, Krzysztof G. Hełminiak, Christopher E. Henze, Kelsey L. Hoffman, Steve B. Howell, Daniel Huber, Roger C. Hunter, Hannah Jang-Condell, Jon M. Jenkins, Todd C. Klaus, David W. Latham, Jie Li, Jack J. Lissauer, Sean D. McCauliff, Robert L. Morris, F. Mullally, Aviv Ofir, Billy Quarles, Elisa Quintana, Anima Sabale, Shawn Seader, Avi Shporer, Jeffrey C. Smith, Jason H. Steffen, Martin Still, Peter Tenenbaum, Susan E. Thompson, Joseph D. Twicken, Christa Van Laerhoven, Angie Wolfgang, and Khadeejah A. Zamudio. Planetary Candidates Observed by Kepler. V. Planet Sample from Q1-Q12 (36 Months). *ApJS*, 217(1):16, March 2015. doi: 10.1088/0067-0049/217/1/16.

Megan Shabram, Brice-Olivier Demory, Jessi Cisewski, Eric B. Ford, and Leslie Rogers. The Eccentricity Distribution of Short-period Planet Candidates Detected by Kepler in Occultation. *ApJ*, 820(2):93, April 2016. doi: 10.3847/0004-637X/820/2/93.

Andrew W. Smith and Jack J. Lissauer. Orbital stability of systems of closely-spaced planets. *Icarus*, 201(1):381–394, May 2009. doi: 10.1016/j.icarus.2008.12.027.

Jason H. Steffen and Jason A. Hwang. The period ratio distribution of Kepler's candidate multiplanet systems. *MNRAS*, 448(2):1956–1972, April 2015. doi: 10.1093/mnras/stv104.

Gerald J. Sussman and Jack Wisdom. Chaotic Evolution of the Solar System. *Science*, 257 (5066):56–62, July 1992. doi: 10.1126/science.257.5066.56.

Daniel Tamayo, Miles Cranmer, Samuel Hadden, Hanno Rein, Peter Battaglia, Alysa Obertas, Philip J. Armitage, Shirley Ho, David N. Spergel, Christian Gilbertson, Naireen Hussain, Ari Silburt, Daniel Jontof-Hutter, and Kristen Menou. Predicting the long-term stability of compact multiplanet systems. *Proceedings of the National Academy of Science*, 117(31):18194–18205, August 2020. doi: 10.1073/pnas.2001258117.

Daniel Tamayo, Christian Gilbertson, and Daniel Foreman-Mackey. Stability constrained characterization of multiplanet systems. *MNRAS*, 501(4):4798–4811, March 2021. doi: 10.1093/mnras/staa3887.

W. A. Traub and B. R. Oppenheimer. Direct Imaging of Exoplanets. In S. Seager, editor, *Exoplanets*, pages 111–156. University of Arizona Press, 2010.

Scott Tremaine. The Statistical Mechanics of Planet Orbits. *ApJ*, 807(2):157, July 2015. doi: 10.1088/0004-637X/807/2/157.

S. Udry, X. Dumusque, C. Lovis, D. Ségransan, R. F. Diaz, W. Benz, F. Bouchy, A. Coffinet, G. Lo Curto, M. Mayor, C. Mordasini, F. Motalebi, F. Pepe, D. Queloz, N. C. Santos, A. Wyttenbach, R. Alonso, A. Collier Cameron, M. Deleuil, P. Figueira, M. Gillon, C. Moutou, D. Pollacco, and E. Pompei. The HARPS search for southern extra-solar planets. XLIV. Eight HARPS multi-planet systems hosting 20 super-Earth and Neptune-mass companions. *A&A*, 622:A37, February 2019. doi: 10.1051/0004-6361/201731173.

Vincent Van Eylen and Simon Albrecht. Eccentricity from Transit Photometry: Small Planets in Kepler Multi-planet Systems Have Low Eccentricities. *ApJ*, 808(2):126, August 2015. doi: 10.1088/0004-637X/808/2/126.

Vincent Van Eylen, Joshua N. Winn, and Simon Albrecht. Orbital Circularization of Hot and Cool Kepler Eclipsing Binaries. *ApJ*, 824(1):15, June 2016. doi: 10.3847/0004-637X/824/1/15.

Vincent Van Eylen, Simon Albrecht, Xu Huang, Mariah G. MacDonald, Rebekah I. Dawson, Maxwell X. Cai, Daniel Foreman-Mackey, Mia S. Lundkvist, Victor Silva Aguirre, Ignas Snellen, and Joshua N. Winn. The Orbital Eccentricity of Small Planet Systems. *AJ*, 157 (2):61, February 2019. doi: 10.3847/1538-3881/aaf22f.

Dimitri Veras. Post-main-sequence planetary system evolution. *Royal Society Open Science*, 3:150571, February 2016. doi: 10.1098/rsos.150571.

Dimitri Veras and Philip J. Armitage. Extrasolar Planetary Dynamics with a Generalized Planar Laplace-Lagrange Secular Theory. *ApJ*, 661(2):1311–1322, Jun 2007. doi: 10.1086/516726.

F. Verbunt and R. H. van Gent. Three editions of the star catalogue of Tycho Brahe. Machine-readable versions and comparison with the modern Hipparcos Catalogue. *A&A*, 516:A28, June 2010. doi: 10.1051/0004-6361/201014002.

Pauli Virtanen, Ralf Gommers, Travis E. Oliphant, Matt Haberland, Tyler Reddy, David Cournapeau, Evgeni Burovski, Pearu Peterson, Warren Weckesser, Jonathan Bright, Stéfan J. van der Walt, Matthew Brett, Joshua Wilson, K. Jarrod Millman, Nikolay Mayorov, Andrew R. J. Nelson, Eric Jones, Robert Kern, Eric Larson, C. J. Carey, İlhan Polat, Yu Feng, Eric W. Moore, Jake VanderPlas, Denis Laxalde, Josef Perktold, Robert Cimrman, Ian Henriksen, E. A. Quintero, Charles R. Harris, Anne M. Archibald, Antônio H. Ribeiro, Fabian Pedregosa, Paul van Mulbregt, and SciPy 1. 0 Contributors. SciPy 1.0: fundamental algorithms for scientific computing in Python. *Nature Methods*, 17:261–272, February 2020. doi: 10.1038/s41592-019-0686-2.

Kathryn Volk and Renu Malhotra. Dynamical Instabilities in Systems of Multiple Short-period Planets Are Likely Driven by Secular Chaos: A Case Study of Kepler-102. *AJ*, 160 (3):98, September 2020. doi: 10.3847/1538-3881/aba0b0.

Mara Volpi, Arnaud Roisin, and Anne-Sophie Libert. The 3D secular dynamics of radial-velocity-detected planetary systems. *A&A*, 626:A74, Jun 2019. doi: 10.1051/0004-6361/201834896.

M. J. Way and Nikolaos Georgakarakos. Effects of Variable Eccentricity on the Climate of an Earth-like World. *ApJL*, 835(1):L1, January 2017. doi: 10.3847/2041-8213/835/1/L1.

Lauren M. Weiss, Geoffrey W. Marcy, Erik A. Petigura, Benjamin J. Fulton, Andrew W. Howard, Joshua N. Winn, Howard T. Isaacson, Timothy D. Morton, Lea A. Hirsch, Evan J. Sinukoff, Andrew Cumming, Leslie Hebb, and Phillip A. Cargile. The California-Kepler Survey. V. Peas in a Pod: Planets in a Kepler Multi-planet System Are Similar in Size and Regularly Spaced. *AJ*, 155(1):48, January 2018. doi: 10.3847/1538-3881/aa9ff6.

Darren M. Williams and David Pollard. Earth-like worlds on eccentric orbits: excursions beyond the habitable zone. *International Journal of Astrobiology*, 1(1):61–69, January 2002. doi: 10.1017/S1473550402001064.

Joshua N. Winn and Daniel C. Fabrycky. The Occurrence and Architecture of Exoplanetary Systems. *ARA&A*, 53:409–447, August 2015. doi: 10.1146/annurev-astro-082214-122246.

J. Wisdom. The resonance overlap criterion and the onset of stochastic behavior in the restricted three-body problem. *AJ*, 85:1122–1133, August 1980. doi: 10.1086/112778.

J. Wisdom. The origin of the Kirkwood gaps - A mapping for asteroidal motion near the 3/1 commensurability. *AJ*, 87:577–593, March 1982. doi: 10.1086/113132.

J. Wisdom, M. Holman, and J. Touma. Symplectic Correctors. *Fields Institute Communications*, 10:217, January 1996.

Jack Wisdom. Resolving the Pericenter. *AJ*, 150(4):127, October 2015. doi: 10.1088/0004-6256/150/4/127.

Jack Wisdom and Matthew Holman. Symplectic maps for the N-body problem. *AJ*, 102: 1528–1538, October 1991. doi: 10.1086/115978.

A. Wolszczan and D. A. Frail. A planetary system around the millisecond pulsar PSR1257 + 12. *Nature*, 355(6356):145–147, January 1992. doi: 10.1038/355145a0.

J. T. Wright, S. Upadhyay, G. W. Marcy, D. A. Fischer, Eric B. Ford, and John Asher Johnson. Ten New and Updated Multiplanet Systems and a Survey of Exoplanetary Systems. *ApJ*, 693(2):1084–1099, March 2009. doi: 10.1088/0004-637X/693/2/1084.

Jason T. Wright and B. Scott Gaudi. *Exoplanet Detection Methods*, pages 489–540. Springer Netherlands, 2013. ISBN 978-94-007-5606-9. doi: 10.1007/978-94-007-5606-9_10.

Ji-Wei Xie, Subo Dong, Zhaohuan Zhu, Daniel Huber, Zheng Zheng, Peter De Cat, Jianning Fu, Hui-Gen Liu, Ali Luo, Yue Wu, Haotong Zhang, Hui Zhang, Ji-Lin Zhou, Zihuang Cao, Yonghui Hou, Yuefei Wang, and Yong Zhang. Exoplanet orbital eccentricities derived from LAMOST-Kepler analysis. *Proceedings of the National Academy of Science*, 113(41): 11431–11435, October 2016. doi: 10.1073/pnas.1604692113.

Wenrui Xu and Dong Lai. Migration of planets into and out of mean motion resonances in protoplanetary discs: analytical theory of second-order resonances. *MNRAS*, 468(3): 3223–3238, July 2017. doi: 10.1093/mnras/stx668.

Jun Yang, Gwenaël Boué, Daniel C. Fabrycky, and Dorian S. Abbot. Strong Dependence of the Inner Edge of the Habitable Zone on Planetary Rotation Rate. *ApJL*, 787(1):L2, May 2014. doi: 10.1088/2041-8205/787/1/L2.

Samuel W. Yee, Daniel Tamayo, Samuel Hadden, and Joshua N. Winn. How Close are Compact Multiplanet Systems to the Stability Limit? *AJ*, 162(2):55, August 2021. doi: 10.3847/1538-3881/ac00a9.

Wei Zhu and Subo Dong. Exoplanet Statistics and Theoretical Implications. *ARA&A*, 59, September 2021. doi: 10.1146/annurev-astro-112420-020055.

Jon K. Zink, Jessie L. Christiansen, and Bradley M. S. Hansen. Accounting for incompleteness due to transit multiplicity in Kepler planet occurrence rates. *MNRAS*, 483(4): 4479–4494, March 2019. doi: 10.1093/mnras/sty3463.

Andras Zsom. A Population-based Habitable Zone Perspective. *ApJ*, 813(1):9, November 2015. doi: 10.1088/0004-637X/813/1/9.